Photocatalytic Hydrogen Production with Iron Oxide under Solar Irradiation

Simin Liu, BSc (JNU, 2003), MIT (QUT, 2006)

A thesis submitted in fulfillment of the requirement for the degree of Master of Applied Science in Chemistry (Research) on the basis of research work carried out at Chemistry Discipline, Faculty of Science and Technology, QUT under the supervision of A/Professor Geoffrey Will and Dr Wayde Martens

Queensland University of Technology, Brisbane, October 2010

Statement of Original Authorship

I hereby declare that this submission is my own work and the work contained in this thesis has not been previously submitted to meet requirements for an award at this or any other higher educational institution. To the best of my knowledge and belief, this thesis does not contain any material previously published or written by another person except where due reference is made.

Signature

Date

Acknowledgements

First and foremost, I would like to thank, A/Professor Geoffrey Will, my principal supervisor, for his guidance and patience throughout this project.

Many thanks also go to Dr Wayde Martens, my associate supervisor, for his training given to me on the instruments as needed (e.g. TGA, UV-Vis) and his advice on the film preparation.

Dr Serge Kokot was thanked for guidance on writing and corrections of the review paper which was published in Journal of Photochemistry and Photobiology C: Photochemistry Review in 2009.

Dr Thor Bostrom, Dr Deborah Stenzel and Dr Loc Duong are also thanked for their help with SEM and EDX as needed.

I also give my appreciation to Tony Raftery for his help and assistance with XRD and taking the time to answer all of my questions about XRD.

The other members of my research group (Stuart Bell, Adrian Fuchs, Dr Sarah Costanzo) are thanked massively for their help and support to get this project completed successfully.

To all the fellow postgraduates who helped, especially Ashley Loke and Henry Spratt who prepared titanium oxychloride solution for me, I give thanks.

I wish to thank CSIRO: National Hydrogen Materials Flagship for financial support through a scholarship.

Finally, I thank my wife, Lucy, my family and friends for their support and understanding during the two and a half years' time.

Abstract

As solar hydrogen is a sustainable and environmental friendly energy carrier, it is considered to take the place of fossil fuels in the near future. Solar hydrogen can be generated by splitting of water under solar light illumination. In this study, the use of nanostructured hematite thin-film electrodes in photocatalytic water splitting was investigated.

Hematite (α-Fe_2O_3) has a narrow band-gap of 2.2 eV, which is able to utilise approximately 40% of solar radiation. However, poor photoelectrochemical performance is observed for hematite due to low electrical conductivity and a high rate of electron-hole recombination. An extensive review of useful measures taken to overcoming the disadvantages of hematite so as to enhance its performance was presented including thin-film structure, nanostructuring, doping, etc.

Since semiconductoring materials which exhibit an inverse opal structure are expected to have a high surface-volume ratio, unique optical characteristics and a shorter distance for photogenerated holes to travel to the electrode/electrolyte interface, inverse opals of hematite thin films deposited on FTO glass substrate were successfully prepared by doctor blading using PMMA as a template. However, due to the poor adhesion of the films, an acidic medium (i.e., 2 M HCl) was employed to significantly enhance the adhesion of the films, which completely destroyed the inverse opal structure. Therefore, undoped, Ti and Zn-doped hematite thin films deposied on FTO glass substrate without an inverse opal structure were prepared by doctor blading and spray pyrolysis and characterised using SEM, EDX, XRD, TGA, UV-Vis spectroscopy and photoelectrochemical measurements.

Regarding the doped hematite thin films prepared by doctor blading, the photoelectrochemical activity of the hematite photoelectrodes was improved by incorporation of Ti, most likely owing to the increased electrical conductivity of the films, the stabilisation of oxygen vacancies by Ti^{4+} ions and the increased electric field of the space charge layer. A highest photoresponse was recorded in case of 2.5 at.% Ti which seemed to be an optimal concentration. The effect of doping content,

thickness, and calcination temperature on the performance of the Ti-doped photoelectrodes was investigated. Also, the photoactivity of the 2.5 at.% Ti-doped samples was examined in two different types of electrochemical cells. Zn doping did not enhance the photoactivity of the hematite thin films though Zn seemed to enhance the hole transport due to the slow hole mobility of hematite which could not be overcome by the enhancement. The poor performance was also obtained for the Ti-doped samples prepared by spray pyrolysis, which appeared to be a result of introduction of impurities from the metallic parts of the spray gun in an acidic medium.

Further characterisation of the thin-film electrodes is required to explain the mechanism by which enhanced performance was obtained for Ti-doped electrodes (doctor blading) and poor photoactivity for Zn and Ti-doped samples which were synthesised by doctor blading and spray pyrolysis, respectively. Ti-doped hematite thin films will be synthesised in another way, such as dip coating so as to maintain an inverse opal structure as well as well adhesion. Also, a comparative study of the films will be carried out.

Papers

Journal publications

1. Liu, S., Kokot, S., Will, G., Photochemistry and chemometrics - An overview, *Journal of Photochemistry and Photobiology C: Photochemistry Reviews*, 2009. 10: p. 159-172.

Conference presentations

1. Liu, S., Martens, W., Bell, S., Will, G., Photocatalytic Hydrogen Production and Water Purification with Iron Oxide under UV/Vis Irradiation, World Hydrogen Energy Conference, Brisbane Australia, June 2008 (Poster presentation and long abstract).

Table of Contents

List of Figures

List of Tables

List of Abbreviations

3DOM	Three-dimensionally ordered macroporous
APCVD	Atmospheric pressure chemical vapour deposition
at.%	Atom %
BET	Brunauer-Emmett Teller
BG	Band gap
CB	Conduction band
DSSC	Dye-sensitised solar cell
DTG	Derivative thermogravimetric analysis
EDX	Energy-dispersive X-ray spectrometry
EISA	Evaporation-induced self-assembly
FCC	Face-centered cubic
FTO	Fluorine doped tin oxide
FWHM	Full-width at half maximum
IPCE	Incident-photon-to-electron conversion efficiency
ITO	Tin doped Indium oxide
MMA	Methyl methacrylate
MPD	Multipurposed X-ray diffractometer
NHE	Normal hydrogen electrode
NIR	Near infrared
NUV	Near ultraviolet
P	Photon
PBG	Photonic band gap
PEC	Photoelectrochemical
PIB-PEO	poly(isobutylene)-block-poly(ethylene oxide)
PMMA	Poly(methyl methacrylate)
RHE	Reversible hydrogen electrode

SCE	Saturated calomel electrode
SE	Substrate-electrode
SEM	Scanning electron microscopy
SHE	Standard hydrogen electrode
TCO	Transparent conducting oxide
TEM	Transmission electron microscopy
TEOS	Tetraethyl orthosilicate
TGA	Thermogravimetric analysis
UPS	Ultrasonic spray pyrolysis
UV	Ultraviolet
VB	Valence band
Vis	Visible
WMO	World Metrological Organization
XRD	X-ray Diffraction

1. Introduction

1.1. Solar hydrogen

1.1.1. Hydrogen energy and production

Fossil fuels (i.e. hydrocarbon fuels), such as oil, coal and natural gas play an important role in the development of global economy, providing all the energy for industry, agriculture, transportation and daily life. About 80 percent of the world total primary energy supply derived from the combustion of fossil fuels in 2006 [17]. However, fossil fuels are non-renewable resources. Excessive exploitation and over-consumption of fossil fuels resulting from the rapid growth of world economy and the on-going increase of world population will cause a shortage of energy resources in near future. The world's energy needs will increase by 50 percent by 2030 [18]. It is believed that world oil reserves will last for only 40 or 50 years [19], and global coal output will peak as soon as 2025 [20].

The use of fossil fuels raises environmental concerns. The exhaust gases produced from the combustion of fossil fuels (e.g. coal power plant, automobile), such as NO_x, SO_2, and CO_2 result in acid rain and lead to global warming. Moreover, the produced waste contains 25 to 30 trace elements, e.g. chromium, arsenic, cadmium, chlorine, fluorine, mercury, which are toxic and hazardous and thus cause air pollution [21].

As a result of a risk of energy shortage, climate change, and air pollution, scientists have been seeking alternative and renewable energy sources to replace fossil fuels for decades. Hydrogen is regarded as one of the ideal fuels because it is the most abundant element in the universe, lightest fuel and richest in energy per unit mass (34.0 Kcal/g, Table 1) [16]. Also, the combustion of hydrogen with oxygen in air

Fuel	Energy (Kcal/g)
Hydrogen	34.0
Petroleum	8.4-10.3
Paraffin	9.8-10.3
Graphite (Coal)	7.8
Caster oil	9.4
Wood	4.2

Table 1. Heat energy of burning of a variety of fuels, reproduced from *Jain* [16].

produces water, which is environmental friendly. However, hydrogen is not a primary fuel as it does not naturally occur in large amounts. In order to produce hydrogen fuel, two key components are necessary: energy and hydrogen atoms. Hydrogen atoms are found most often as part of many larger molecules, such as water and methane. Water contains only hydrogen and oxygen atoms and thus is free of carbon atoms. The energy required for splitting of water can be supplied from a wide range of energy sources. If the energy is supplied by a source of renewable and clean energy, such as sunlight, wind, tidal or hydrothermal, hydrogen fuel can be produced in a sustainable and clean manner. Therefore, solar hydrogen is a clean, green form of energy which is produced with the use of sunlight and water. Replacement of fossil fuels with solar hydrogen will relieve global energy tension, and cause reduction of greenhouse gas emission and improvement of air quality.

1.1.2. Basics of solar radiation

The sun gives off a vast amount of radiant energy in the form of electromagnetic waves, i.e., solar radiation. About half of the radiation at the earth surface lies in visible region of the spectrum. The other half lies mostly in NIR region with small in near-ultraviolet (NUV) region of the spectrum [22]. Light consists of individual particles called photons. The energy of a photon depends only on its frequency (ν) or equivalently, its wavelength (λ) and the formula is given by:

$$E = h\nu = \frac{hc}{\lambda} \tag{1.1a}$$

where h is Planck's constant (6.626 x 10^{-34} J·s) and c the speed of light (3.0 x10^{8}

$$\lambda(nm) = 1241/E(eV) \quad (1.1b)$$

$m.s^{-1}$) and where 1 eV equals to 1.062 x 10^{-19} J [23]. Hence, the wavelength ranges in solar spectrum correspond to collections of photons with different energies [22]. The spectrum of NUV, visible and NIR ranges in wavelength (nm) andb energy (eV) are tabulated (Table 2).

Name	Wavelength range in nm	Energy per photon in eV	% E
NUV	300 - 400 nm	3.10 - 4.13 eV	7 %
visible	400 - 700 nm	1.77 - 3.10 eV	50 %
NIR	780 -3000 nm	0.89 - 1.65 eV	43 %

Table 2. Spectrum ranges of NUV, visible and NIR in nanometers and electronvolts [22].

1.2. Water splitting

Water splitting can be achieved by several different types of approaches. One of the approaches is electrolysis which requires a supply of external electrical power to split water. Here, a solar cell can provide electrical energy to convert water into hydrogen. Another approach is photocatalysis. Photocatalysis is a chemical process which is facilitated by light impinging on a photo-activated substance, i.e. a photocatalyst [24]. Solar light collection and water splitting are combined into a single photoelectrode by this photoelectrochemical process, to produce hydrogen. When a photon, energy of which is above or equal to that of the band gap of a semiconductor, impinges on a photocatalyst as shown in Fig. 1, an electron is excited from the valence band to the conduction band, leaving a positive hole. The electron is able to reduce water to molecular hydrogen, and the photogenerated positive hole can oxidise hydroxide ion to oxygen and water in basic solution. The first step in the process is photon absorption by the semiconductor and photoexcitation of an electron, which is followed by the water electrolysis reaction at the surface of the semiconductor [1]. The chemical equations in basic solution are shown below [25]:

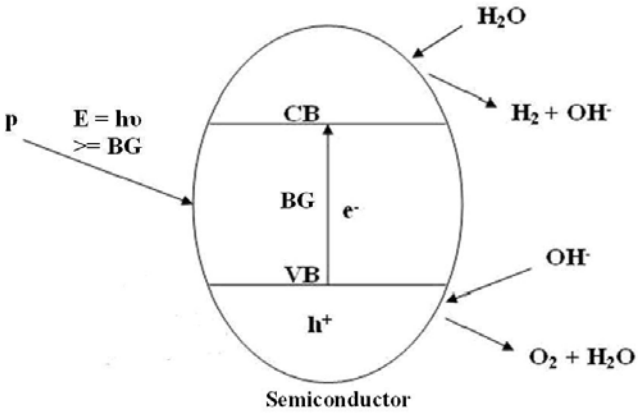

Figure 1. Photocatalysis of water: conduction band (CB), valence band (VB), band gap (BG), photon (p), electron (e^-), positive hole (h^+) [1]

Photon absorption:	$4h\nu \rightarrow 4h^+ + 4e^-$	(1.2a)
Anode (oxidation):	$4h^+ + 4OH^-(aq) \rightarrow O_2(g) + H_2O(aq)$	(1.2b)
Cathode (reduction):	$4e^- + 4H_2O(l) \rightarrow 2H_2(g) + 4OH^-(aq)$	(1.2c)
Overall reaction:	$2H_2O(l) + 4h\nu \rightarrow 2H_2(g) + O_2(g)$	(1.2d)

It is noted that the number of absorbed photons is equal to the number of produced electron-hole pairs, which is twice that of produced H_2 molecules, i.e. two photons or two electrons per hydrogen molecule.

The thermodynamic potential (E^o_{cell}) for the water-splitting reaction is 1.23 eV and thus an electrical energy corresponding to the change in the Gibb's free energy ΔG^o_{cell} of the reaction must be supplied (237.178 kJ·mol^{-1} at 298 K and 1 bar) according to the equation below:

$$\Delta G^\circ_{cell} = -nFE^\circ_{cell} \quad (1.3)$$

where n is the number of moles of electrons transferred in the reaction and F is the Faraday constant (96485 C/mol) [26]. However, in practice about 2.0 eV is required to overcome the energy losses relating to reaction kinetics and charge transfer through electrical leads and electrolyte, i.e. the electrode overpotentials and the Ohmic overpotentials [25, 27]. The electrode overpotentials result from the low activity of the electrodes in electrolyte, which is also known as activation

overpotential. The Ohmic overpotential is due to the resistive losses in the cell. In order to obtain high efficiency of water splitting, overpotential must be minimised. Reduction of both electrode and Ohmic overpotentials is assisted by a rise in operating temperature which causes a decrease of the electrolyte resistance and an increase of the reaction rate [27].

1.3. Semiconductoring photocatalysts

1.3.1. Energy levels in semiconductors and electrolytes

In electronic band structure of a semiconductor which is represented in Fig. 1, the highest energy band is called the valence band, which is almost fully occupied by electrons, while the lowest energy band is called the conduction band, which is almost unoccupied. A band gap (E_g) is the energy difference between the lower energy level of conduction band (E_c) and the upper energy level of valence band (E_v), where no electron states exist. The band gap is larger in an insulator (> 4 eV) and the two bands overlap in a metal. Bandgap energies (E_g) of semiconductors commonly range from 1 to 3 eV, and this range overlaps well with the solar spectrum at the surface of the Earth [28].

A spontaneous water splitting process under irradiation requires that the conduction band edge of a semiconductor photoelectrode should be located above (i.e., more negative than, NHE as reference) the reduction potential of water, which is favourable for electron transfer to reduce water to hydrogen whereas the valence band should be located below (i.e. more positive than) the oxidation potential, which is favourable for hole transfer to oxidise water to oxygen, presented in Fig. 2 [3].

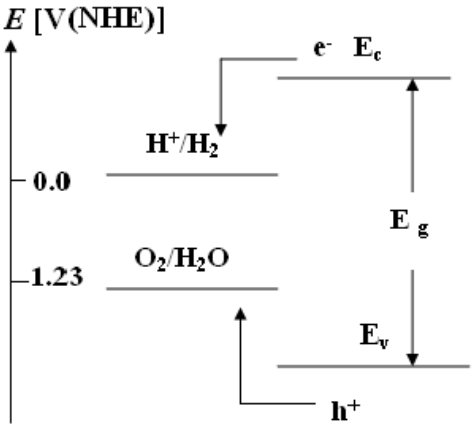

Figure 2. Band position of a semiconductor under the condition of spontaneous water splitting. The water reduction and oxidation potentials are given in volts relative to normal hydrogen electrode (NHE).

However, in many semiconductor-electrolyte systems, the conduction band edge of the semiconductor is below the reduction potential of water. Thus, an electron transfer barrier is created and spontaneous water splitting becomes impossible. An external electrical bias or internal chemical bias (by generating a pH gradient between anode and cathode with two electrolytes of different pH) [29] is required to assist the water splitting.

The band gap determines what portion of the solar spectrum a semiconductor photoelectrode absorbs. For example, TiO_2 has a band gap of about 3.2 eV and thus the cut-off wavelength is about 388 nm derived from Eq.1.1b which is in the UV region. Therefore, any photons with wavelength below or equal to 388 nm are able to excite and generate electron-hole pairs in TiO_2. The Fermi energy level (E_F) of a semiconductor is referred to as the energy level at which the probability of occupation by an electron is one-half, which is equivalent to the electrochemical potential of electrons in the semiconductor [28].

Another feature of band theory is the way an electron is transferred to the conduction band. A direct bandgap indicates that the two band edges occur at the same value of k -vector, e.g. gallium arsenide, gallium nitride. An indirect bandgap refers to that the conduction band edge (E_c) and the valence band edge (E_v)

occurring at a different value of k-vector. Examples of indirect bandgap semiconductors include silicon, germanium, and silicon carbide. The best values of the band gap are obtained by optical absorption. For a direct bandgap semiconductor in Fig. 3a, E_c and E_v occur at the same wavevector $k \approx 0$. In the direct absorption process, a photon of wavevector $k \approx 0$ and frequency υ is absorbed by the semiconductor with the generation of an electron and a hole in the conduction and valence bands, respectively. Hence $h\nu = E_g$. For an indirect bandgap semiconductor in Fig. 3b, E_c and E_v are separated by a substantial wavevector k_c. In the indirect absorption process, absorption of a photon of wavevector $k \approx 0$ and frequency ν results in the creation of a phonon of wavevector $K \approx -k_c$ and frequency Ω, which will move the electron across *k* space by an amount of $-k_c$. Hence $k(photon) = k_c + K \approx 0$ and $h\nu = E_g + h\Omega$, which satisfy conservation of wavevector as well as energy [2].

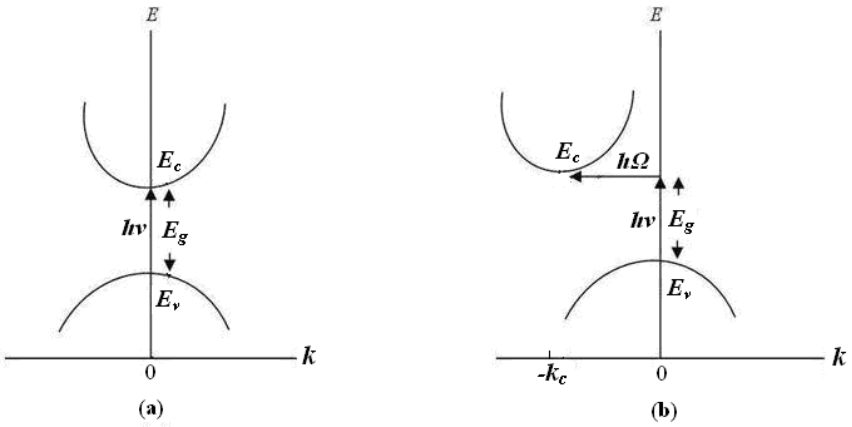

Figure 3. A schematic representation of a) a direct band gap with a direct photon transition, and b) an indirect bandgap with an indirect photon transition, reproduced from *Kittel* [2].

The density of energy states within the energy bands, which increases with the increase of the energy above the conduction band or below the valence band edge, are shown below:

$$N_c = \frac{8\sqrt{2\pi}}{h^3}\left(m_e^*\right)^{3/2}\left(E - E_c\right)^{1/2} \tag{1.4a}$$

and

$$N_v = \frac{8\sqrt{2\pi}}{h^3}\left(m_h^*\right)^{3/2}\left(E - E_v\right)^{1/2} \tag{1.4b}$$

for the conduction band and valence band, respectively, where h is Planck's constant and m_e^* and m_h^* the effective masses of electrons and holes, respectively. The equilibrium electron (n_o) and hole (p_o) concentrations in the conduction band and valence band, respectively, are given by:

$$n_o = N_c \, exp\left(-\frac{E_c - E_F}{kT}\right) \tag{1.4c}$$

$$p_o = N_v \, exp\left(-\frac{E_v - E_F}{kT}\right) \tag{1.4d}$$

where k is the Boltzmann constant (1.38 x 10^{-23} J/K), and T the temperature (Kelvin scale, K). Multiplying eq.1.4c and eq.1.4d, an equilibrium concentration can be expressed as:

$$n_o p_o = N_c N_v \, exp\left(\frac{E_c - E_v}{kT}\right) = n_i^2 \tag{1.4e}$$

where n_i^2 is the intrinsic carrier concentration which exponentially decreases with the increase of band gap [4].

An intrinsic semiconductor is a pure semiconductor without any impurity present. In an intrinsic semiconductor, the electron and hole concentrations in the conduction (n_o) and valence bands (p_o), respectively at equilibrium are equal. The Fermi energy level stays in the middle of the band gap as illustrated in Fig. 4a.

An extrinsic semiconductor is a semiconductor in which a dopant has been introduced. Impurity elements introduced into an intrinsic semiconductor are classified as either donors or acceptors, changing the charge carrier concentrations in the semiconductor. Since donor atoms have more valence electrons than the atoms

they replace in an intrinsic semiconductor, they donate their extra valence electrons into the conduction band of the semiconductor and thus the semiconductor possesses excess electrons, which enhance the equilibrium electron concentration in the conduction band (n_o), producing an *n*-type semiconductor. In *n*-type semiconductors, electrons and holes are the majority and minority carriers, respectively. Moreover, the Fermi level (E_F) lies just below the conduction band edge (E_c) of an *n*-type semiconductor as illustrated in Fig. 4b. Acceptor atoms have fewer valence electrons than the intrinsic atoms they replace so they accept electrons from the valence band and the semiconductor have excess holes, which increase the equilibrium hole concentration in the valence band (p_o), generating a *p*-type semiconductor. In *p*-type semiconductors, holes and electrons are the majority and minority carriers, respectively. Also, the Fermi level (E_F) lies just above the valence band edge (E_v) of a *p*-type semiconductor as illustrated in Fig. 4c. For example, atoms of Group IV and II are employed by semiconductors of Group III as donors and acceptors, respectively.

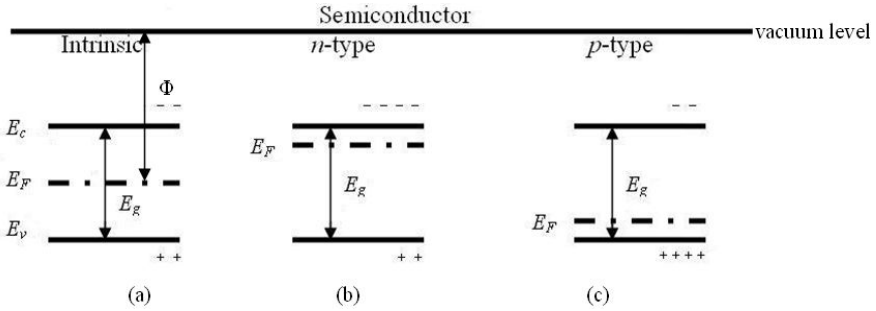

Figure 4. A schematic representation of energy band levels of an a) intrinsic, b) *n*-type, and c) *p*-type semiconductor. A work function (Φ) in (a) indicates the work required to remove an electron from the Fermi level of the intrinsic semiconductor to the vacuum level, reproduced from *Grimes [3]*.

In a redox system (i.e., electrolyte redox system), the electrochemical potential of electrons ($\overline{\mu}_{e,redox}$) is usually given relative to a reference electrode, which is conventionally the normal hydrogen electrode (NHE) or Saturated calomel electrode

(SCE). The corresponding electrochemical potential is equal to the Fermi level of the redox system $E_{F,redox}$ on the absolute scale [30], i.e.

$$E_{E,redox} = \bar{\mu}_{e,redox} \tag{1.5}$$

Moreover, there exist occupied and unoccupied energy states relating to the reduced and the oxidised species of the redox system, respectively. A Gaussian distribution of the redox energy states against electron energy is shown in Fig. 5.

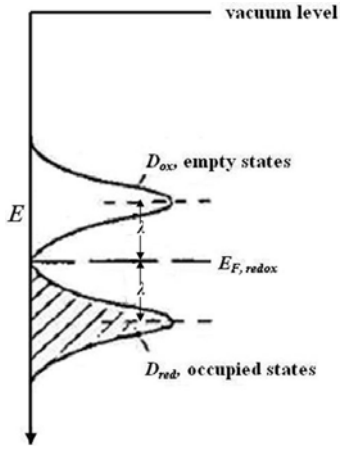

Figure 5. A schematic representation of energy distribution of a redox system. In the electrolyte solution, the occupied energy states (shaded) and empty energy states (unshaded) are broadened by the fluctuating solvent environment to Gaussian distributions, corresponding to D_{red} and D_{ox}, respectively, where λ is the Marcus reorganisation energy, reproduced from *Nozik* [4].

1.3.2. The semiconductor and electrolyte interface

An interface between a semiconductor photoelectrode and an aqueous electrolyte solution is similar to a Schottky junction in many respects. The interfacial behavior between these two phases is described by a diffuse ionic double layer model [4, 5, 31-35]. An equilibrium at the interface is achieved when the electrochemical potential of these two phases is equal, i.e.:

$$E_F = E_{F,redox} \tag{1.6}$$

In a photoelectrolysis cell, a semiconductor as a working electrode and a metal as a counter electrode (e.g., Pt) are connected and immersed in an electrolytic solution. Fig. 6 shows the energy band diagrams of an *n-type* semiconductor

photoanode and a metal cathode with a redox system. When the two electrodes and the electrolyte are under initial condition, there is no contact between the semiconductor and the metal and no equilibrium through the solution (Fig. 6a). The conduction and valence bands are flat due to no net excess charge at the interface and the electrode potential of the semiconductor is called the flat band potential (V_{FB}). Fig. 6b describes that in the dark, electrons leave the semiconductor via an ohmic contact, traverse an external circuit to the metal cathode as the Fermi level of the semiconductor is above that of the metal until the two Fermi levels lie at the same energy (i.e., at equilibrium), leaving holes behind in the space charge region (i.e., the depletion layer). Two band edges bend upward by energy of E_B so that a potential barrier (i.e., a Schottky barrier) is established against further electron transfer. Since the Fermi level of the metal cathode is lower than the water reduction potential, an electron transfer barrier is formed between the two energy levels and thus water splitting is unfavorable. In Fig. 6c, under illumination, the photo-generation of

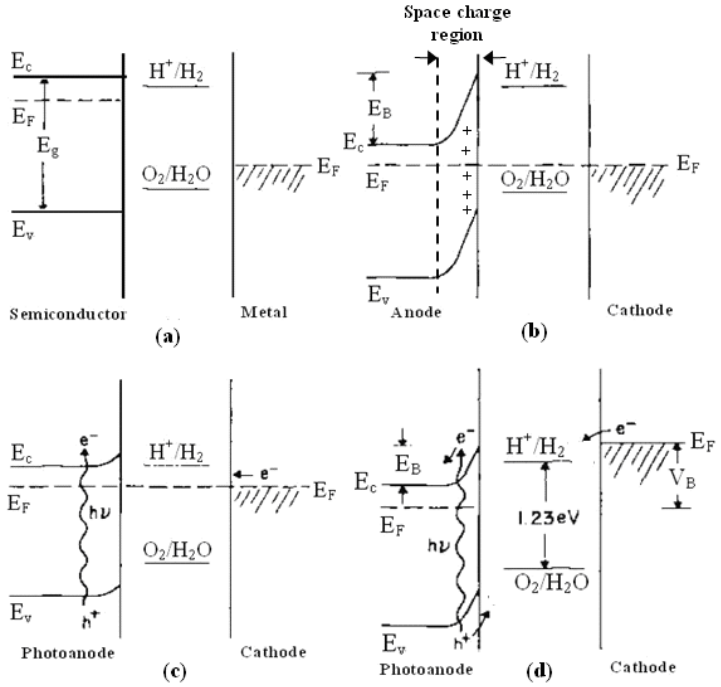

Figure 6. Energy level diagrams of a photoelectrolysis cell consisting of *n-type* semiconductor-metal, a) no semiconductor junction and no chemical potential equilibrium, b) under equilibrium condition in the dark, c) under illumination without bias (V_B), and d) under illumination with bias, reproduced from *Nozik* [5].

electron-hole pairs results in a decrease of band bending before a new equilibrium is established. At the new equilibrium, the water reduction potential is still above the Fermi level of the metal. Fig. 6d shows that an anodic bias is applied to raise the Fermi level of the metal cathode above the water reduction potential so that electrons are injected from the cathode to the electrolyte to reduce water to hydrogen and holes are injected from the photoanode to the electrolyte to oxidise water to oxygen. For a *p-type* semiconductor in a photoelectrolysis cell under illumination, the two bands bend downward. Photogenerated minority electrons in the semiconductor are swept to the surface and then injected to the electrolyte to reduce water. The photogenerated majority holes are swept toward the semiconductor bulk where they transfer to the metal anode and then are injected to the electrolyte to oxidise water. In the above case where the metal Fermi level is below the water reduction potential, an external bias is applied to sustain the current flow and increase the band bending to maintain the separation of photogenerated electron-hole pairs which is driven by the electric field in the semiconductor. Semiconductors such as ZnO, SiC, CdS, of which the flat band potential is above the water reduction potential, that is, the two band edges straddle the redox potential for water splitting [4]. Hence, no applied voltage is required for water photoelectrolysis. However, the bandgap of these semiconductors is relatively large so that the sunlight absorption is low, especially, absorption in the visible region. External bias is not required if both an *n*-type semiconductor and a *p-type* semiconductor are used as the two electrodes in a photoelectrolysis cell and the electron affinities of the two semiconductors are different. More details of a *p-n* photoelectrolysis cell are available in the reference [36].

1.3.3. Semiconductor Electrode Stability

In a water splitting cell, the photo-produced electrons and holes in the semiconductor photoelectrodes exhibit highly reducing and oxidising abilities, respectively. These holes and electrons may oxidise and reduce the semiconductor, respectively, leading to dissolution, of which the processes are called anodic and

cathodic photocorrosion, respectively. Photocorrosion of semiconductors represents a severe problem since it decreases energy conversion efficiencies and shortens the lifetime of electrodes.

Gerischer [37, 38] and Bard [39] developed a simple model of electrode stability where the redox potential of the anodic and cathodic photocorrosion are present in an energy diagram. The stability of an electrode is determined by comparison of the locations of the two photocorrosion reactions with those of the water splitting reaction, and with the two band edges of the electrode as shown in Fig. 7. When the redox potential of the cathodic decomposition reaction is above the conduction band edge and the redox potential of the anodic decomposition reaction is below the valence band edge on the SCE scale, the electrode is thermodynamically stable as illustrated in Fig. 7a. Unfortunately, there are no semiconductors known so far which match this situation. If one or both of the redox potential of the two decomposition reactions lie within the band gap, the electrode becomes unstable (see Fig. 7b, c and d). Therefore, electrode stability is dependent on the competition between charge carriers capture by water and charge carriers capture by the surface atoms of the

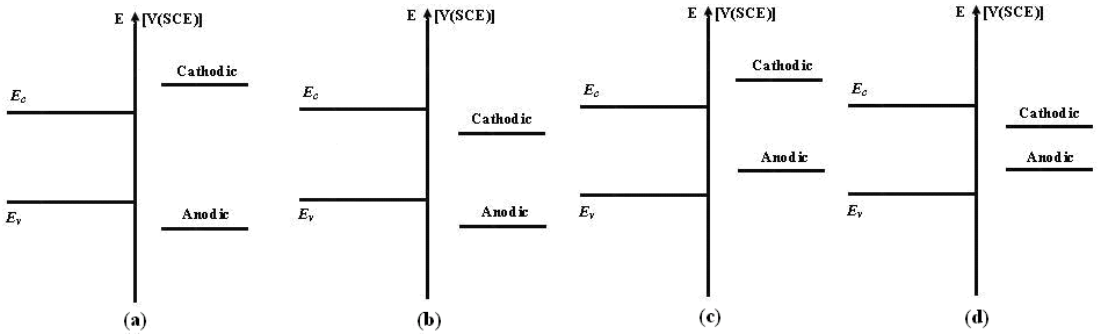

Figure 7. Energy level diagrams of a semiconductor in an electrolyte under the conditions of a) electrode stability, b) cathodic decomposition, c) anodic decomposition, and d) anodic and cathodic decomposition.

electrode, which are controlled by the relative kinetics of those corresponding reactions [5].

Some metal oxide semiconductors such as TiO_2, SnO_2, WO_3, $SrTiO_3$ are resistant to photocorrosion as photoanodes, while ZnO is stable only as a photocathode (*p*-ZnO). Cu_2O is generally prone to electrochemical corrosion [3].

Suppression of photocorrosion of semiconductor photoelectrodes in water splitting can be achieved by the addition of electrode corrosion inhibitors. A second method is coating of a thin film of metal oxides with a conducting polymer which protects the electrode from decomposition, or a thin film of catalysts which enhances the rate of electron transfer to the redox species on the electrode surface.

1.3.4. Efficiency measurements

The most important figure of merit for a water splitting cell is the efficiency with which solar energy is converted into chemical potential energy stored in the form of hydrogen molecules. The cell efficiency is determined by the light absorption and utilisation characteristics of the semiconductor photoelectrodes. The overall photoconversion efficiency is referred to as the ratio of the maximum energy output acquired from hydrogen to the incident solar energy [3].

The total incident irradiance (P_t) is given by:

$$P_t = \int_0^\infty P(\lambda) d\lambda \tag{1.7}$$

where $P(\lambda)$ is the incident irradiance at wavelength λ (units $Wm^{-2}\,nm^{-1}$).The absorbed photon flux at wavelength λ, $I(\lambda)$ (units $m^{-2}.nm^{-1}.s^{-1}$) relates the spectral radiance by:

$$I(\lambda) = \frac{P(\lambda)\lambda}{hc} \tag{1.8}$$

The spectral photon flux is related to the water photoelectrolysis applications as absorption of one photon produces at most one electron-hole pair and excess photon energy (difference between the photon energy and the required energy to split water) is lost.

The overall photoconversion efficiency η of a water splitting cell with a bias voltage can be defined as the difference between the energy stored as hydrogen and

the energy input from power supply, which is then divided by the light energy input (P_t). The corresponding formula is given by [40]:

$$\eta = j_p\left(V_{rev}^o - V_B\right)/P_t \tag{1.9a}$$

where j_p is the photocurrent produced per unit illuminated area (units A.cm^{-2}), V_{rev}^o the standard reversible potential, which is 1.23 V vs NHE for the water splitting reaction, V_B the bias voltage measured between the working and counter electrodes. If there is no external voltage applied, the efficiency is based on the following formula [41]:

$$\eta = j_p V_{rev}^o / P_t \tag{1.9b}$$

The overall photoconversion efficiency of water photoelectrolysis can also be expressed by [42]:

$$\eta = j_p\left(V_{rev}^o - \left|V_{meas} - V_{aoc}\right|\right)/P_t \tag{1.10a}$$

and

$$\eta = j_p\left(\left|V_{meas} - V_{coc}\right| - V_{rev}^o\right)/P_t \tag{1.10b}$$

for a semiconductor photoanode and photocathode, respectively, where V_{meas} is the potential of the working electrode measured relative to a reference electrode and V_{aoc} and V_{coc} are the photoanode and photocathode potentials at open circuit conditions, respectively. Since the external voltage is applied and the photocurrent flows across the working and counter electrodes, the power supply is the product of the photocurrent and the applied voltage between these two electrodes (i.e., V_B), which has to be subtracted when calculating the efficiency [43-46]. Therefore, in either two or three-electrode geometry, a voltage measured between the working and counter electrodes should be used as the bias voltage in calculating any meaningful cell efficiency [47].

The performance of a water splitting cell is also evaluated by the incident-photon-to-electron conversion efficiency (*IPCE*). The *IPCE* is defined by the number of electrons produced by light in the external circuit divided by the

number of incident photons and given by [48]:

$$IPCE(\lambda) = j_p(\lambda)/[eI(\lambda)] \quad (1.11a)$$

where $j_p(\lambda)$ is the photocurrent density at wavelength λ. Substituting $I(\lambda)$ in Eq. 1.11a with Eq. 1.8, one obtains:

$$IPCE(\lambda) = \left(\frac{hc}{e}\right)\left(\frac{j_p(\lambda)}{P(\lambda)\lambda}\right) \quad (1.11b)$$

IPCE generally is measured at a bias voltage associated with the maximum photoconversion efficiency.

1.4. α-Fe_2O_3

1.4.1. Properties of hematite

Since the report of water splitting undertaken by Fujishima and Honda in 1972 using a TiO_2 photoanode illuminated with UV light [49], the use of semiconductor photoelectrodes for solar hydrogen production has been extensively investigated involving various metal oxide semiconductors such as SnO_2 [50], WO_3 [51-53], ZnO [54-60], Cu_2O [61, 62], CuO [63, 64], TiO_2 [29, 45, 65-68], $SrTiO_3$ [69, 70], and non-oxide semiconductors such as GaAs [71], InP [72], CdS [73]. One of the most promising photoelectrodes identified for water splitting applications is hematite (α-Fe_2O_3). Hematite is a thermodynamically stable crystallographic phase of iron oxide with the corundum hexagonal close packed crystal structure [74]. It has an indirect band gap of around 2.2 eV and a donor concentration of 2.5 x 10^{17} cm^{-3} [3]. α-Fe_2O_3 is an insulator at room temperature with specific resistance of $\rho \sim 10^{12}$ Ω.cm [75]. A detailed study of structural, optical and electrical properties of pure hematite was conducted by Glasscock, et al and the results can be accessed in the reference [74].

1.4.2. Mechanism of charge transport

Charge transport through the hematite lattice was theoretically studied by Iordanova et al [6]. The hematite lattice is shown as an alternation of iron bilayers and oxygen

layers parallel to the (001) basal plane in a hexagonal unit cell as described in Fig. 8. Fe^{III} atoms within each bilayer have parallel spins, while adjacent bilayers have opposite spins. Electrons are able to move by hopping through Fe^{II}/ Fe^{III} valence interchange within the iron bilayers (*n-type* conductivity), while electron transport

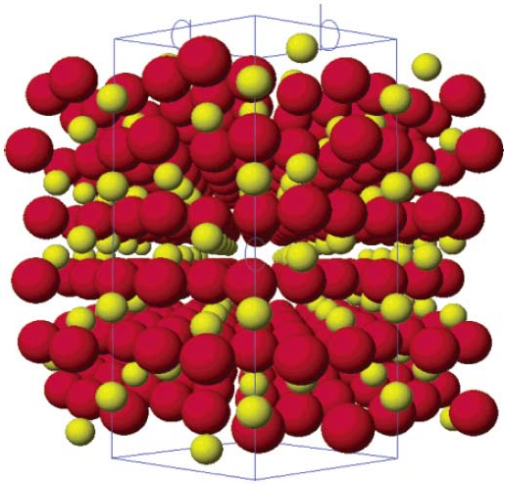

Figure 8. Model of the α-Fe_2O_3 crystal lattice viewed in the [110] direction with an alternation of iron bilayers and oxygen layers parallel to the (001) basal plane in a unit cell (iron, yellow; oxygen, red; hexagonal unit cell, blue), reproduced from *Iordanova* [6].

between neighboring iron bilayers is spin forbidden by Hund's rules. Therefore, the conductivity along the (001) basal plane is four orders of magnitude higher than that along the [001] direction. Conductivity along [001] is attributed to hole transfer by hopping through Fe^{III}/Fe^{IV} valence interchange between neighboring iron bilayers (*p-type* conductivity) although this process encounters a larger activation barrier than within the iron biplayers. The behavior of hematite with light illumination in aqueous media can be explained as follows. Photogenerated holes are located in 'd' orditals of α-Fe_2O_3 which forms narrow bands. The low hole mobility is ascribed to the strong coupling with the lattice phonons during the hopping process in the narrow 'd' bands [3]. For absorption of photons at long wavelengths (e.g., the absorption coefficient (α) of 1.6 x 10^7 m^{-1} at 500 nm), electron-hole pairs are created deep in the semiconductor bulk (about 100 nm) and far away from the electrolyte interface. The low mobility and short diffusion length of minority holes result in a high probability

of recombination of charge carriers, which can be prevented by application of more positive potential for transfer of more conduction band electrons out of the material, that is, by increasing the energy of the photoproduced electrons [76]. The few holes that reach the surface through the acceleration in the space charge layer will be faced with the slow charge transfer kinetics at the interface, which is due to an energy mismatch between the acceptor 'd' orbitals of Fe^{IV} and the donor 'p' orbitals of hydroxide in solution [77]. For absorption of photons at short wavelengths, electron-hole pairs are created in the outer part of the material where there exists a depletion layer [3].

1.4.3. Advantages and disadvantages

α-Fe_2O_3 is considered as an ideal material for photoelectrochemical water splitting and selected as the semiconductor photocatalyst in this project due to many pleasant features. First, as an *n-type* semiconductor, α-Fe_2O_3 has a relatively narrow band gap and thereby makes use of a large fraction of the solar spectrum. This allows the absorption of all UV light and most of the visible light from 295 nm up to band-gap wavelength of 564 nm, which comprises approximately 40% of incident solar radiation at AM 1.5 [78]. Moreover, it is naturally abundant on the earth and thus a low cost semiconductor material. It is nontoxic and environmentally friendly. Last, α-Fe_2O_3 is stable in most electrolytes at pH > 3 [79]. Although the reported theoretical maximum efficiency of α-Fe_2O_3 for photoelectrolysis of water is 12.9% [80], the reported photoconversion efficiencies to date are much lower than the theoretical maximum efficiency as well as the target efficiency of 10% [81]. The poor conversion efficiency of α-Fe_2O_3 has been attributed to a number of factors including: the low absorption coefficient, especially in the region between 450 and 610 nm due to an indirect band-gap transition [13, 82], the slow kinetics of water oxidation by the valence band holes (0.1-1$cm.s^{-1}$ compared to 10^3-10^4 $cm.s^{-1}$ for WO_3 and TiO_2) [75, 83], the short hole diffusion length (20 nm [83], 2-4 nm [84]) as compared to that of TiO_2 (800 nm [85]), trapping of electrons by oxygen-deficient iron site [86], and low charge mobilities (an electron mobility less than 10^{-2}-10^{-1}

$cm^2.V^{-1}.s^{-1}$ has been reported and the mobility of holes is lower than that of electrons [87]), leading to a high electron-hole recombination rate [8], and the conduction band edge of the material below the H^+/H_2 redox potential (hence an external bias is required) [29].

1.4.4. Approaches

In order to overcome these limitations of α-Fe_2O_3 and improve its efficiency for water splitting, several approaches have been employed including a thin-film structure, nanostructuring, doping with substitutional elements, and others. In the following, reports on photocatalytic water splitting with hematite photoelectrodes relating to these aforementioned approaches in the literature are reviewed, including synthesis techniques of hematite photoelectrodes due to the dependence of the photoelectrochemical behavior of this material on its method of synthesis.

1.4.4.1. Thin film structure

The electron-hole recombination caused by the low mobility of charge carriers and the short diffusion length of minority charge carriers can be decreased by reducing the distance that photogenerated electrons and holes need to travel. There exists an optimal film thickness where the resistivity of the semiconductor and the light absorption reach optimum values. The photoresponse in semiconductor electrodes is expected to be a maximum value by the following equation [88]:

$$X_o \approx \alpha^{-1} \approx W \qquad (1.12)$$

where X_o α, and W are the film thickness, absorption coefficient of light, and width of the space charge layer, respectively. In accordance with Eq. 1.12, most of the incident photons should be absorbed inside the space charge layer and film thickness should not be greater than the width of the space charge layer [89].

Hematite thin films each with thickness (ca. 60 nm) below that of the space charge region, were successively stacked and in contact with solution with light passed through each electrode using 0.5 M Na_2SO_4 and NaOH (pH 13) under one sun

illumination. Under similar conditions, the photocurrent of these stacked hematite electrodes (1.6 $mA.cm^{-2}$) increased by over three times relative to that of a thick hematite electrode (ca. 1 μm; 0.5 $mA{\cdot}cm^{-2}$) [90, 91]. Hence, it was demonstrated that the charge carrier recombination could be minimised for hematite photoelectrodes by fabricating films of thickness below the width of the space charge layer.

The use of undoped and Cu/Zn doped hematite thin films and pellets prepared by spray pyrolysis (SP) and sol-gel method, respectively using iron nitrate as the precursor in photoelectrolysis of water has been investigated by Satsangi [92]. It was demonstrated that iron oxide thin films exhibited better photoresponse relative to pellets. This was, probably, due to the smaller grain size in films leading to higher surface area to volume ratios and due to smaller transverse resistance of the films introduced in the path of photocurrent resulting from smaller thickness as compared to pellets.

Spray pyrolysis of a 0.1 M $FeCl_3$ ethanolic solution containing 0.1 M HCl onto tin oxide coated conducting glass substrates at 340 ^{o}C in air for a range of spray times between 10 and 40 s has been reported for the fabrication of hematite thin-film photoanodes. Fig. 9 shows that the hematite thin films prepared by spraying for 10 s exhibited the lowest photocurrent densities under both front and back illumination, reflecting a lack of absorption of light for the small amount of material. Between 20 and 40 s of spray time, the photocurrent density of the thin films decreased with increasing spray times (i.e., thickness) under both illumination, reflecting a short diffusion length of minority holes and low charge mobility [7].

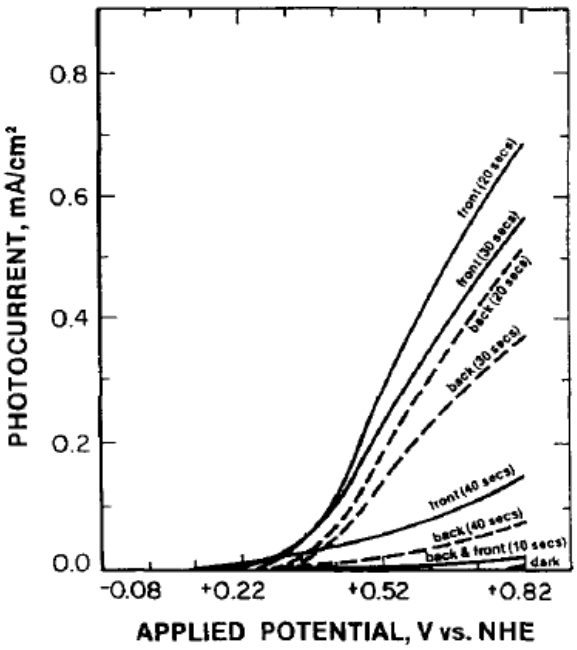

Figure 9. Photocurrent density of hematite thin film photoanodes prepared by spraying for different length of spray time shown in parenthesis, as a function of applied potential under front and back illumination conditions, reproduced from *Majumder* [7].

1.4.4.2. Nanostructuring

Given a thin-film structure, nanostructuring techniques can be employed to address drawbacks of hematite such as the poor light absorption and the electron-hole recombination losses in the bulk and at the surface. Preparation and application of nanocomposite and nanostructured hematite electrodes in water splitting are discussed in detail in this section.

A nanocomposite electrode, in principle, is able to improve its performance by increasing the active volume of material for photon absorption while reducing the distance that holes and electrons need to travel in the high-resistivity semiconductor to participate in water oxidation and reduction, respectively [8]. A nanocomposite hematite photoelectrode comprises a thin layer of hematite semiconductor deposited on a nanostructured substrate with a very high surface area. The conduction band edge of the substrate materials must lie below that of the hematite to allow efficient electron transport across the hematite/substrate interface. Last, the substrate should

have a larger band gap than hematite in order not to compete with the light absorption [8, 82, 93].

Undoped and Si-doped α-Fe_2O_3 thin films deposited onto two nanostructured, ZnO nanowires and TiO_2 nanotubes grown on indium doped tin oxide (ITO) coated conducting glass by filtered arc deposition have been reported [8]. The composite photoelectrode design and charge transfer mechanism were shown in Fig. 10. It was demonstrated that the quantum efficiencies of the nanocomposite photoanodes were

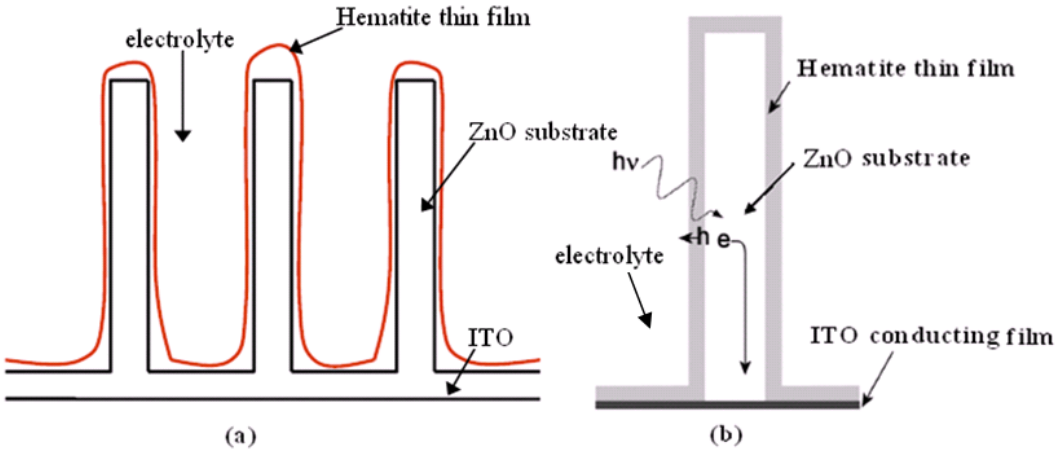

Figure 10. Schematic representation of the nanocomposite hematite electrode design: a) cross section of an array of hematite coated ZnO nanowires in electrolyte, b) charge transfer mechanism described in a single hematite deposited ZnO nanowire where photons are absorbed by the hematite thin film and photoproduced electrons efficiently travel through the ZnO nanowires to the ITO conducting substrate and holes migrate to the semiconductor/electrolyte interface in a short distance, reproduced from *Glasscock* [8].

lower than the equivalent thin films though the absorption of long wavelength photons was improved. The lower efficiencies of the composite hematite electrodes with ZnO nanowires as substrate were attributed to the negative conduction band edge of ZnO as compared to hematite. For TiO_2 nanotubes, the lower photocurrent was probably due to the formation of a nonohmic contact at the interface between α-Fe_2O_3 and TiO_2.

In the literature, the nanostructured hematite thin films used for this application include hematite thin films with a structure of nanocrystalline, nanosheet, nanopore, nanorod, etc.

Nanocrystalline thin-film semiconductors are commonly composed of a three dimensional network of inter-connected nanoparticles showing novel optical and electrical characteristics relative to that of a bulk, thick or thin film semiconductor [94, 95]. In a thin-film semiconductor photoelectrode, a space charge region is formed at the semiconductor/electrolyte interface. Photoproduced electrons and holes are separated by an internal electric field formed at this region. In contrast, in a nanocrystalline semiconductor photoelectrode, the individual nanoparticles are unable to form a space charge region as the diameter of individual nanoparticles in the film (~100 nm [9, 41]) is considered to be too small to permit the formation of a space charge layer (about 1 μm thick [3]) [96]. Therefore, the charge separation and transport in the nanocrystalline thin film is determined by the kinetics of holes at the electrode/electrolyte interface (i.e., the diffusion of holes) other than an internal electric field [97].

Photoelectrochemical properties of nanocrystalline thin-film electrodes of α-Fe_2O_3 on ITO glass substrates prepared by doctor-blading of 45 nm diameter hematite colloid have been investigated by Qian and coworkers [9]. The thicker film resulted in a poor photoresponse for short wavelength light. The mechanism of photocurrent generation and the electron concentration gradient within the electrode under illumination was depicted in Fig. 11. In this nanocrystalline thin-film

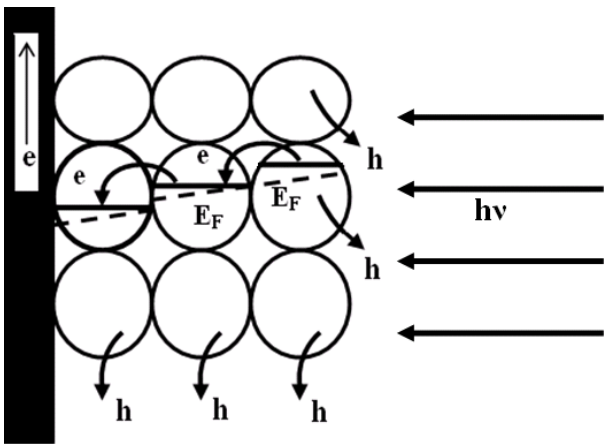

Figure 11. Schematic representation of the charge separation and transport within the hematite nanocrystalline thin film during illumination, reproduced from *Qian* [9].

electrode, the electrolyte was able to penetrate through the nanoparticles up to the surface of the back contact and thus the electrode/electrolyte interface occurred at each nanoparticle. A lower photocurrent was obtained from the thicker film as an increased charge recombination occurred at a great number of grain boundaries during the charge transport through the film to the back contact. Also, a higher electric resistance from the thicker film was another factor for the loss of charge [98]. Upon frontside illumination of the thicker film with short wavelength light, most of the charge carriers were generated relatively far from ITO substrate so the electrons were subject to more recombination loss during the transport through the film.

Nanocrystalline thin films of hematite photoanodes coated on conducting tin-oxide glass substrates were prepared by spray pyrolysis of a $FeCl_3.6H_2O$ ethanolic solution. Under a 50 $mW.cm^{-2}$ illumination from a Xe lamp in a 1 M NaOH aqueous solution, a photocurrent density of 3.7 $mA.cm^{-2}$ at 0.7 V/SCE was obtained from the hematite thin-film photoanodes under the optimum conditions. Moreover, a total photoconversion efficiency of 4.92% and a practical photoconversion efficiency of 1.84% at 0.2 V/SCE at pH 14 were obtained from the optimal thin films [41].

α-Fe_2O_3 thin-film photoanodes having a mesoscopic leaflet type structure coated on FTO substrates have been prepared by ultrasonic spray pyrolysis (USP) of 0.02 M ferric acetylacetonate in ethanol at a substrate temperature of 420 ^oC. The hematite thin films prepared by USP showed much higher photoactivity than those prepared by conventional spray pyrolysis. These mesoscopic hematite thin films comprised of 100 nm-sized platelets with a thickness of 5-10 nm. These nanosheets were oriented perpendicularly to the FTO substrate with their flat surface exposing (001) facets. This nanostructure was beneficial that it provided a very short distance for holes to travel to the electrode/electrolyte interface before the recombination with electrons, which overcame the short diffuse length of holes [99].

Thin films of hematite nanoparticles synthesised by oxidising Fe films in air at

600 ^{o}C for 30 s exhibited a highly porous structure (see Fig. 12). The hydrogen evolution rate was twice that of the hematite granular films prepared by oxidising Fe films in air at 600 ^{o}C over 1h, and two orders of magnitude higher than that reported for hematite powders [100, 101]. The charge transfer and separation was improved by the porous structure [102, 103]. Nanoporous α-Fe_2O_3 films have also been synthesised by potentiostatic anodisation of iron foil and annealing in N_2 at 400 ^{o}C. The pore diameters ranged from 50 to 250 nm with a pore depth of ca. 500 nm depending on the applied potential and electrolytic composition.

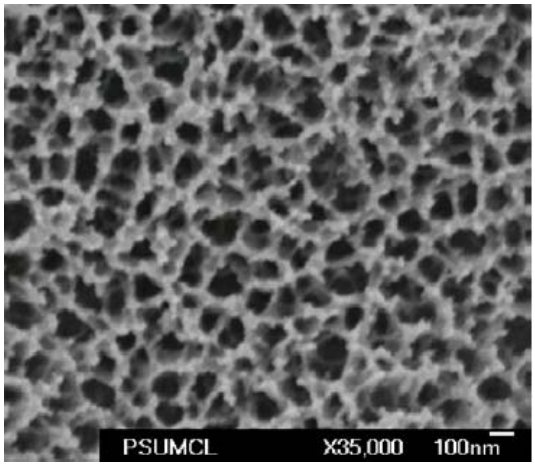

Figure 12. SEM image of a hematite film anodised in 1% HF + 0.5% NH_4F + 0.2% HNO_3 in glycerol at 10 C at 90 V, reproduced from *Prakasam* [10].

Mesoporous α-Fe_2O_3 has been of particular interest recently because confining d-electrons to the thin walls between pores can provide novel magnetic, electrical, and optical characteristics. Moreover, the high internal pore surface area can cause new and unique catalytic properties [104]. In addition to application of mesoporous iron oxide thin films to electrodes in lithium batteries [105], (magneto)optical devices [106], and catalysts [107], the use of mesoporous hematite thin films in photoelectrolysis of water has not been reported to date. Herein, we survey the literature on the fabrication of mesoporous α-Fe_2O_3 thin films.

Mesoporous hematite synthesis usually involves the use of a soft template (a surfactant, e.g. alkyl amine) around which the mesoporous hematite is formed or a hard template (e.g., mesoporous silica) within the pores of which the mesoporous

hematite is produced, and then the template is removed by dissolution. In both case, an iron precursor solution is required for the formation of hematite. Furthermore, if the temperature range within which the target phase forms does not coincide with the stability range of the template, the hematite phase may not be obtained [104]. Mesoporous α-Fe_2O_3 thin films with crystalline walls were synthesised by the evaporation-induced self-assembly (EISA) process and a subsequent heat treatment at 450 ^oC using block copolymer templates, i.e., poly(isobutylene)-block-poly(ethylene oxide) (PIB-PEO). Hematite thin films with the well-order mesostructure, comprised of pores with an average diameter of ca. 10 nm were shown in Fig. 13. Disordered and ordered mesoporous hematite thin films

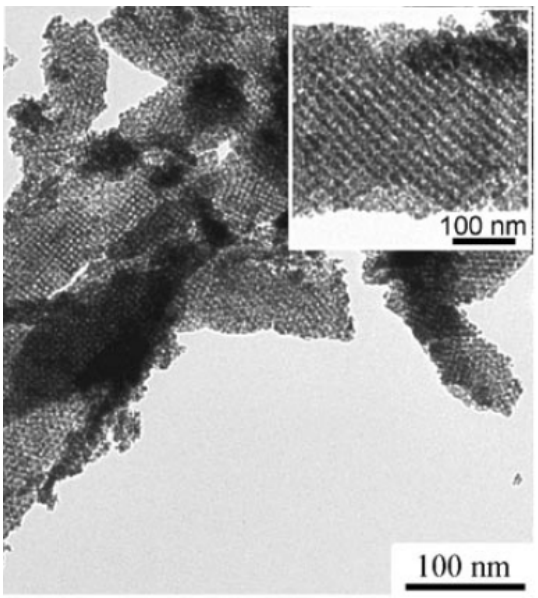

Figure 13. Transition electron microscopy (TEM) image of a mesoporous α-Fe_2O_3 thin film; the inset is a magnification, reproduced from *Brezesinski* [11].

with amorphous walls have been prepared using soft templating methods [108-112]. Mesoporous α-Fe_2O_3 thin films have been synthesised using $Fe(NO_3)_3.9H_2O$ in ethanol as precursor and mesoporous silica as hard template which was removed by dissolution in NaOH. Hematite thin films with an ordered mesoporous structure and crystalline walls that exhibited a near-single crystal-like order were found with a pore size and wall thickness of 3.85 nm and 7 nm, respectively [113].

Hematite thin films with a structure of nanorods have been reported, which avoided recombination losses at grain boundaries between the nanoparticles compared to nanostructured hematite thin films consisted of interconnected spherical particles as shown in Fig. 14 [12, 86].

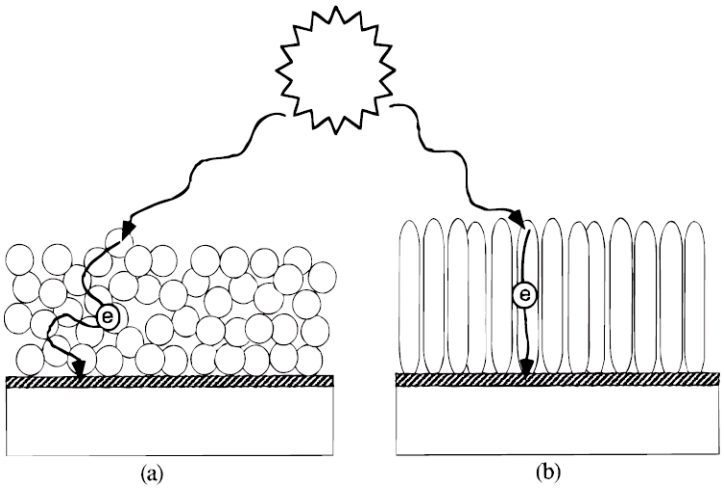

Figure 14. Schematic drawing of electron transport through a) spherical particles and b) nanorods, reproduced from *Beermann* [12].

An IPCE of about 8 % was obtained by these hematite electrodes at 350 nm without any applied voltage under 0.1 $mW.cm^{-2}$ of backside illumination (substrate-electrode (SE)) in two-electrode set-up [86]. Hematite thin films consisting of oriented nanorods coated onto transparent conductive glass substrates have been studied in PEC cells. Under frontside and backside illumination from a 450 W Xe lamp, IPCE increased by a factor of 100 and 7, respectively, in contrast to those from hematite thin films with spherical particles [114].

Nanowires prepared by thermal oxidation of Fe metal sheet. A photocurrent density of 1.32 $mA.cm^{-2}$ at 0.0V/SCE and a photoconversion efficiency of 1.69% at 0.70 V vs V_{aoc} (electrode potential at open circuit conditions) [115]. With respect to a structure of nanotube arrays, due to a high surface area and efficient charge transfer, titania nanotubes have been extensively studied in water splitting [116-118]. However, hematite thin films with a nanotubular structure have not been applied to this area in the literature. The fabrication of hematite nanotudes and application of

them to some other fields (e.g., gas sensor, lithium ion battery) has been common in the literature [119-121].

1.4.4.3. Doping

Doping α-Fe_2O_3 thin films with heteroatoms as a means of improving performance in water splitting has been extensively studied in recent years. Incorporation of dopants into hematite is expected to improve the electrical properties and photocatalytic activity, and change the microstructure and morphology of the material. A great number of dopant species have been introduced into hematite in order to enhance performance including Ag^{+}, Mg^{2+}, Cu^{2+}, Zn^{2+}, Al^{3+}, Rh^{3+}, Au^{3+}, Cr^{3+}, Si^{4+}, Ge^{4+}, Ti^{4+}, Pt^{4+}, and Nb^{5+} [8, 13, 25, 75-77, 92, 115, 122-136]. As an *n-type* semiconductor with trivalent state on Fe, any doping atom with valence state below +3 introduced into hematite renders it an *p-type* semiconductor, whereas a *n*-type semiconductor is obtained for valence state of dopant species above +3. Since application of Si, Ti and Zn-doped α-Fe_2O_3 photoelectrodes to photogeneration of hydrogen has been reported in the literature recently, we will discuss the effect of these dopant atoms on the performance of the hematite thin-film photoelectrodes.

5 wt% Si-doped hematite thin film electrodes deposited on conducting glass substrates have been prepared by Glasscock, et al [135] using reactive magnetron sputtering in an attempt to evaluate how the dopant affected the photocatalytic performance of the hematite electrodes. The Si-doped hematite electrodes obtained a much higher photocurrent density than the undoped hematite electrodes though the Si-doped hematite electrodes seemed to be highly amorphous and have a high level of surface disorder. It was shown that the increased photocurrent was attributed to reduction of charge recombination as a result of an improvement of the charge-transfer coefficient at the surface and possible passivation of the grain boundaries by the dopant.

Transluscent Si-doped and undoped hematite thin films coated on transparent conducting oxide (TCO)-coated glass were fabricated by two different methods, ultrasonic spray pyrolysis (USP) and atmospheric pressure chemical vapour

deposition (APCVD) with iron (III) acetylacetonate ($Fe(AcAc)_3$) and iron pentacarbonyl ($Fe(CO)_5$), respectively as precursor and TEOS as silicon dopant. It was demonstrated that the morphology and photoresponse of the films was significantly affected by silicon doping. The USP Si-doped hematite thin films exhibited a changed morphology and increased photocurrent compared to USP undoped hematite electrodes (see Fig. 15a). The APCVD Si-doped samples obtained a photocurrent density of up to 1.45 $mA.cm^{-2}$ at 1.23 V vs RHE and exhibited a dendritic morphology (See Fig. 15b). APCVD undoped hematite electrodes obtained a photocurrent density of below 1 $\mu A.cm^{-2}$ at the same applied potential and less developed branches at the surface (see Fig. 15b, inset). The improvement of the photocurrent was explained through the increased electrical conductivity resulting from silicon acting as an electron donor in the hematite lattice. The grain size was reduced to a level that was of the order of the hole diffusion length in the presence of silicon. Also, the smaller grain size increased the specific surface area of the photoanode [76].

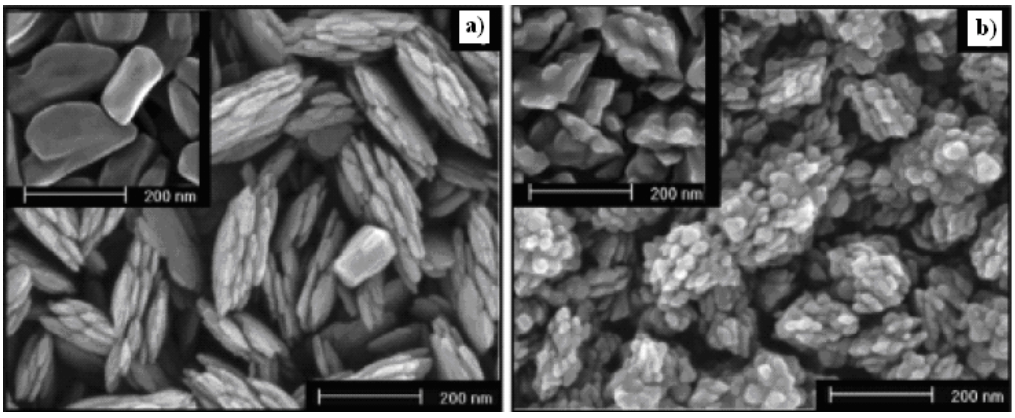

Figure 15. Typical HR-SEM images of Si-doped hematite films on TCO prepared from a) USP and b) APCVD: (a, Inset) USP undoped hematite thin films, (b, Inset) APCVD undoped hematite thin films, reproduced from *Cesar* [13].

Si-doped Fe_2O_3 thin films deposited onto conductive glass substrates have been prepared by spray pyrolysis of a $Fe(AcAc)_3$ solution as precursor and different amounts of TEOS as dopant at a substrate temperature of 450 ^oC. The highest photocurrent density of 0.33 $mA.cm^{-2}$ was obtained for 0.2 at.% Si-doped Fe_2O_3

compared to 0.04 $mA{\cdot}cm^{-2}$ for undoped hematite thin films under the same condition [137].

5 at.% Ti-doped Fe_2O_3 thin films prepared by reactive magnetron sputtering showed much higher PEC activity than the undoped material. In addition to changes in conductivity by doping, the Ti dopants acted as the same as Si dopants, which has been discussed previously [135].

Ti-doped Fe_2O_3 thin-film photoanodes fabricated from the spray pyrolysis produced a photocurrent density of 4.05 $mA.cm^{-2}$ at 0.45 V vs NHE for 5 at.% Ti-doped Fe_2O_3 in contrast to 0.78 $mA{\cdot}cm^{-2}$ at the same applied potential for undoped thin films. The enhancement of photoresposne of the films was most likely due to the increased electrical conductivity and the stabilisation of oxygen vacancies by the Ti^{4+} ions [138].

Zn-doped Fe_2O_3 thin films deposited on FTO glass substrates by spray pyrolysis from an aqueous solution of $Fe(NO_3)_3.9H_2O$ and $Zn(NO_3)_2.6H_2O$ with a range of dopant concentrations from 0.5 to 10.0 at.% at a substrate temperature of 350 ^oC have been investigated by Kumari and coworkers [130]. Under illumination a maximum photocurrent density of ~0.64 $mA.cm^{-2}$ was obtained at 0.7V/SCE for 5 at.% doping concentration as compared to c.a. 0.1 $mA.cm^{-2}$ at 0.7V/SCE for undoped thin films.

Other Zn-doped Fe_2O_3 thin films coated on ITO glass substrates prepared by spray pyrolysis from an ethanolic solution of $FeCl_3.6H_2O$ and $Zn(NO_3)_2.6H_2O$ at a substrate temperature from 663 K to 668 K have been reported. It was shown that zinc turned the indirect band gap of hematite to a direct band gap due to formation of $ZnFe_2O_4$. Also, a much higher photoresponse was ascribed to higher acceptor densities which reduced the resistivity of the film [131].

In summary, *n*-type behavior has been obtained for Si/Ti-doped Fe_2O_3 thin films, whereas *p-type* properties have been shown by Zn-doped Fe_2O_3 thin films. The doping has been demonstrated to significantly improve the photocatalytical activity. The mechanism for enhanced photoresponse has been discussed for each of the

dopants in terms of crystal structure, morphology, electrical conductivity anddonor/acceptor concentrations.

1.4.4.4. Others

Some other methods used to overcome the disadvantages of hematite are surface modifications, electrolytic composition modification, and a tandem-cell configuration.

Surface modifications have included the deposition of metal oxide semiconductors, electrocatalysts, metallic dots, nonmetal atoms, and swift heavy ion irradiation on the surface of a hematite thin film. A thin layer of WO_3 deposited on the surface of a hematite thin film which was coated on a FTO glass substrate has been fabricated by spin-coating. A higher visible light response and IPCE of WO_3/Fe_2O_3 were obtained relative to WO_3 or α-Fe_2O_3 alone when applied to water splitting. A proposed mechanism was that the photogenerated electrons transported more easily than in WO_3 or α-Fe_2O_3 alone. Hence, the interface between WO_3 and α-Fe_2O_3 effectively separated electrons and holes, contributing to the improvement of the performance in water splitting [139]. Electrocatalysts such as ruthenium oxide [7] and Au particles [126] have been deposited on hematite thin-film electrodes by spray pyrolysis and sol-gel, respectively, in order to improve the performance in water splitting. The ruthenium oxide deposition reduced the onset potential of the hematite film by 120 mV but did not increase the photoresponse. Au particles on the surface enhanced the photocurrent by catalytically promoting the hole transfer from the valence band to electrolyte. A catalytic cobalt monolayer deposited on the surface of a hematite thin film has been demonstrated to increase the photocurrent density slightly compared to a hematite thin film without treatment with cobalt [76]. For deposition of metallic dots on the surface of hematite thin films, metallic Cu and Zn have been reported to be deposited on the surface of hematite thin films by thermal evaporation technique. An enhanced photoresponse of the electrodes has been observed [92, 140]. Fluoride has been deposited on the surface of Ti-doped α-Fe_2O_3 by Hu and cowokers [141] to negatively shift the flat-band potential and allow the

water splitting reaction to occur without an external bias.

The slow kinetics of water oxidation by holes can be addressed by modifying the electrolyte composition. The mechanism for the improvement of photoresponse is explained that the addition of a substance into electrolyte can bypass the relatively slow oxygen evolution reaction to supply a source of electrons to rapidly consume photogenerated holes [142]. Duret et al. [99] have reported a large increase of the photocurrent and a decrease of the onset potential for the mesoscopic hematite thin films made by ultrasonic spray pyrolysis in the presence of H_2O_2 in the electrolyte. A similar effect on hematite thin-film electrodes has been reported by Itoh et al [90]. They explained that the photogenerated holes oxidised H_2O_2 ten times faster than H_2O. Moreover, glucose [142] and iodide [114] have been added to the electrolyte in order to enhance the photoresponse of the hematite electrodes in water splitting.

A tandem-cell configuration can be used to eliminate the required bias so as to improve the efficiency for photoelectrolysis of water, such as p/n Fe_2O_3 tandem cells, hematite/dye-sensitised solar cell (DSSC) tandem cells. For the use of hematite/DSSC tandem cells in water splitting, a Si-doped Fe_2O_3 thin-film photoelectrode combined with two DSSCs in series which provided the required potential for hydrogen evolution by absorbing the red part of the solar spectrum transmitted by hematite electrode has been reported to exhibit a solar-to-chemical conversion efficiency of 2.1 % [13]. For further details refer to the reference [36].

1.5. Rational for research

The α-Fe_2O_3 photoelectrodes used for water splitting in this project have several important properties. First, the material has a thin-film structure, thus minimising the effect of rapid electron-hole recombination due to a short hole diffuse length and low charge mobilities. Second, the material exhibits an inverse opal structure (i.e., three-dimensionally ordered macroporous (3DOM) structure). The inverse opal structure produces a high surface-to-volume ratio and unique optical properties [143]. The high surface-to-volume ratios can enhance surface reaction by providing photogenerated holes with a number of reactive sites to participate in water oxidation.

In addition, the walls between the macropores have thicknesses corresponding to tens of nanometers, which can greatly shorten the distance photogenerated holes need to travel to reach the electrode/electrolyte interface (see Fig. 16). Inverse opals that have a spatially periodic structure resulting in a photonic crystal with a photonic band gap (PBG). These properties can exclude the passage of photons of a chosen range of wavelengths and therefore confine, control, and manipulate photons in three dimensions [143, 144]. The band gap can be fixed to a given wavelength by controlling the pore size in the inverse opals [144]. The inverse opal structure plays an important role in transport of the water molecules in the interconnected pore system and of charge carriers in the interconnected solid skeleton [143]. To further enhance the photocatalytic activity, two different dopant atoms, Ti and Zn are introduced into the material.

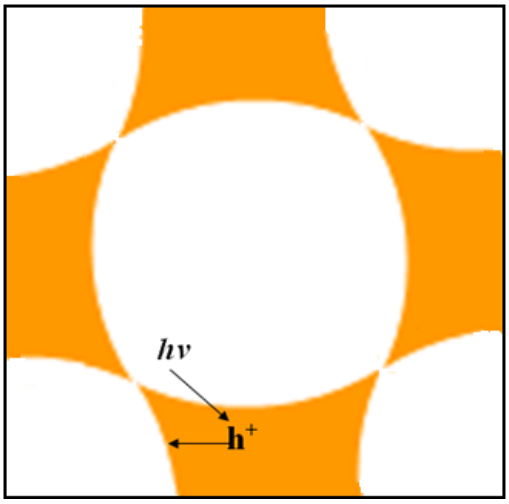

Figure 16. Schematic representation of an inverse opal structure where there is a short distance for a photogenerated hole to travel to reach the electrolyte.

Inverse opals or 3DOM materials can be prepared by template-based methods using arrays of monodisperse spherical particles [145]. In this case, poly(methyl methacrylate) (PMMA) spheres are used as templates. Fig. 17 is the SEM image of

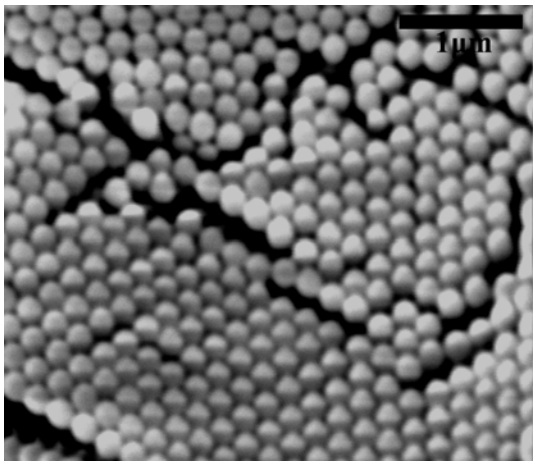

Figure 17. SEM image of highly ordered PMMA spheres.

PMMA spheres which exhibit a high degree of periodicity in three dimensions. PMMA exhibits a face-centered cubic (*fcc*) crystal structure where the volume ratio of spheres to voids is 74% to 26% (see Fig. 18) [14]. To prepare inverse opals, the void spaces between spheres in the PMMA template are filled with fluid precursors which penetrate the template and are converted into a solid. Removal of the templating spheres leaves an interconnected solid skeleton that surrounds the air holes left in the original locations of the PMMA spheres (see Fig. 19). The skeletal walls surround regular macropores that are interconnected through windows at the points where the original spheres touched [143]. The preparation process of an

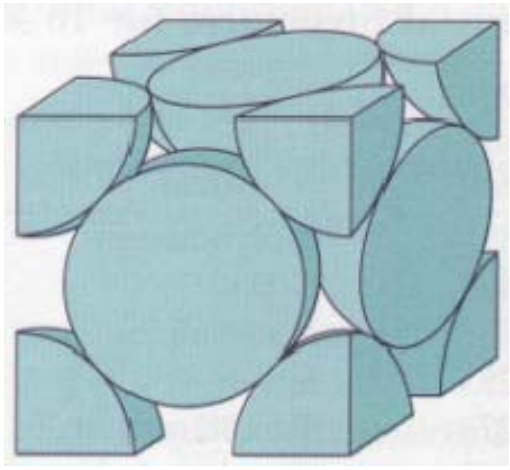

Figure 18. A hard sphere unit cell representation of the face-centered cubic structure, reproduced from *William* [14].

inverse opal structured hematite thin film is presented in Fig. 19. PMMA mixed with an iron nitrate solution is deposited on a glass substrate. After the solution is infiltrated into the voids between the templating spheres and then dried, the coating is calcined to form hematite and then remove the PMMA temple so as to obtain a highly ordered inverse opal structured hematite thin film.

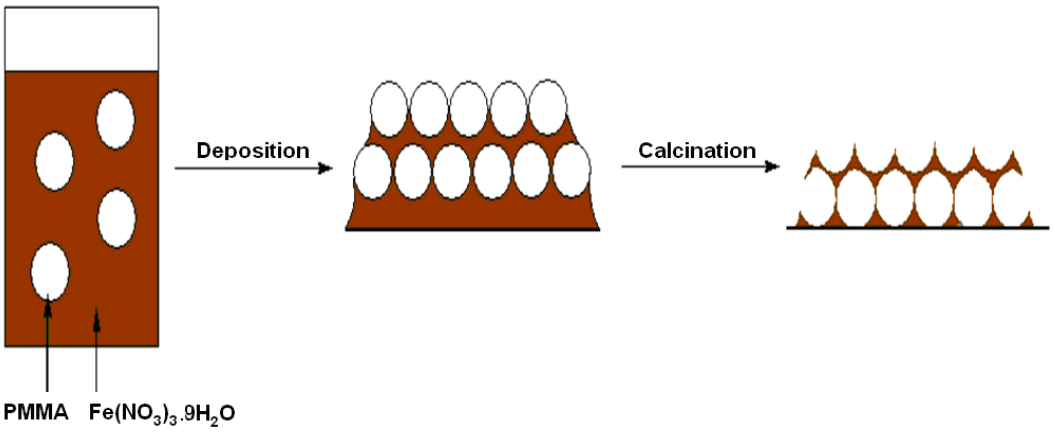

Figure 19. Preparation process of a hematite thin film with an inverse opal structure.

In this project, undoped, and Ti and Zn doped Fe_2O_3 thin films deposited on FTO glass substrates are prepared by doctor balding and spray pyrolysis. These thin films are characterised by the use of XRD, SEM, EDX, UV/Vis spectroscopy, TGA, and photoelectrochemical measurements.

2. Experimental

2.1. Synthesis of poly(methyl methacrylate) templates

PMMA spheres were prepared by an emulsion polymerisation as described elsewhere [146]. Briefly, 500 mL of de-ionised water and 40 mL of methyl methacrylate (MMA) (Aldrich, 99%) were mixed and heated to 85^{o}C with moderate stirring in a round bottom flask in an oil bath at a hotplate (IKA) under a N_2 flow. This setup also contained a reflux condenser and temperature probe. To this mixture, 0.2343 g of 2,2'-Azobis (2-methylpropion-amidine) dihydrochloride initiator (Aldrich, 97%) was added by dissolving in a small amount of H_2O (c.a. 10 mL) and allowed to react for 1 hour at 85^{o}C. The resulting polymer spheres were immediately filtered through a plug of cotton wool, followed by drying under an air stream at ambient temperature until dry (3 - 5 days). These prepared PMMA spheres were used as templates for the production of inverse opals.

2.2. Synthesis of titanium dopant precursor

Titanium oxychloride ($TiOCl_2$) used as one of the titanium dopant precursors was synthesised by the partial hydrolysis of titanium (IV) tetrachloride in a hydrochloric acid solution. A 2 M HCl solution was obtained from the dilution of an HCl solution (Ajax Finechem, 32%). 75 mL of the HCl solution (2 M) was added to a Schott bottle and cooled in an ice-H_2O with magnetic stirring. Following distillation of $TiCl_4$ (Aldrich, 99.9%), 4 mL of the freshly distilled $TiCl_4$ was immediately added to the cooled HCl solution with a syringe. A solution of $TiOCl_2$ (c.a. 0.5 M) in 2 M HCL was obtained after stirring overnight at ambient temperature. The $TiOCl_2$ solution was stable for approximately one month before the hydrolysis of $TiOCl_2$ and the occurrence of a white precipitate, titania.

2.3. Cleaning regime of conducting glass slides

All the FTO conducting glass slides (2.5 cm X 2.5 cm, Dyesol TEC15 glass plates, 2.3 mm thick, 15 Ω/sq) to be used as substrates were cleaned with Teepol

detergent in tap water; rinsed in acetone, tap water and finally de-ionised water; wiped with Kimwipes papers and dried in a stream of air.

2.4. Doctor-blading

Hematite thin films deposited on a conducting glass substrate were prepared in methanol and water using a simple doctor blade technique following the literature method by Bjorksten [147]. An FTO glass substrate was covered with adhesive tapes (for typical office use, thickness: 20 μm [148]) on two parallel edges and one end to control the thickness of the films and to provide an area for electrical contact. A solution of precursors and dopants was added to the one end of the glass slide covered with the adhesive tapes, which were spread across the surface via the two parallel edges using a pipette tube, by a single application of the tube.

An FTO glass slide deposited with a coating was heated in a furnace (Modutemp Pty, Ltd) from ambient temperature to 200 ^{o}C at 1 ^{o}C/min, isothermal for 2 hours, then heated to a higher temperature at 1 ^{o}C/min and isothermal again for 2h. All the calcination processes for undoped and doped α-Fe_2O_3 films employed this scheme. Since the electrical resistivity of the FTO glass slides increases with an increase of temperature and a calcination temperature over 650 ^{o}C causes the damage of the glass slides, all the coatings are calcined at a temperature below 650 ^{o}C.

2.4.1. α-Fe_2O_3 thin films

Varying amounts of $Fe(NO_3)_3.9H_2O$ (ACS reagent, Sigma, 98%) from 0.159 to 1.272 g were dissolved in 10 mL of methanol and then mixed with 1 g of finely ground PMMA spheres. These solutions were stirred with a magnetic bar on a hotplate (IKA) for 1 hour. A few drops of each of these solutions were spread across the surface of an FTO glass slide by doctor blading. After drying at ambient temperature, these slides were calcined at 450 ^{o}C.

Other solutions containing 0.159 g of $Fe(NO_3)_3.9H_2O$ in 2 mL of either methanol, deionised water or 2 M HCl aqueous solution were mixed with 0.25 g of finely ground PMMA spheres under magnetic stirring for 1 h. A few drops of each of these

solutions were spread onto an FTO glass slide by doctor blading. These slides were calcined at 450 ^{o}C or 550 ^{o}C.

A blank FTO glass slide was heated to 550 ^{o}C at 1 ^{o}C/min and isothermal for 2 h. This blank FTO glass slide was used for comparative purposes.

Table 3 summarised the sample name, solvent name, volume of solvent, mass of iron nitrate and PMMA, and calcination temperature. In subsequent sample names, FE refers to $Fe(NO_3)_3.9H_2O$, ME for methanol, WA for deionised water, HC for HCl, and DB for doctor blading. For these samples prepared from 10 mL of methanol, the number in the sample names relates to a ratio of iron nitrate and PMMA (w/w). For example, '1' corresponds to a ratio of 0.159, '2' to a ratio of 0.318 (i.e. 2 x 0.159 = 0.318), and '3' to a ratio of 0.477 (i.e. 3 x 0.159 = 0.477). For these samples prepared from 2 mL of solution, the calcination temperature is indicated in the sample names, e.g., 450 referring to 450 ^{o}C.

Sample name	**Solvent (mL)**	**$Fe(NO_3)_3.9H_2O$ (g)**	**PMMA (g)**	**Temp. (^{o}C)**
FEMEDB-1	methanol (10)	0.159	1	450
FEMEDB-2	methanol (10)	0.318	1	450
FEMEDB-3	methanol (10)	0.477	1	450
FEMEDB-4	methanol (10)	0.636	1	450
FEMEDB-5	methanol (10)	0.795	1	450
FEMEDB-6	methanol (10)	0.954	1	450
FEMEDB-8	methanol (10)	1.272	1	450
FEMEDB-450	methanol (2)	0.159	0.25	450
FEWADB-450	H_2O (2)	0.159	0.25	450
FEWADB-550	H_2O (2)	0.159	0.25	550
FEHCDB-550	HCl (2)	0.159	0.25	550

Table 3. Synthetic parameters and conditions of α-Fe_2O_3 thin films deposited on FTO glass slides by doctor blading

2.4.2. Ti-doped Fe_2O_3 thin films

Approximately 0.155 g of $Fe(NO_3)_3.9H_2O$ was dissolved in 1 ~ 4 mL of 2 M HCl containing 2.5 at.% Ti from the $TiOCl_2$ solution. The solution was added to 0.25 g of finely ground PMMA with magnetic stirring for 1 h. A few drops of the resultant solution were spread onto FTO glass slides by doctor blading. All slides were calcined at 550 ^oC while the slides prepared from the $Fe(NO_3)_3.9H_2O$ solution (0.0775 $g.mL^{-1}$, 2mL) were calcined at three different temperatures from 450 to 600 ^oC as indicated

2.5 at.% Ti-doped Fe_2O_3 thin films with double layers were prepared by doctor blading of an $Fe(NO_3)_3.9H_2O$ solution in 2 M HCl (0.0775 $g.mL^{-1}$, 2mL) containing 2.5 at.% of $TiOCl_2$ and 0.25 g of finely ground PMMA spheres onto FTO glass slides using double layers of adhesive tapes. Then these slides were calcined at 550 ^oC.

A solution of $Fe(NO_3)_3.9H_2O$ in 2 M HCl (see Table 4) containing 1 to 20 at.% of $TiOCl_2$ (except 2.5 at.%) was added to 0.25 g of finely ground PMMA spheres with magnetic stirring for 1 h. A few drops of the solution were spread onto FTO glass slides by doctor blading. These slides were calcined at 550 ^oC.

2.4.3. Zn-doped Fe_2O_3 thin films

An $Fe(NO_3)_3.9H_2O$ aqueous solution containing 5 to 20 at.% of Zn from $Zn(NO_3)_2.6H_2O$ (see Table 4) was added to 0.25g of finely ground PMMA spheres with magnetic stirring for 1 h. A few drops of the resultant solution were spread onto FTO glass slides by doctor blading. These slides were calcined at 550 ^oC.

Zn-doped samples at a doping level between 5 and 20 at.% were also prepared using 2 M HCl.

Table 4 summarised the sample name, solvent name, volume of solvent, dopant name, atomic percent of dopant, mass of $Fe(NO_3)_3.9H_2O$ PMMA, calcination temperature and number of layers of adhesive tapes. In these sample names, TI refers to $TiOCl_2$,

HC to HCl, and ZN to $Zn(NO_3)_2.6H_2O$. For Ti-doped Fe_2O_3 thin films, the doping level, calcination temperature, volume of solution, and number of layers of adhesive tapes were indicated in the sample names, e.g., 2.5TI-550-2-1L refers to 2.5 at.% Ti-doped Fe_2O_3 thin films prepared by 2 mL of solution and calcination at 550 ^oC using 1 layer of adhesive tapes. Meanwhile, for Zn-doped Fe_2O_3 thin films, a doping level was indicated in the sample names, e.g., ZNWADB-5 refers to 5 at.% Zn-doped Fe_2O_3 thin films prepared by doctor blading of aqueous solution.

Sample name	**Solvent (mL)**	**Dopant (Atom%)**	**$Fe(NO_3)_3.9H2O$ (g)**	**PMMA (g)**	**Temp. (^oC)**	**No. of Layers**
1TI-550-2-1L	2 M HCl (2)	$TiOCl_2$ (1)	0.157	0.25	550	1
2.5TI-550-2-1L	2 M HCl (2)	$TiOCl_2$ (2.5)	0.155	0.25	550	1
5TI-550-2-1L	2 M HCl (2)	$TiOCl_2$ (5)	0.151	0.25	550	1
10TI-550-2-1L	2 M HCl (2)	$TiOCl_2$ (10)	0.143	0.25	550	1
20TI-550-2-1L	2 M HCl (2)	$TiOCl_2$ (20)	0.127	0.25	550	1
2.5TI-450-2-1L	2 M HCl (2)	$TiOCl_2$ (2.5)	0.155	0.25	450	1
2.5TI-600-2-1L	2 M HCl (2)	$TiOCl_2$ (2.5)	0.155	0.25	600	1
2.5TI-550-1-1L	2 M HCl (1)	$TiOCl_2$ (2.5)	0.155	0.25	550	1
2.5TI-550-4-1L	2 M HCl (4)	$TiOCl_2$ (2.5)	0.155	0.25	550	1
2.5TI-550-2-2L	2 M HCl (2)	$TiOCl_2$ (2.5)	0.155	0.25	550	2
ZNWADB-5	H_2O (2)	$Zn(NO_3)_2.6H_2O$ (5)	0.151	0.25	550	1
ZNWADB-10	H_2O (2)	$Zn(NO_3)_2.6H_2O$ (10)	0.143	0.25	550	1
ZNWADB-20	H_2O (2)	$Zn(NO_3)_2.6H_2O$ (20)	0.127	0.25	550	1
ZNHCDB-5	2 M HCl (2)	$Zn(NO_3)_2.6H_2O$ (5)	0.151	0.25	550	1
ZNHCDB-10	2 M HCl (2)	$Zn(NO_3)_2.6H_2O$ (10)	0.143	0.25	550	1

ZNHCDB-20	2 M HCl (2)	$Zn(NO_3)_2.6H_2O$ (20)	0.127	0.25	550	1

Table 4. Synthetic parameters and conditions of Ti and Zn-doped Fe_2O_3 thin films deposited on FTO glass slides by doctor blading.

2.5. Spray pyrolysis

Hematite thin films were prepared by spray pyrolysis following the literature method by Sartoretti [138]. A portion of an FTO glass slide was covered with aluminum foil to keep it free from deposition for use as an electrical connection. A Protek Corp. K-type Thermocouple (TM-1300K, HCT112) was used to measure and maintain the temperature of the glass substrate placed on a hotplate (Industrial Equipment & Control Pty Ltd). A spray solution was sprayed onto the glass slide at a temperature between 400 and 450 ^oC at a distance of 50 cm from the slide with a carrier gas of N_2 using an air brush (Gison, Model No: R-134a). A spray of 10 s was followed by a wait of 5 min to maintain a constant substrate temperature. This procedure deposited one layer. The spraying continued until the desired number of layers was achieved.

2.5.1. Ti-doped Fe_2O_3 thin films

30 mL of 0.128 M $Fe(NO_3)_3.9H_2O$ and 0.00337 M $TiOCl_2$ in 2 M HCl aqueous solution was prepared. The solution was sprayed onto FTO glass slides by spray pyrolysis. 3, 6 and 12 layers of deposition were prepared. Then these slides were calcined at 550 ^oC for 2 h. Table 5 summarised the sample name, solvent name, concentration of $Fe(NO_3)_3.9H_2O$, dopant name and concentration, number of layers and calcination temperature for the 2.5 at.% Ti -doped Fe_2O_3 thin films by spray pyrolysis. In subsequent sample names, SP refers to spray pyrolysis. The number of layers of deposition was indicated in the sample names, e.g, TIHCSP-3L refers to Ti-doped Fe_2O_3 thin films with 3 layers of deposition prepared by spray pyrolysis using 2 M HCl aqueous solution.

Sample name	Solvent	$Fe(NO_3)_3.9H_2O$ (M)	Dopant (Atom%)	No. of layers	Temp. (^oC)
TIHCSP-3L	2 M HCl	0.128	$TiOCl_2$ (2.5)	3	550
TIHCSP-6L	2 M HCl	0.128	$TiOCl_2$ (2.5)	6	550
TIHCSP-12L	2 M HCl	0.128	$TiOCl_2$ (2.5)	12	550

Table 5. Synthetic parameters and conditions of 2.5 at.% Ti-doped Fe_2O_3 thin films deposited on FTO glass slides by spray pyrolysis.

2.6. Instrumentation

2.6.1. Scanning electron microscopy (SEM)

Samples were coated with a thin conductive layer of evaporated carbon using a Cressington high vacuum evaporative coater. The secondary electron images were obtained with the use of an FEI Quanta 200 SEM. The chemical composition of the films were analysed at 20 kV accelerating voltage by energy-dispersive X-ray spectrometry (EDX) on the FEI Quanta SEM fitted with an EDAX thin-window X-ray detector and microanalysis system.

2.6.2. PMMA spheres and inverse opals diameter determination

The Microsoft Office Picture Manager 2003 was applied to the measurement of the number of pixels in the scale bar of the SEM images which was obtained and used to measure the diameter of a sphere or a void of an inverse opal. Sizes of exceeding 20 spheres or voids were measured and averaged to obtain reported dimensions for a sample.

2.6.3. X-ray powder diffraction (XRD)

X-ray powder diffraction (XRD) patterns of undoped, and Ti and Zn-doped hematite thin films deposited on FTO glass slides were recorded with CuKα radiation (λ = 1.541874 Å) and parabolic mirror based parallel beam (multilayered W/Si) on a PANalytical X' Pert PRO MPD (radius: 240.0 mm) at 40 KeV and 40 mA and fixed

incidence 1.5° (Ω) from 10 to 80° (2θ) at a step size of 0.02° (2θ) with each step measured for 1.1 seconds using the proportional detector (PW3011/20) with a parallel plate collimator (acceptance angle 0.09°).

2.6.4. Crystallite size determination

The crystallite size of the undoped, and Ti and Zn-doped hematite thin films were calculated using the Scherrer equation which is given by [149]:

$$\tau = \frac{K\lambda}{B\cos\theta} \qquad \text{(Eq. 2.1)}$$

where τ is the mean size of the crystalline domains, which may be smaller or equal to the grain size, K the shape factor which has a typical value of about 0.9 and varies with the actual shape of the crystallite, λ the *x*-ray wavelength, θ the Bragg angle, and B the line broadening at half the maximum intensity which is termed full-width at half maximum (FWHM). Here, the broadening B of the sample equals to the difference between the measured broadening B_{mea} and the instrumental broadening B_{std} since the instrumental factors contribute to the width of a diffraction peak. B_{std} was calculated using LaB_6 as standard which was run in the same condition as these samples.

2.6.5. Thermogravimetric analysis (TGA) and derivative thermogravimetric analysis (DTG)

Samples (i.e., precursors) were dried in air at ambient temperature prior to the TGA and DTG analysis. The thermal decomposition of the samples was carried out in a TA® Instruments incorporated high-resolution thermogravimetric analyser (series Q500). Approximately 20-30 mg of sample was isothermal for 20 min, then heated from the ambient temperature to 1000 °C at a ramp rate of 5 °C/min in a flowing air atmosphere (80 cm^3/min), cooled down in a flowing nitrogen atmosphere (80 cm^3/min) and equilibrated at 300 °C.

2.6.6. Ultraviolet and visible spectroscopy

Optical absorption measurements of these hematite thin films were performed using a Cary 5000 UV-Vis spectrometer. The absorbance of these thin films ($log(1/R)$, where R is reflectance) was measured in the 300 - 800 nm range in a reflection mode.

2.6.7. Electronic band gap determination

Based on the UV-Vis absorbance spectra, the energy position of the absorption edge of these hematite thin films (i.e., band-gap wavelength) was determined by locating the position of the minima of numerical derivative in the plot of numerical derivative against wavelength. The electronic band gap in electron volts can be calculated using Eq. 1.1b.

2.6.8. Photoelectrochemical measurements

The photoelectrochemical performance of the films was measured using a two-electrode configuration in two different reactors. One is a 100 mL Perspex cell which is a home-made two-electrode electrochemical cell (see Fig. 20) with 0.1 M NaOH (Analytical Reagent, Chem-Supply, 99%) aqueous solution as electrolyte, a hematite thin film deposited on an FTO glass slide as the photoanode and a platinum

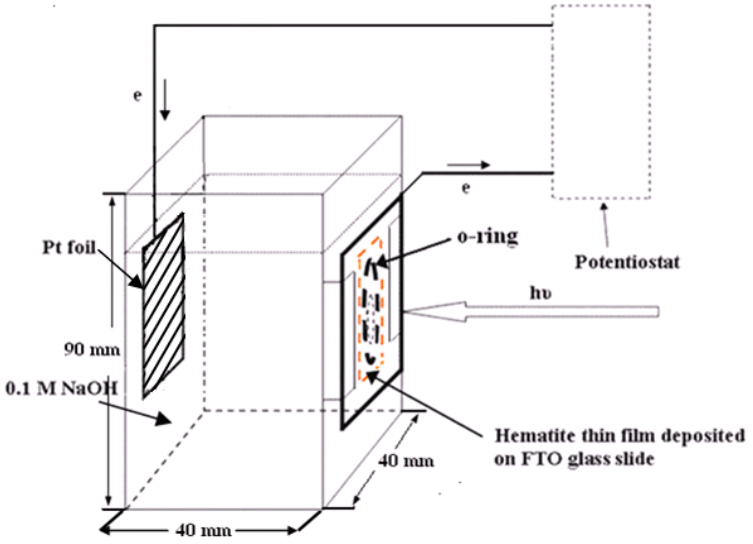

Figure 20. Schematic representation of the function of a 100 mL Perspex reactor in which a hematite thin film deposited on an FTO glass slide attached and stabilised onto an o-ring (diameter: 16.28 mm)

is used as a photoelectrode; a Pt foil is used as counter electrode; 0.1 M NaOH aqueous solution is used as electrolyte; a potentiostat is used to measure the voltage and current and apply the voltage between the working and counter electrodes; the distance between the two electrode is 40 mm.

foil as the counter electrode. The contact area between the thin-film photoanode and the electrolyte, which is also the illuminated area, is equal to the area of an o-ring with a diameter of 16.28 mm. The other is a sandwich cell (see Fig. 21) in which a hematite thin film deposited on an FTO glass slide as the photoanode is attached to the platinum coated FTO glass substrate as the counter electrode via an o-ring

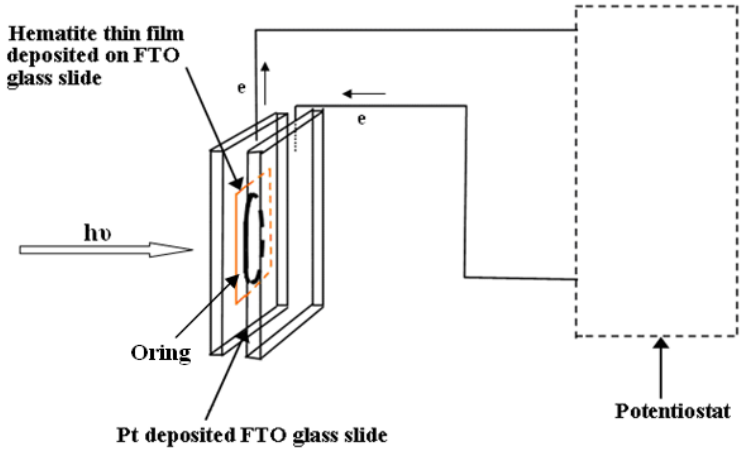

Figure 21. Schematic illustration of the function of a sandwich cell in which a hematite thin film deposited on FTO glass slide is used as the photoanode; a Pt-coated FTO glass slide is used as the counter electrode; an o-ring (diameter: 14.90 mm) is sandwiched between the two electrodes, containing 0.1 M NaOH as electrolyte; a potentiostat is used to measure the voltage and current and apply the voltage between the working and counter electrodes.

(diameter: 14.90 mm) in which 0.1 M NaOH aqueous solution was contained as electrolyte. The thickness of the o-ring is 2.20 mm. The illumination source was an AM 1.5 solar simulator (Newport Model 66902) equipped with a 150 W xenon arc lamp. The intensity of the light was calibrated at 100 $mW{\cdot}cm^{-2}$ using an optical power meter (Newport Model 1918-C). The photocurrent of the films was measured by a source-measure unit (Keithley Model 236) during a 50 $mV.s^{-1}$ scan of the bias voltage range which were also measured and applied by this instrument. The

photocurrent density (j_p), as a function of bias potential (V_B), was determined from the difference between the current measured under illumination and the current in the dark.

The IPCE was measured by passing the output from the 150 W xenon arc lamp through a grating monochromator with built-in electronic shutter (Cornerstone^{TM} 260 ¼ m) via a 50-mm diameter fused silica lens and measuring the photocurrent as a function of wavelength over the range 320-650nm. An AM 1.5 direct air mass filter (Model No. 81092) was introduced for scans at wavelengths exceeding 600 nm to eliminate artifacts from second-order diffraction. The intensity of the monochromatic light was measured with a calibrated photodiode (Oriel). The IPCE was calculated using Eq. 1.11b.

3. Results and discussion

3.1. Poly(methyl methacrylate) templates

Fig. 22 shows the surface microstructure of synthesised PMMA spheres. The periodic, regular arrangement of spheres extended over several micrometers. Well-ordered sublayers proved that the ordering extended into the whole structure. The average diameter of the spheres is 229 ± 7 nm. Therefore, the PMMA spheres exhibited a three-dimensional, long-range ordering structure.

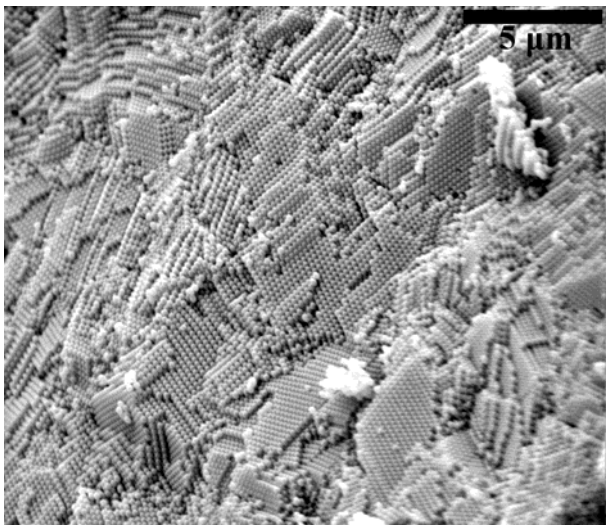

Figure 22. A representative SEM image of PMMA spheres

A study of the thermal properties of PMMA is useful to the synthesis of inverse opals of hematite to know at what temperature PMMA is expected to change its structure compared to the other components of the inverse opals. PMMA was analysed by thermogravimetric and differential thermogravimetric analysis and the results are shown in Fig. 23. One thermal decomposition step was observed, which represented the decomposition of PMMA in air and the release of CO_2 and H_2O. The mass loss occurred at 254 ^oC.

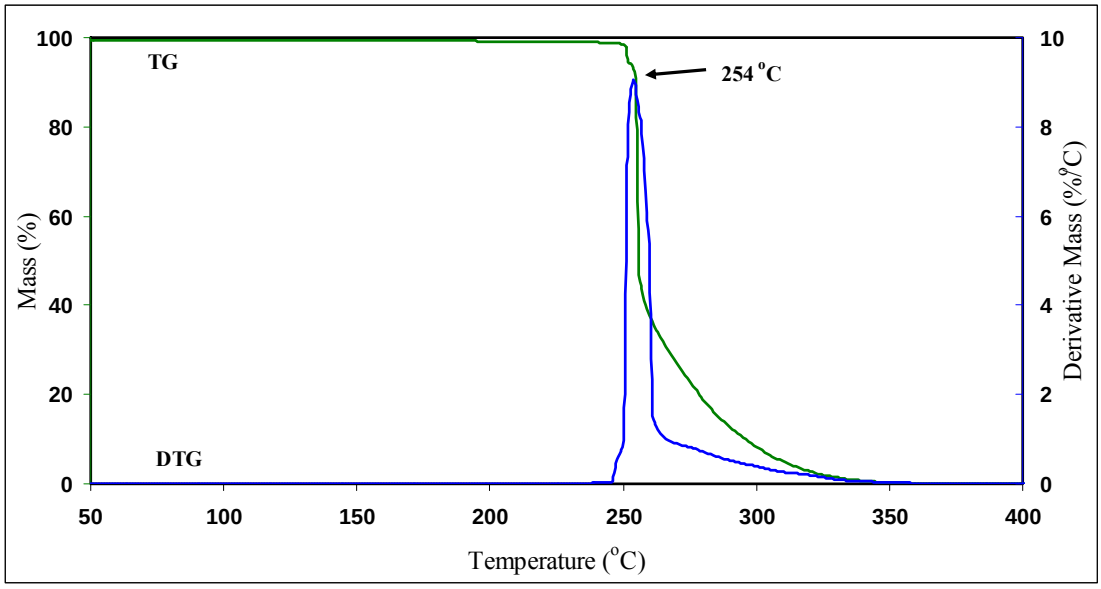

Figure 23. TGA and DTG curves of PMMA in air.

3.2. Undoped and Ti and Zn-doped Fe_2O_3 thin films by doctor blading

3.2.1. α-Fe_2O_3 thin films

3.2.1.1. X-ray diffraction

The X-ray diffraction patterns of iron oxide thin films on FTO glass substrates are shown in Fig. 24. Apart from the strong diffraction peaks from the SnO_2 coating of the glass substrates (cassiterite), the diffraction peaks of hematite (labeled 'H') were present in all the iron oxide thin films. It was thus concluded that these films prepared from doctor-blading of iron nitrate and PMMA in three different solvents, methanol, water, and 2 M HCl solution, followed by calcination at two different temperatures, 450 and 550 ^oC resulted in hematite.

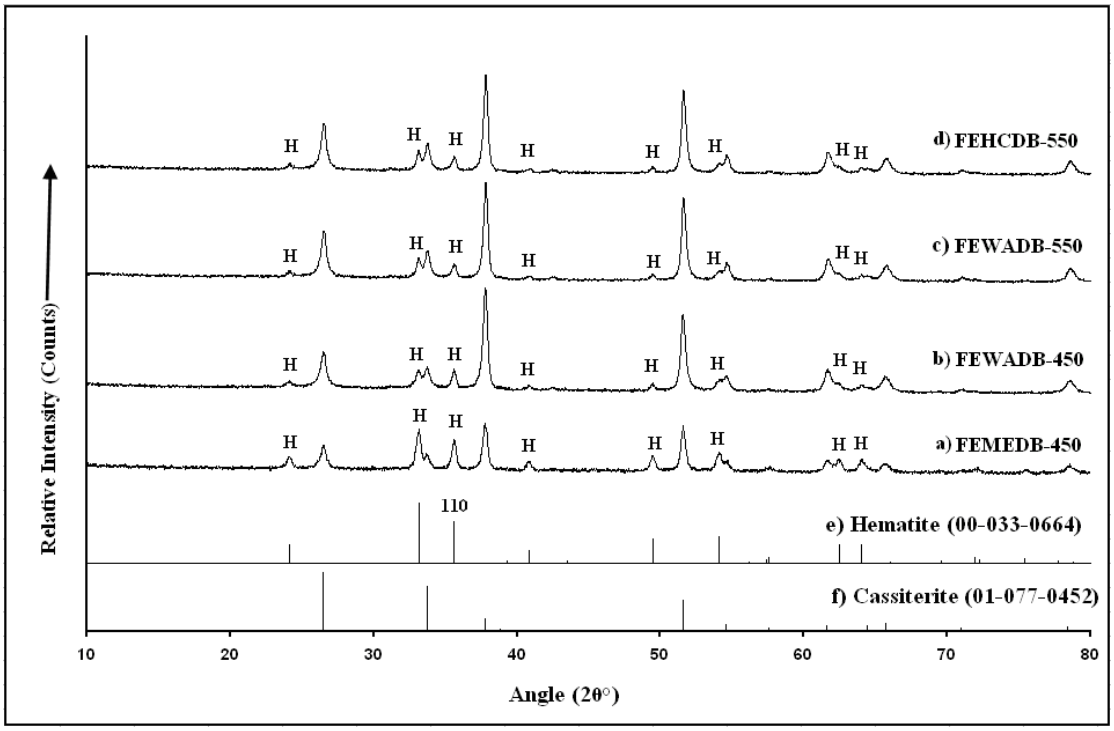

Figure 24. X-ray diffraction patterns of iron oxide thin films on FTO glass substrates, a) FEMEDB-450, b) FEWADB-450, c) FEWADB-550, d) FEHCDB-550, and e) standard powder patterns of hematite and f) cassiterite (SnO_2).

In order to calculate the crystallite sizes in the hematite thin films, the strong diffraction peak corresponding to (110) plane (see Fig. 24) was chosen. The results are shown in Table 6 below. The crystallite sizes of hematite thin films prepared in different solvents and calcined at two different temperatures were in the range between 38 and 48 nm.

Sample Name	Crystallite size (nm)
FEMEDB-450	46
FEWADB-450	38
FEWADB-550	48
FEHCDB-550	44

Table 6. Crystallite sizes of hematite thin films prepared by doctor blading.

3.2.1.2. Morphological characterisation

Fig. 25 shows the SEM results of hematite for a range of mass ratios of iron nitrate to PMMA (w/w) in methanol sintered at 450 ^{o}C. For these films with ratios of 0.159 (FEMEDB-1, Fig. 25a) and 0.318 (FEMEDB-2, Fig. 25b), very few small inverse opals were found. However, a number of highly ordered inverse opals became evident from these films with ratios of 0.477 (FEMEDB-3, Fig. 25c) and 0.636 (FEMEDB-4, Fig. 25d). Furthermore, the number of inverse opals decreased significantly for these films with ratios of 0.795 (FEMEDB-5, Fig. 25e) and 0.954 (FEMEDB-6, Fig. 25f). The inverse opals disappeared for the films with a ratio of 1.272 (FEMEDB-8, Fig. 25g). For the ratio below 0.477, iron nitrate seemed to be not enough to form inverse opals. Between 0.477 and 0.636 was the optimal range to form inverse opals with long-range order. Between 0.795 and 0.954, iron nitrate seemed to be too much. Thus, the number of inverse opals decreased gradually due to filling of the inverse opals by the extra hematite after removal of the PMMA template. For the ratio of 1.272, all of the inverse opals were completely filled by the hematite. A nonporous structure was present without the use of PMMA as shown in Fig. 25h.

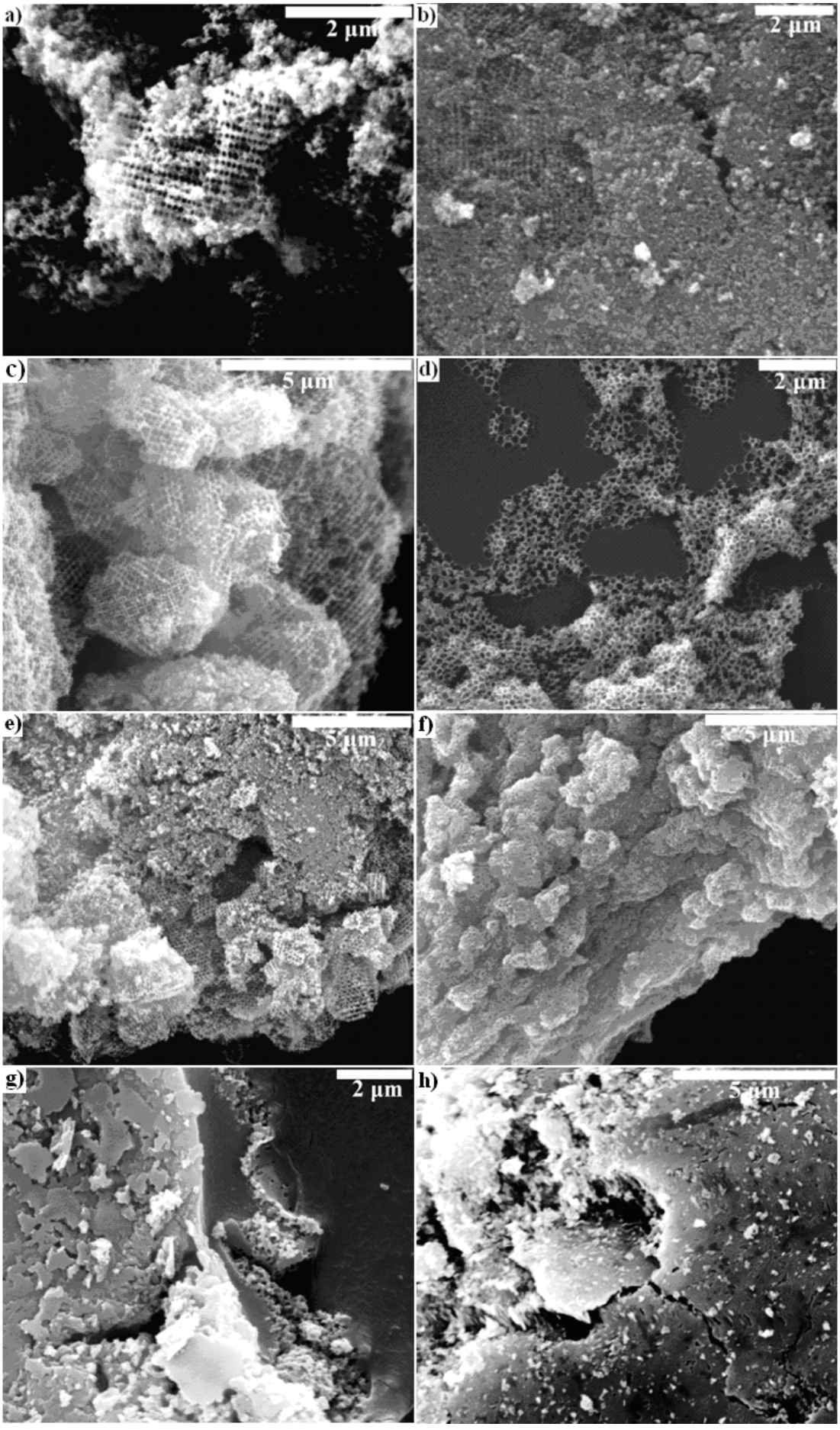
a)
2 µm
b)
2 µm
c)
5 µm
d)
2 µm
e)
5 µm
f)
5 µm
g)
2 µm
h)
5 µm

Figure 25. SEM images of α-Fe_2O_3 thin films prepared by doctor blading, with mass ratios of iron nitrate to PMMA, a) 0.159 (FEMEDB-1), b) 0.318 (FEMEDB-2), c) 0.477 (FEMEDB-3), d) 0.636 (FEMEDB-4), e) 0.795 (FEMEDB-5), f) 0.954 (FEMEDB-6), and g) 1.272 (FEMEDB-8), and h) without PMMA.

Changes in the size of inverse opals as a function of mass ratios of iron nitrate to PMMA are observed in Fig. 26 and increased from 61 ± 5 to 118 ± 11 nm when the ratio increased from 0.159 to 0.477. Then, the size of inverse opals increased from 118 ± 11 to 152 ± 6 nm more slowly when the ratio rose to 0.795, and then dropped to 92 ± 18 nm for the ratio of 0.954.

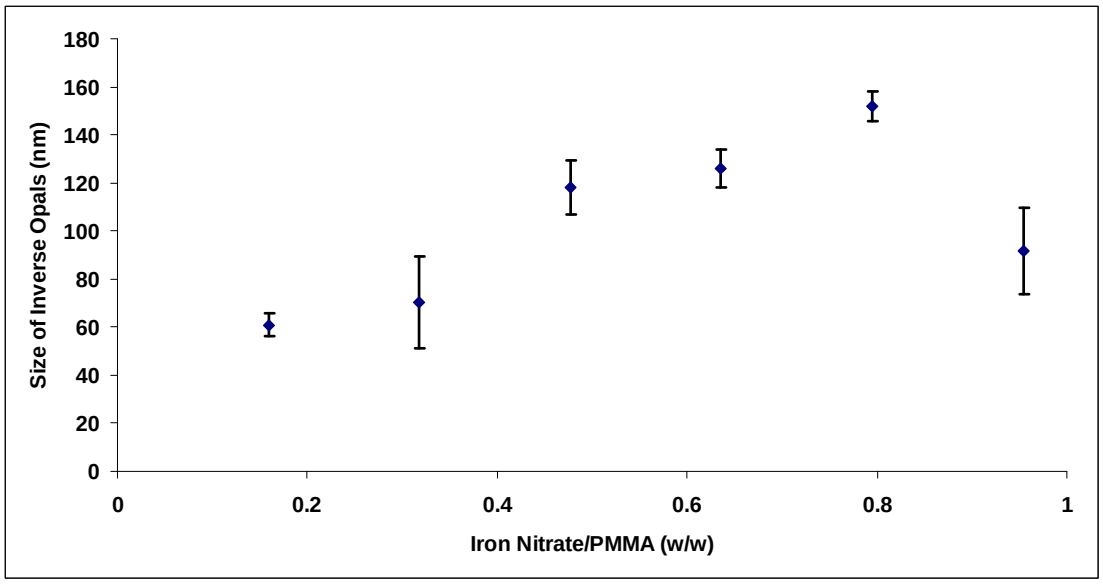

Figure 26. Changes of sizes of inverse opals with increasing iron nitrate/PMMA

Since the optimal range of ratios of iron nitrate to PMMA is between 0.477 and 0.636 for the forming of highly ordered inverse opals, the ratio of 0.636 was selected to be the optimum ratio for this work.

When hematite thin films were prepared using methanol as solvent, the films were not well adhered to the FTO glass substrate. Therefore, water was tried to use as solvent instead of methanol in the preparation of hematite thin films. When water was used as solvent, hematite thin films with an iron nitrate/PMMA ratio of 0.636 and calcined at 450 ^{o}C (FEWADB-450) formed a highly ordered inverse opal

structure as shown in Fig. 27a. The size of inverse opals was reduced to 62 ± 10 nm. The adhesion of the films is much better than that of the films with methanol as solvent. When the calcination temperature was increased to 550 ^{o}C (FEWADB-550), the adhesion of the film was further enhanced due to better sintering between the particles at a higher temperature. Also, this hematite thin film exhibited an inverse opal structure (see Fig. 27b). The average size of inverse opals was 51 ± 6 nm. When a 2 M HCl aqueous solution was used as solvent, the adhesion of the films was much better than that of the films with water as solvent. The enhancement of adhesion was probably due to the change of polarity and wetting properties of the solution by the addition of HCl. However, the inverse opal structure of the hematite thin films was completely destroyed by the addition of HCl as shown in Fig. 27c. The samples with 2 M HCl solution as solvent appeared denser than those samples with H_2O as solvent.

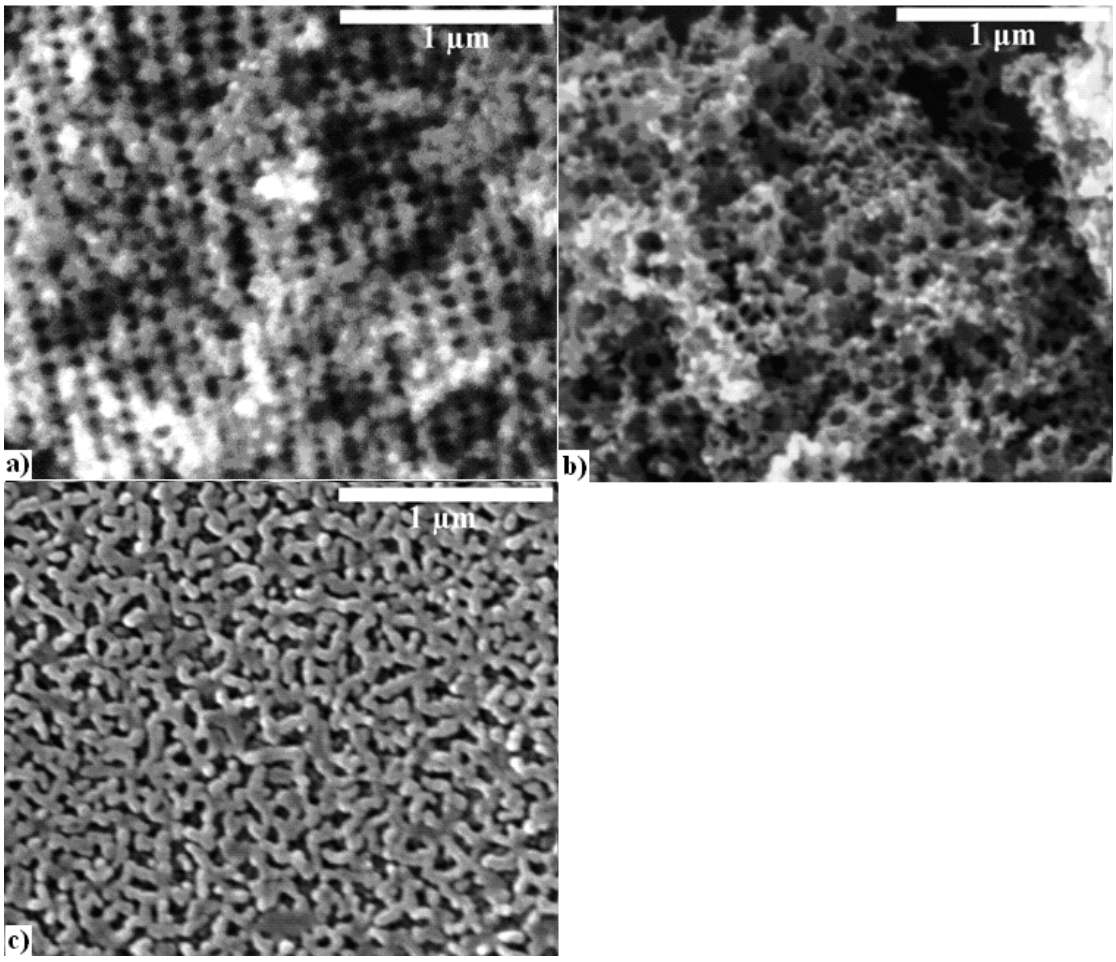

Figure 27. SEM images of hematite thin films prepared from iron nitrate and PMMA in a) aqueous

solution calcined at 450 °C (FEWADB-450) and b) 550 °C (FEWADB-550), and c) 2 M HCl calcined at 550 °C (FEHCDB-550).

3.2.1.3. Thermal analysis

The thermogravimetric and differential thermogravimetric analysis of iron nitrate is shown in Fig. 28. Three major thermal decomposition steps were observed. The mass loss in the 45 to 102 °C was attributed to the water mass loss. The mass loss at 45 °C was 33.4 % and at 102 °C was 7.69 % totaling 41.09 which based on the formula (Eq. 3.1) was in good agreement with the theoretical loss of 40.1 %. The thermal decomposition step at 133 °C was attributed to the evolution of NO_2 and O_2 and accounted for 39.11 % of the mass with the theoretical mass loss being 40.1 % based on the formula

$$4Fe(NO_3)_3.9H_2O \longrightarrow 2Fe_2O_3 + 12NO_2 + 3O_2 + 36H_2O \qquad \text{(Eq. 3.1)}$$

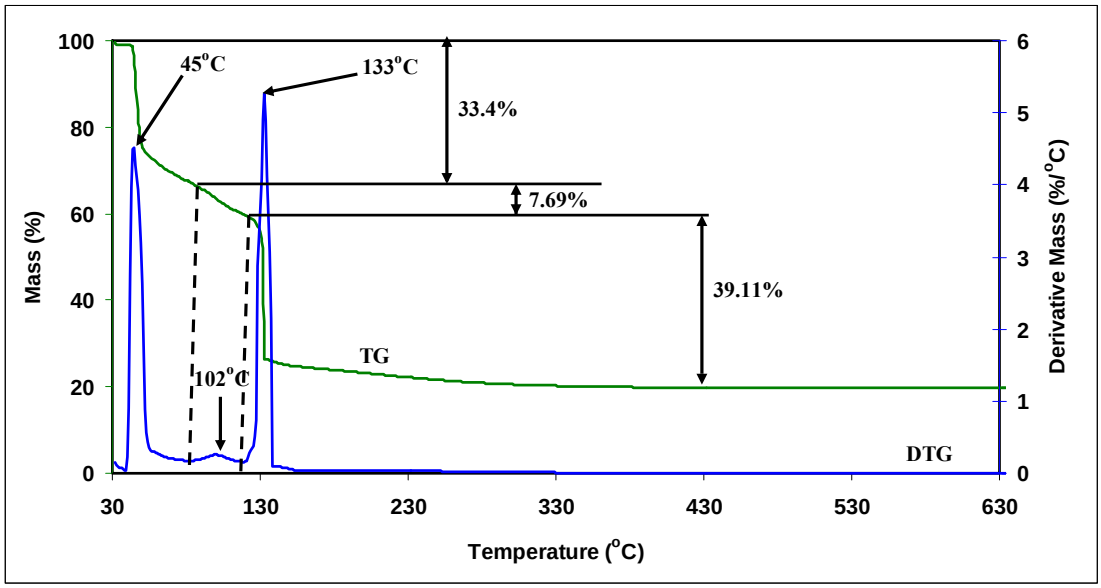

Figure 28. TGA and DTG of $Fe(NO_3)_3.9H_2O$ in air.

The thermogravimetric and differential thermogravimetric analysis of a mixture of iron nitrate and PMMA which was prepared from an aqueous solution of 0.0795 $g.mL^{-1}$ $Fe(NO_3)_3.9H_2O$ and 0.125 $g.mL^{-1}$ PMMA and dried at ambient temperature is shown in Fig. 29. Four major thermal decomposition steps were observed. The mass

loss at 30 °C was 19.82 % which is assigned to the loss of solvent (i.e. water). In other words, 80.18 % of the mixture was iron nitrate and PMMA. The mass loss of 12.94 % at 40 °C was attributed to the water loss of iron nitrate. By calculation, the mass loss of water from iron nitrate was 16.14 % (i.e., 12.94 %/80.18 %) which was in good agreement with the theoretical loss of 15.59 %. The mass loss in the 189 to 235 °C corresponded to the evolution of NO_2 and O_2 and accounted for 8.26 %. The mass loss of the gas was 10.30 % (i.e., 8.26 %/80.18%) by calculation which was in agreement with the theoretical loss of 15.59 %. The mass loss of 51.81 % at 263 °C was attributed to the decomposition of PMMA as compared to the thermal analysis of PMMA on its own (see Fig. 23). The mass loss of PMMA by calculation was 64.62 % (i.e., 51.81 %/80.18 %) which agreed well with the theoretical mass loss of 61.12 %. Therefore, compared to the thermal analysis of iron nitrate on its own, the evolution of NO_2 and O_2 occurred at higher temperatures when the mixture was burning. Iron nitrate decomposed before the decomposition of PMMA during the burning of the mixture. This order ensured the formation of inverse opals of hematite [143]. That is, iron oxide solid formed in the voids of PMMA spheres after the decomposition of iron nitrate and inverse opals of iron oxide formed after the removal of PMMA.

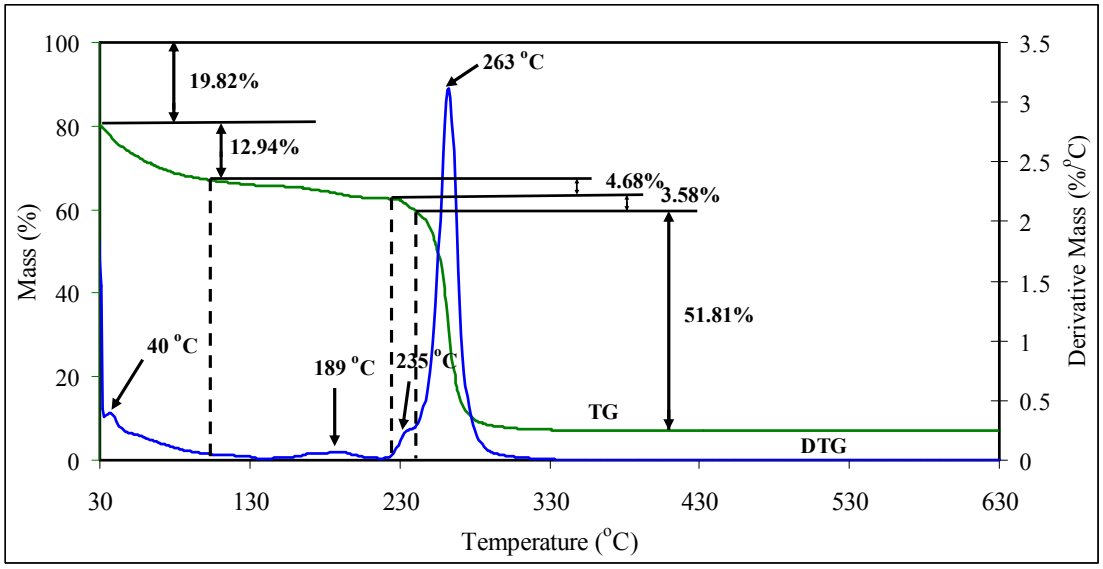

Figure 29. TGA and DTG of a dried mixture of $Fe(NO_3)_3.9H_2O$ and PMMA with H_2O as solvent in air

3.2.1.4. Photoelectrochemical properties

Hematite thin films prepared in both methanol and water and calcined at 450 ^{o}C did not show any photocatalytic response due to poor adhesion (i.e., easily scraped off by a finger), as shown in Fig. 30.

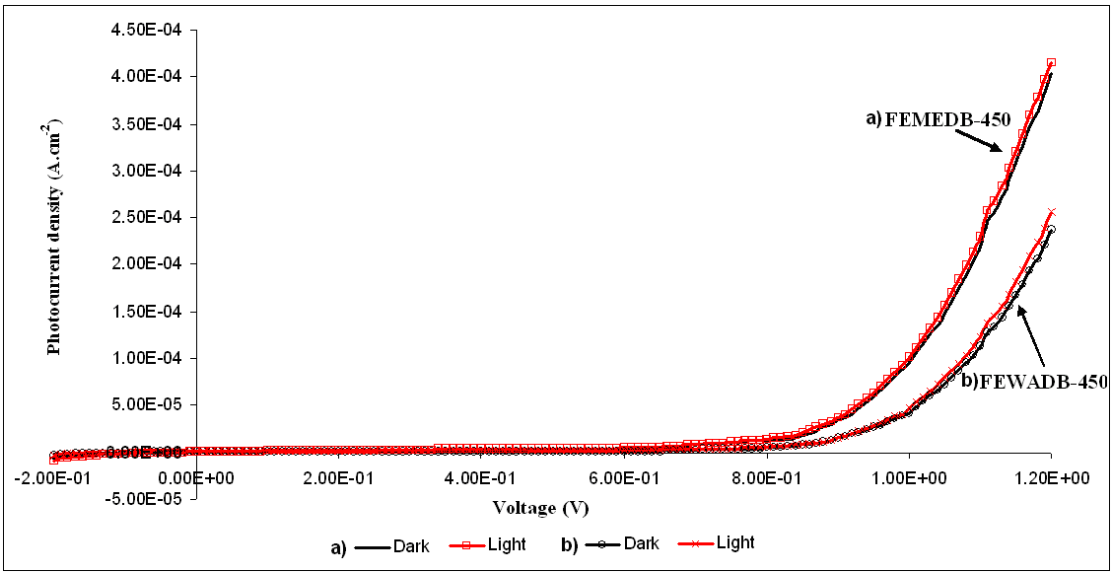

Figure 30. Photocurrent-voltage characteristics of α-Fe_2O_3 thin films prepared in both methanol and water and calcined at 450 ^{o}C, a) FEMEDB-450 and b) FEWADB-450, which were measured in darkness and under simulated sunlight in a 100 mL Perspex cell.

Fig. 31a and b show that hematite thin films prepared in both water and 2 M HCl and calcined at 550 ^{o}C did not produce photocurrent under illumination even though the adhesion of the films was enhanced significantly. Also, the blank FTO substrate did not contribute to the production of photocurrent (Fig. 31c).

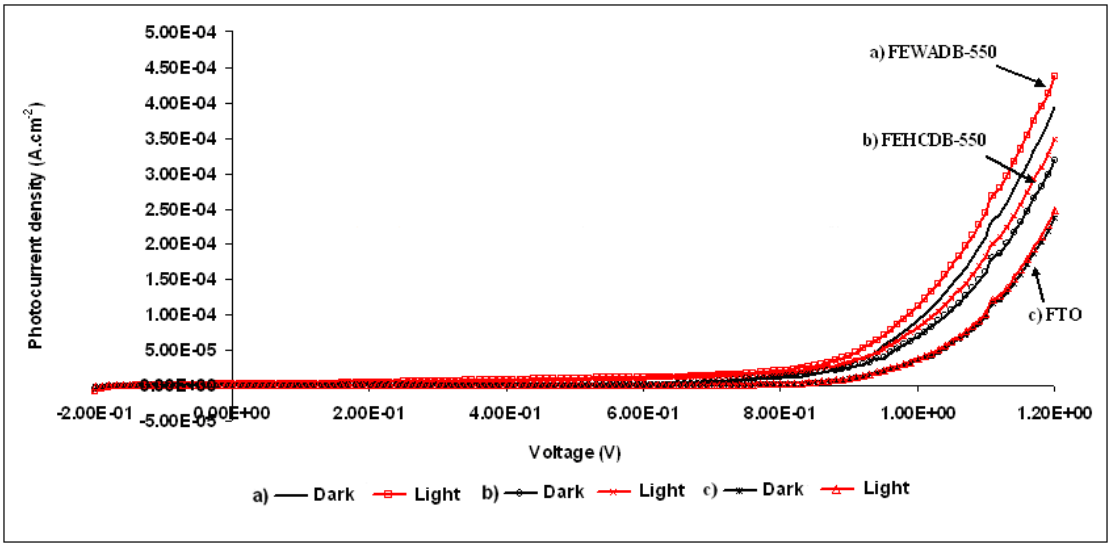

Figure 31. Photocurrent-voltage characteristics of α-Fe_2O_3 thin films prepared by doctor-blading of iron nitrate and PMMA in a) water (FEWADB-550) and b) 2 M HCl (FEHCDB-550) and calcined at 550 ^oC, and a c) blank FTO substrate calcined at 550 ^oC, which were measured in darkness and under simulated sunlight in a 100 mL Perspex cell.

Since enhancement of adhesion of the hematite thin films on the FTO glass or a rise of temperature did not improve the photoresponse of hematite, doping hematite with different atoms is one of the approaches to increase the photoactivity [25, 75, 129-131, 138]. Here, Ti and Zn were doped into the hematite thin films so as to investigate the effect of dopants on the photocatalytic activity of hematite thin films. In the next two sections, Ti and Zn-doped Fe_2O_3 thin films are present including crystal structure, surface morphology, elemental analysis, UV-Vis absorbance and PEC properties.

3.2.2. Ti-doped Fe_2O_3 thin films

3.2.2.1. X-ray diffraction

Fig. 32 shows the X-ray diffraction patterns of Ti-doped iron oxide thin films on FTO glass substrates at a range of doping level from 2.5 to 20 at.% prepared by doctor-blading of $TiOCl_2$, $Fe(NO_3)_3.9H_2O$ and PMMA in 2 M HCl and calcined at 550 ^oC. Hematite was identified in diffraction patterns of the Ti-doped iron oxide thin films at a doping level from 2.5 to 20 at.% with the corresponding diffraction

peaks labeled by ‘H’. The cassiterite phase was also identified originating from the substrate. Other impurity phases, including anatase or rutile were absent at a level greater than the instrument sensitivity for the Ti-doped samples at a doping level from 2.5 to 10 at.%. However, anatase was present in 20 at.% Ti-doped samples with the corresponding peak labeled by ‘*’. Therefore, Ti seemed to be incorporated into hematite structure at a doping concentration between 2.5 and 10 at.%.

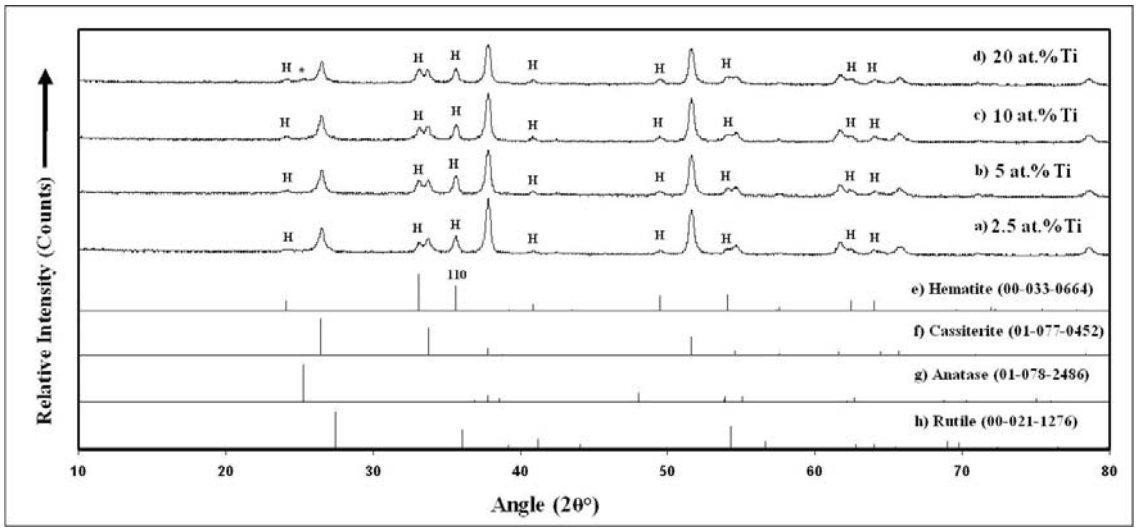

Figure 32. X-ray diffraction patterns of Ti-doped iron oxide thin films on FTO glass substrates prepared by doctor blading, a) 2.5 at.% (2.5TI-550-2-1L), b) 5 at.% (5TI-550-2-1L), c) 10 at.% (10TI-550-2-1L), d) 20 at.% Ti-doped iron oxide (20TI-550-2-1L), and reference patterns of e) hematite, f) cassiterite, g) anatase, and h) rutile.

The strong diffraction peak corresponding to the (110) plane was chosen to calculate the crystallite size of hematite for Ti-doped thin films. The results are described in Table 7. The crystallite sizes of Ti-doped Fe_2O_3 were in the range between 30 and 35 nm.

Sample Name	Crystallite Size (nm)
2.5TI-550-2-1L	30
5TI-550-2-1L	35
10TI-550-2-1L	35
20TI-550-2-1L	30

Table 7. Crystallite sizes of Ti-doped Fe_2O_3 thin films.

3.2.2.2. Optical absorption spectra

UV-Vis Absorbance spectra were obtained for two representative thin films, hematite and 5 at.% Ti-doped Fe_2O_3 thin films on FTO glass substrates (Fig. 33). For both thin films, there is a broad absorption between 600-800 nm, which can be explained by Crystal Field Theory [150] as the d-orditals of Fe^{3+} having been split into two sets where the d_{xy}, d_{xz} and d_{yz} orbitals are lower in energy and d_{z^2} and $d_{x^2-y^2}$ orbitals are higher. Here, the lower energy orbitals are completely filled with 5d-electrons, therefore when hematite absorbs photons within the visible region, electrons will be transferred from the lower energy d-orbitals to the higher energy excited state. Both films show similar absorbance at wavelength < 600 nm regardless of the Ti/Fe ratio.

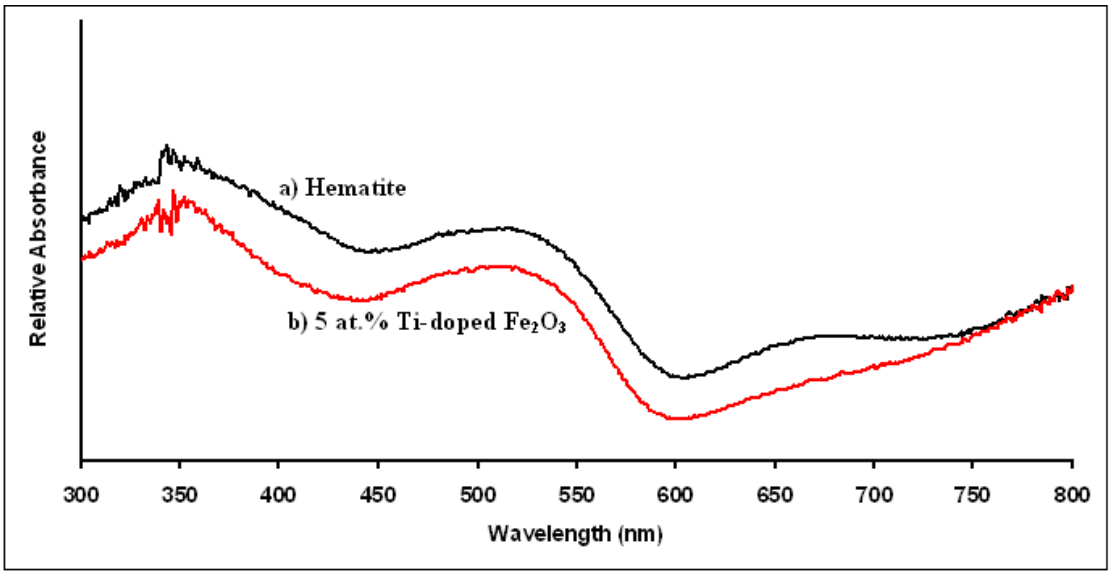

Figure 33. UV-Vis absorbance spectra of two representative thin films on FTO glass substrate, a) hematite (FEHCDB-550), and b) 5 at.% Ti-doped Fe_2O_3 thin films (5TI-550-2-1L).

Fig. 34 shows the differential absorbance ($d_{log(1/R)}/d_\lambda$) spectra of Ti-doped Fe_2O_3 thin films with different Ti content. The position of the minima corresponds to the absorption edge. There is only one absorption edge for each of the thin films. The electronic band gaps of these thin films were shown in nanometers and electron volts in Table 8 below. The electronic band gap of hematite and Ti-doped Fe_2O_3 thin films

is around 2.2 eV, which agrees well with the band-gap value of hematite. Therefore, the Ti dopant did not significantly change the band gap of hematite thin films.

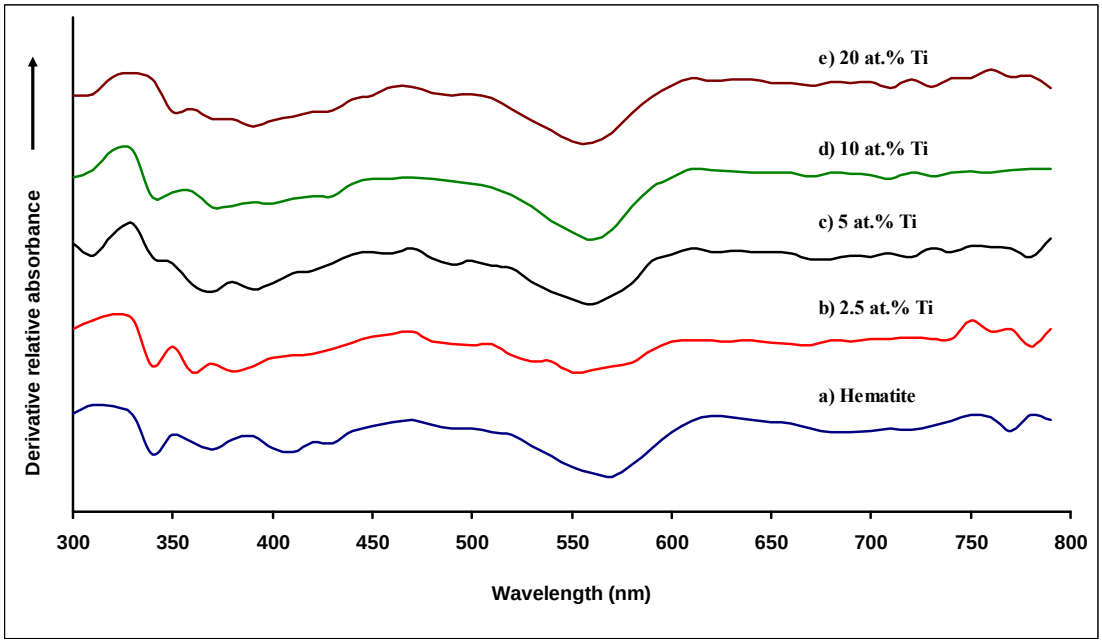

Figure 34. Differential absorbance spectra of , a) hematite (FEHCDB-550), b) 2.5 at.% (2.5TI-550-2-1L), c) 5 at.% (5TI-550-2-1L), d) 10 at.% (10TI-550-2-1L), and e) 20 at.% Ti-doped Fe_2O_3 thin films (20TI-550-2-1L).

Sample Name	Band-gap value (nm)	Band-gap value (eV)
FEHCDB-550	570	2.18
2.5TI-550-2-1L	550	2.26
5TI-550-2-1L	560	2.22
10TI-550-2-1L	560	2.22
20TI-550-2-1L	560	2.22

Table 8. Electronic band gaps of Ti-doped Fe_2O_3 thin films with different Ti content.

3.2.2.3. Morphological characterisation

Fig. 35 shows the SEM images of Ti-doped Fe_2O_3 thin films with different Ti content on FTO glass substrates. Inverse opal structures were not clearly seen in

either of Ti-doped Fe_2O_3 thin films possibly due to the existence of HCl in the solution which has already been discussed in Section 3.2.1.2.

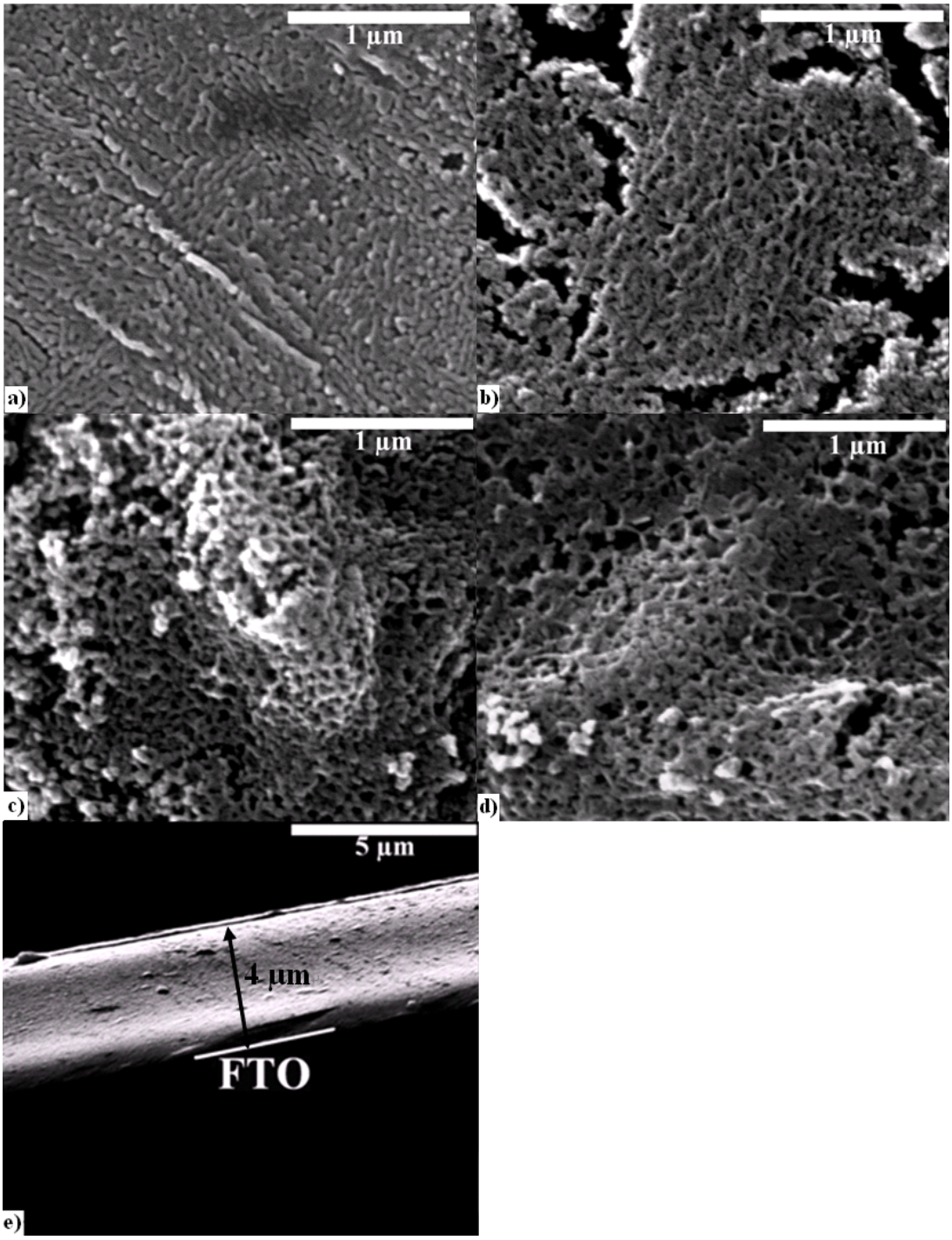

Figure 35. SEM images of a) 2.5 at.%, b) 5 at.%, c) 10 at.%, and d) 20 at.% Ti-doped Fe_2O_3 thin films on FTO glass substrates, and e) cross-section of 2.5 at.% Ti-doped Fe_2O_3 thin films on FTO glass substrate (thickness of the film: 4 µm).

3.2.2.4. EDX analysis

EDX analyses of Ti-doped Fe_2O_3 thin films at a range of doping levels between 2.5 and 20 at.% were reported in Table 9, respectively. The Ti doping levels of these Ti-doped Fe_2O_3 thin films (i.e., Ti/(Ti+Fe)) were about 2.49, 5.18, 10.08, 19.71 at.%, respectively, which is in agreement with the composition of the targets.

Elements / Sample Name	O (at.%)	Ti (at.%)	Fe (at.%)	Total (at.%)
2.5TI-550-2-1L	75.46	0.61	23.93	100.00
5TI-550-2-1L	64.10	1.86	34.04	100.00
10TI-550-2-1L	57.54	4.28	38.18	100.00
20TI-550-2-1L	51.61	9.54	38.85	100.00

Table 9. EDX analysis of Ti-doped Fe_2O_3 thin films at a doping content between 2.5 and 20 at.%.

3.2.2.5. Photoelectrochemical properties

Fig. 36 shows that 2.5 at.% Ti-doped Fe_2O_3 thin films (2.5TI-550-2-1L) obtained the highest photocurrent density, which was 0.47 $mA.cm^{-2}$ at 0.85 V (Fig. 36c). Undoped hematite thin films exhibited the lowest photocurrent density (Fig. 36a). When the Ti doping level is below 2.5 at.%, the photocurrent density increased with increasing of Ti content. A maximum photocurrent density of 0.16 $mA.cm^{-2}$ at 0.85 V was obtained in case of samples with 1 at.% Ti (Fig. 36b). When the Ti concentration is above 2.5 at.%, the photocurrent density of Ti-doped Fe_2O_3 thin films decreased with an increase of Ti dopant concentration. A maximum photocurrent density of 0.36 $mA.cm^{-2}$ at 0.85 V was recorded by 5 at.% Ti-doped Fe_2O_3 thin films (Fig. 36d) and 0.28 $mA.cm^{-2}$ by the ones with 10 at.% Ti at the same potential (Fig. 36e). 20 at.% Ti-doped Fe_2O_3 thin films recorded 0.23 $mA.cm^{-2}$ at 0.85 V (Fig. 36f). Therefore, the optimal Ti doping concentration appeared to be 2.5 at.% for hematite thin films.

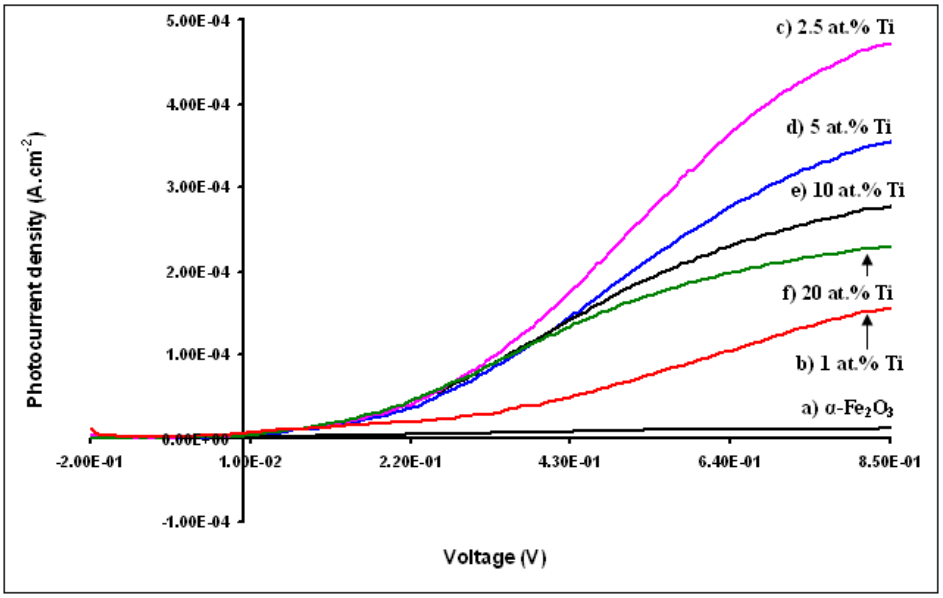

Figure 36. Photocurrent-voltage characteristics of Ti-doped Fe_2O_3 thin films at different dopant concentrations, a) α-Fe_2O_3 (FEHCDB-550), b) 1 at.% (1TI-550-2-1L), c) 2.5 at.% (2.5TI-550-2-1L), d) 5 at.% (5TI-550-2-1L), e) 10 at.% (10TI-550-2-1L), and f) 20 at.% Ti-doped Fe_2O_3 (20TI-550-2-1L) thin films in a 100 mL Perspex cell.

Fig. 37 shows that the maximum photocurrent density of 2.5 at.% Ti-doped Fe_2O_3 thin films calcined at 550 ^oC (0.47 $mA.cm^{-2}$ at 0.87 V) was much higher than that of the thin films calcined at 450 ^oC (0.06 $mA.cm^{-2}$ at 0.87 V). The enhanced photoresponse caused by the elevated calcination temperature is thought to be a result of better adhesion of the film and sintering of the hematite particles. However, the maximum photocurrent density of the films dropped from 0.47 $mA.cm^{-2}$ at 550 ^oC to 0.2 $mA.cm^{-2}$ at 600 ^oC (at 0.87 V). A rise of calcination temperature causes an increase of electric resistance of the FTO glass slides, therefore reducing the photocurrent [151]. Thus, the optimal calcination temperature of the 2.5 at.% Ti-doped Fe_2O_3 thin films is 550 ^oC.

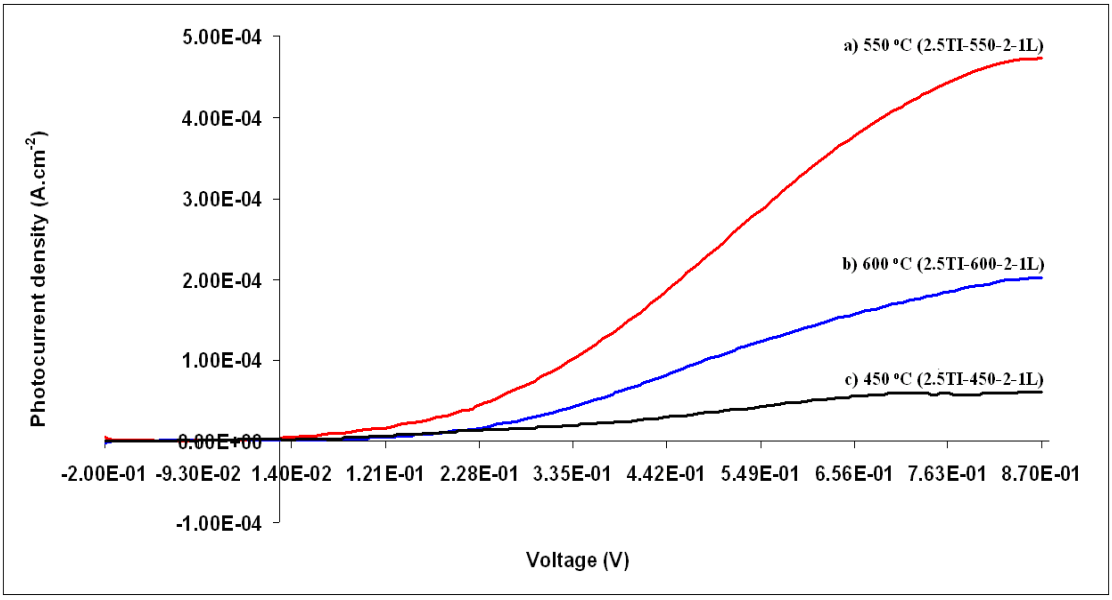

Figure 37. Photocurrent-voltage characteristics of 2.5 at.% Ti-doped Fe_2O_3 thin films calcined at three different temperatures, a) 550 °C (2.5TI-550-2-1L), b) 600 °C (2.5TI-600-2-1L), and c) 450 °C (2.5TI-450-2-1L) in a 100 mL Perspex cell.

Fig. 38a shows that 2.5 at.% Ti-doped Fe_2O_3 thin films (2.5TI-550-2-1L) with a thickness of 4 μm prepared from doctor blading of 0.0775 $g.mL^{-1}$ iron nitrate and 0.125 $g.mL^{-1}$ PMMA using one layer of adhesive tape (thickness: 20 μm [148]) (see Fig. 35e) recorded the highest photocurrent density (0.47 $mA.cm^{-2}$ at 0.83 V). Thinner films (2.5TI-550-4-1L) were obtained by reducing the concentrations of both iron nitrate and PMMA by half, i.e., 0.0388 $g.mL^{-1}$ and 0.0625 $g.mL^{-1}$, respectively, which was achieved by doubling the solvent. The maximum photocurrent density of these thinner films decreased to 0.096 $mA.cm^{-2}$ at 0.83 V (Fig. 38c), which was due to a lower absorption of light although the thin films were well adhered. Thicker films were acquired (2.5TI-550-1-1L) by doubling the concentrations of both iron nitrate and PMMA, i.e., 0.155 $g.mL^{-1}$ and 0.25 $g.mL^{-1}$, respectively, which was achieved by reducing the solvent by half. The maximum photocurrent density of these thicker films decreased to 0.19 $mA.cm^{-2}$ at 0.83 V (Fig. 38b) due to poor adhesion of the film (i.e, easily scraped off by a finger). This may have been due to the decrease in solvent present decreasing the drying time. Thicker films also prepared by doctor-blading of 0.0775 $g.mL^{-1}$ iron nitrate and 0.125 $g.mL^{-1}$ PMMA

using two layers of adhesive tape did not increase the photocurrent density (0.12 $mA.cm^{-2}$ at 0.83 V, Fig. 38d) which is thought to be due to the poor adhesion of the films. Therefore, the optimal thickness of the Ti-doped Fe_2O_3 thin films seemed to be 4 µm.

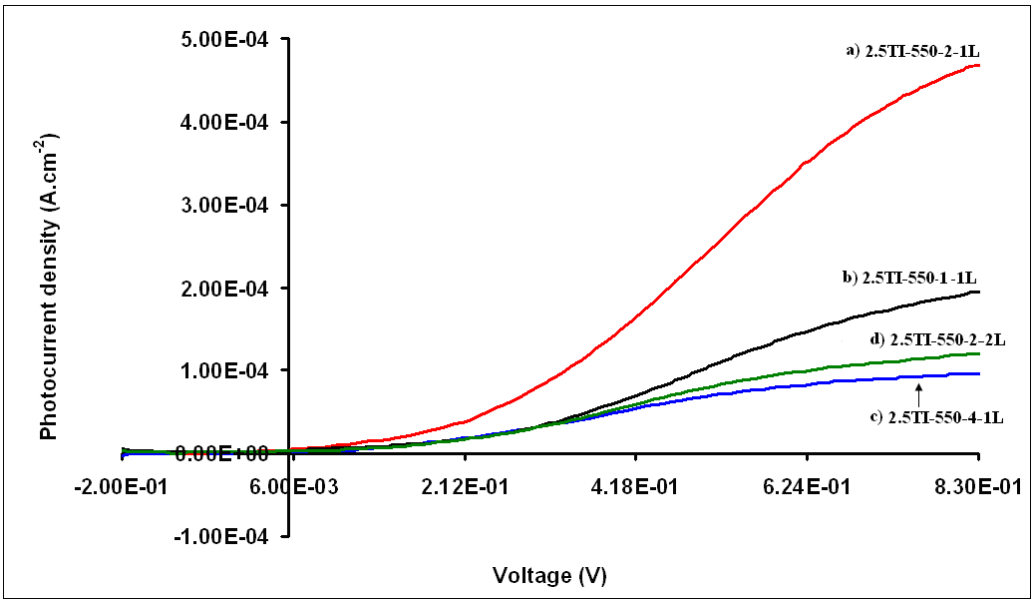

Figure 38. Photocurrent-voltage characteristics of 2.5 at.% Ti-doped Fe_2O_3 thin films with different thickness prepared by doctor-blading of a) 0.0775 $g.mL^{-1}$ iron nitrate and 0.125 $g.mL^{-1}$ PMMA with one layer of adhesive tape (2.5TI-550-2-1L), b) 0.155 $g.mL^{-1}$ iron nitrate and 0.25 $g.mL^{-1}$ PMMA with one layer of adhesive tape (2.5TI-550-1-1L), c) 0.0388 $g.mL^{-1}$ and 0.0625 $g.mL^{-1}$ with one layer of adhesive tape (2.5TI-550-4-1L), and d) 0.0775 $g.mL^{-1}$ iron nitrate and 0.125 $g.mL^{-1}$ PMMA with two layers of adhesive tape (2.5TI-550-2-2L) in a 100 mL Perspex cell.

Fig. 39 shows that the maximum photocurrent density of 2.5 at.% Ti-doped Fe_2O_3 thin films measured in a 100 mL Perspex cell (0.48 $mA.cm^{-2}$) was nearly four times as much as that of the films measured in a sandwich cell (0.11 $mA.cm^{-2}$) at an applied potential of 0.94 V. The reason for this large difference of photoresponse can be explained that the surface area of the Pt coated glass substrate used as the counter electrode in the sandwich cell is equal to the area of the o-ring (area: 1.74 cm^2) which is sandwiched in between the counter electrode and the photoanode. However, the surface area of the Pt foil used as the counter electrode in the 100 mL Perspex cell is 40.98 cm^2, which is much greater than that of the Pt-coated glass slide. Thus, the

photocurrent is limited by the surface area of cathode. Also, the volume of the electrolyte in the 100 mL Perspex cell is much larger than that in the sandwich cell. For the sandwich cell, H^+ and OH^- ions are localised on the surface of photoanode and cathode, respectively, due to a small volume of electrolyte in the sandwiched o-ring (the thickness of o-ring: 2.20 mm), which slows down the oxidation of OH^- ions by holes and reduction of H^+ ions by electrons on the photoanode and cathode surfaces, respectively, therefore resulting in charge carrier recombination. Thus, the water reduction rate is much higher in the 100 mL Perspex cell than that in the sandwich cell.

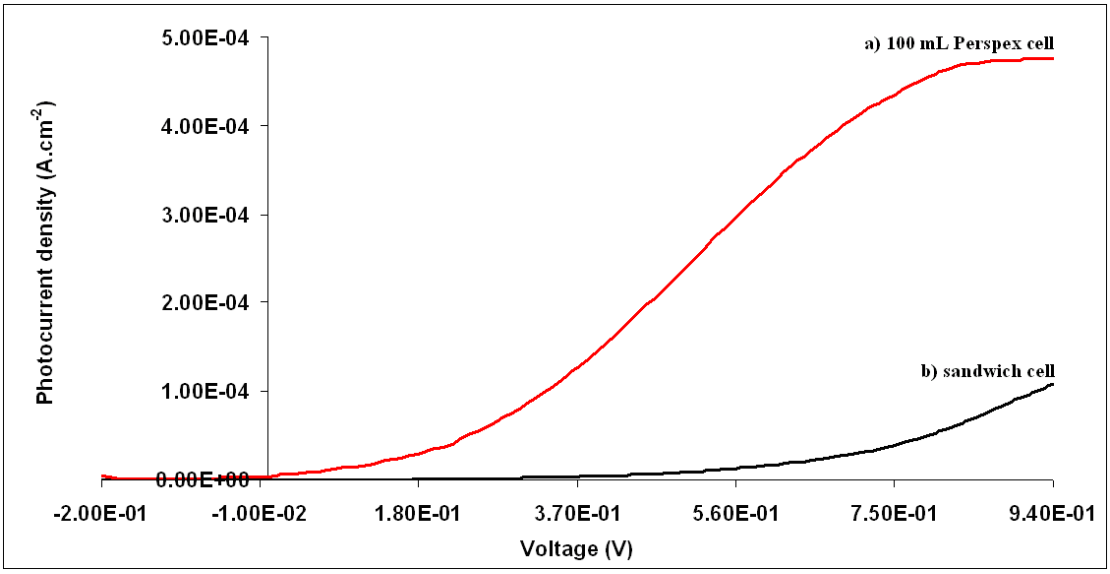

Figure 39. Ph-otocurrent-voltage characteristics of 2.5 at.% Ti-doped Fe_2O_3 thin films (2.5TI-550-2-1L), which were measured in a) a 100 mL Perspex cell and b) a sandwich cell.

IPCE values as functions of wavelength of Ti-doped Fe_2O_3 thin films at a range of doping levels between 2.5 and 20 at.% were shown in Fig. 40. The maximum IPCE of Ti-doped Fe_2O_3 thin films at a range of wavelength between 320 and 600 nm decreased with increase of Ti doping levels. Also, a positive IPCE value started at a higher wavelength with an increase of Ti doping levels, that is, 325 nm for 2.5 at.%, 335 nm for 5 and 10 at.%, and 345 nm for 20 at.%. A positive IPCE value finished at a shorter wavelength with an increase of Ti doping concentration. According to the literature, the bandgap wavelength of hematite is 564 nm [78].

However, the positive IPCE value of 20 at.% Ti-doped Fe_2O_3 thin films ended at 525 nm. In contrast, the positive IPCE values of 2.5, 5 and 10 at.% Ti-doped Fe_2O_3 thin films extended to 600, 590 and 580 nm, respectively. 2.5 at.% Ti-doped Fe_2O_3 thin films obtained the highest IPCE which was about 9.73% at 330 nm and 0.4 V. 20 at.% Ti-doped Fe_2O_3 thin films recorded the lowest IPCE which was about 2.10% at 375 nm and 0.4 V. Undoped hematite thin films acquired negative IPCE at the same range of wavelengths, which was not present in the graph.

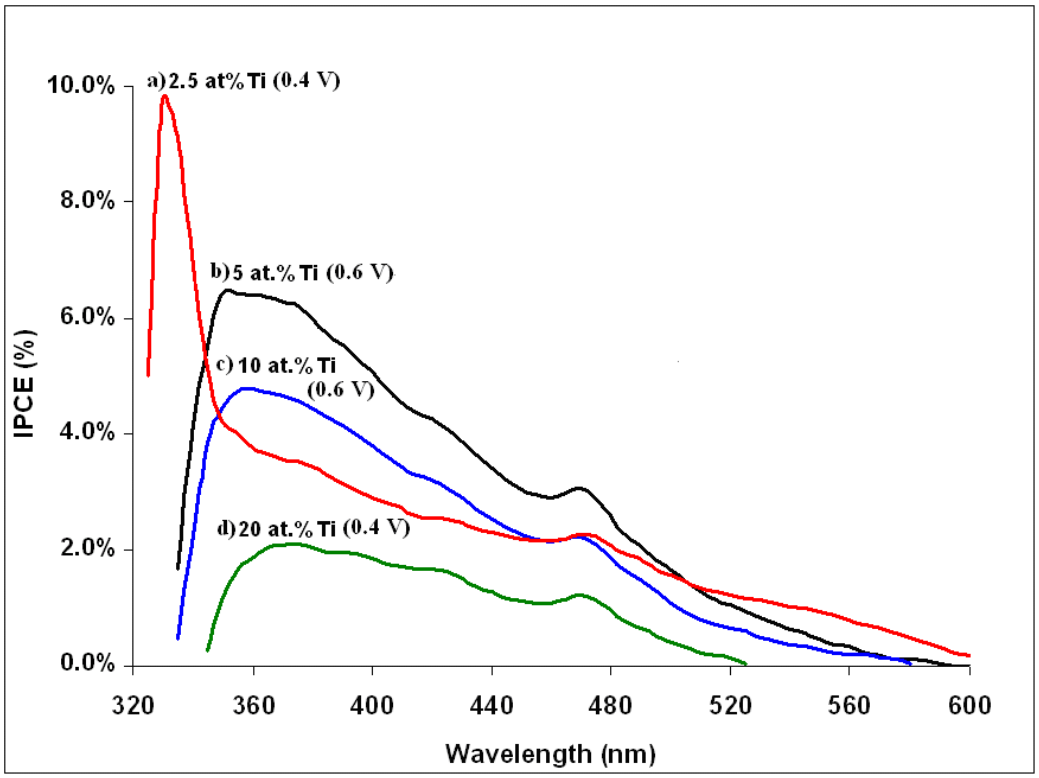

Figure 40. IPCE as a function of wavelength of the Ti-doped Fe_2O_3 thin films, a) 2.5 at.% Ti at 0.4 V, b) 5 at.% Ti at 0.6 V, c) 10 at.% Ti at 0.6 V, and d) 20 at.% Ti at 0.4 V.

Ti doping enhanced significantly the photoresponse of hematite thin films in water splitting. The optimum condition is the hematite thin films with 2.5 at.% Ti and 4 μm in thickness calcined at 550 ^{o}C. The enhanced performance is probably due to improved electrical conductivity of the films and the stabilisation of oxygen vacancies by Ti^{4+} ions. High purity hematite has a very low conductivity (< 10^{-4} Ω^{-1} m^{-1}), which causes a substantial potential drop during the transfer of photogenerated electrons through the bulk of the hematite electrode with high resistance. The

increase of electrical conductivity is attributable to the formation of Fe^{2+}-Fe^{3+} mixed-valence state. In this doping, Ti acts as an electron donor. The substitution of Fe^{3+} by Ti^{4+} on the Fe^{3+} lattice point causes the formation of Fe^{2+} on another lattice point so as to maintain the charge balance in the lattice. The Fe^{2+} ion has an excess d-electron, which acts as an electron carrier. The electron on the Fe^{2+} ion hops to the neighbouring Fe^{3+} site. This would enhance the electron transfer and thus the conductivity while decreasing the carrier recombination [135, 152]. Also, the increased donor concentration would increase the electric field across space charge layer causing a higher charge separation efficiency [79]. The photoresponse of Ti-doped hematite thin films decreased with an increase of Ti content (above 2.5 at.%). The reason is probably that decreasing the width of space charge layer which caused by increasing the donor concentration would negate the increased separation efficiency [79]. In combination of the results of XRD and PEC measurements, Ti seemed to enter into the hematite structure at a doping concentration between 2.5 and 20 at.%. However, anatase was present in 20 at.% Ti-doped samples. 2.5 at.% seemed to be an optimal doping concentration as the highest photoresponse was observed.

2.5 at.% Ti-doped Fe_2O_3 thin films acquired the highest photocurrent density which was 0.48 $mA.cm^{-2}$ at 0.94 V. Also, the largest overall photoconversion efficiency was 0.22% at 0.69 V using Eq. 1.9a. The largest IPCE was 9.73% at a wavelength of 330 nm and 0.4 V.

3.2.3. Zn-doped Fe_2O_3 thin films

3.2.3.1. X-ray diffraction

When deionised water was used as solvent in the preparation of Zn-doped Fe_2O_3 thin films, a very poor adhesion was obtained for all thin films, especially, those with 10 and 20 at.% Zn. When 2 M HCl was used as solvent instead of deionised water, the adhesion was enhanced significantly. The reason for the enhancement of adhesion has been explained in Section 3.2.1.2.

Fig. 41 shows the XRD patterns of Zn-doped iron oxide thin films with different Zn content on FTO glass substrates. Cassiterite was evident in these diffraction peaks of all the Zn-doped iron oxide thin films, which was from the FTO substrates. Hematite was identified in the diffraction patterns of 5 and 10 at.% Zn-doped Fe_2O_3 thin films (Fig. 41a and b) with the corresponding diffraction peaks labeled by 'H'. Zinc iron oxide ($ZnFe_2O_4$) was present in the 20 at.% Zn-doped Fe_2O_3 thin films (Fig. 41c) with the corresponding diffraction peaks labeled by '*'. Also, hematite seemed to be present in a small amount. No zincite (ZnO) was detected by the instrument.

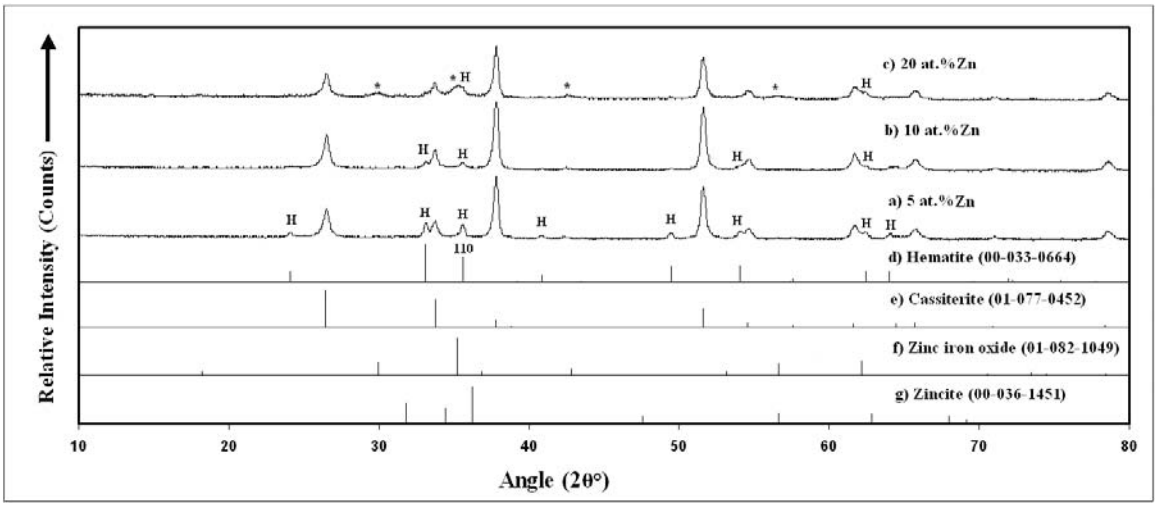

Figure 41. X-ray diffraction patterns of Zn-doped iron oxide thin films prepared by doctor blading, a) 5 at.% (ZNHCDB-5), b) 10 at.% (ZNHCDB-10), and c) 20 at.% Zn-doped iron oxide (ZNHCDB-20), and reference patterns of d) hematite, e) cassiterite, f) zinc iron oxide ($ZnFe_2O_4$), and g) Zincite (ZnO).

Therefore, Zn seemed to be incorporated into the hematite structure at a doping level between 5 and 10 at.%. However, when the content increased to 20 at.%, hematite almost disappeared, and zinc iron oxide was formed. Also, amorphous phase was probably present due to the absence of most of hematite.

The strong diffraction peak corresponding to the (110) plane was chosen to calculate the crystallite sizes of hematite for 5 and 10 at.% Zn-doped Fe_2O_3 thin films. The results are shown in Table 10. The crystallite sizes of hematite for 5 and 10 at.% Zn-doped Fe_2O_3 thin films were 44 and 47 nm, respectively.

Sample Name	Crystallite Size (nm)
ZNHCDB-5	44
ZNHCDB-10	47

Table 10. Crystallite sizes of Zn-doped Fe_2O_3 thin films

3.2.3.2. Optical absorption spectra

UV-Vis Absorbance spectra were acquired for two representative thin films, hematite and 10 at.% Zn-doped Fe_2O_3 thin films on FTO glass substrates (Fig. 42). As noted above, both films showed a broad and small absorption at 600-800 nm which is due to the absorption of photons resulting in the excitement of the 5d-electrons of Fe^{3+} from the lower energy d-orbitals to higher energy. Also, both films exhibited similar absorbance at wavelengths < 600 nm.

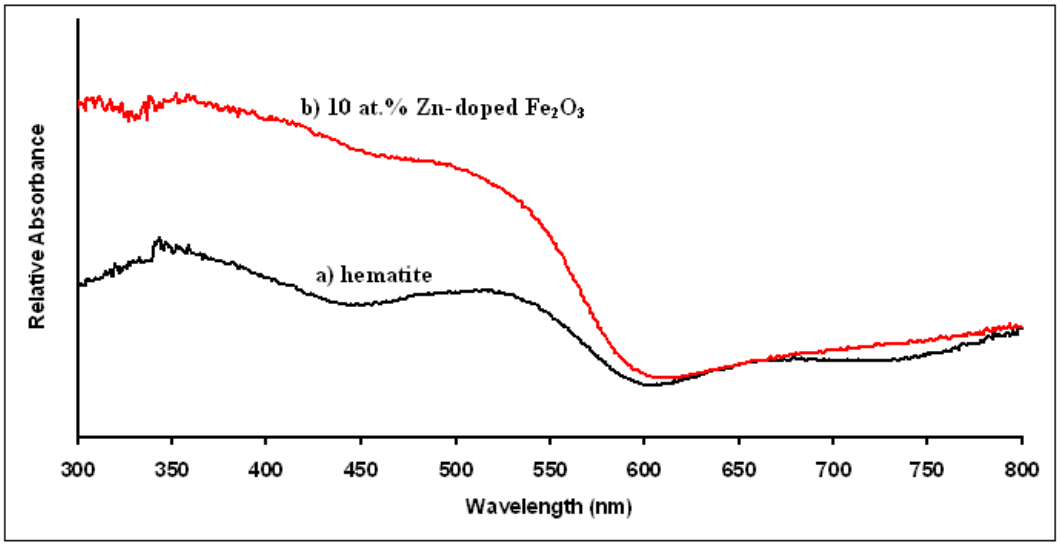

Figure 42. UV-Vis absorbance spectra of two representative thin films on FTO glass substrates, a) hematite (FEHCDB-550), and b) 10 at.% Zn-doped Fe_2O_3 thin films (ZNHCDB-10).

In order to estimate the energy position of absorption edges of the Zn-doped Fe_2O_3 thin films with different Zn content, the differential absorbance ($d_{(\log(1/R)}/d_\lambda$) spectra are shown in Fig. 43. According to the position of minima, 5 and 10 at.% Zn-doped Fe_2O_3 thin films had the same sharp absorption edge, 560 nm, corresponding to 2.22 eV, which is the value formerly reported for hematite phase [138]. There seemed to be no sharp absorption edges for 20 at.% Zn-doped Fe_2O_3

thin films. The absence of definite band gaps is probably due to the presence of amorphous or zinc iron oxide phase in the films.

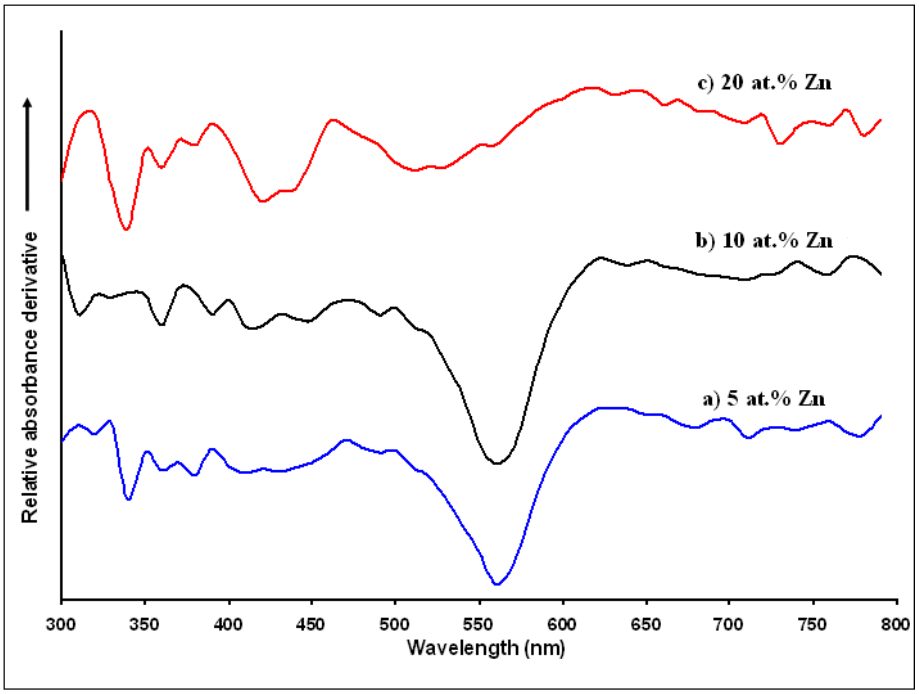

Figure 43. Differential absorbance spectra of, a) 5 at.% (ZNHCDB-5), b) 10 at.% (ZNHCDB-10), and c) 20 at.% Zn-doped Fe_2O_3 thin films (ZNHCDB-20).

3.2.3.3. Morphological characterisation

Fig. 44 shows the SEM images of the surface of Zn-doped Fe_2O_3 thin films with different Zn content. No inverse opal structure was formed in either of the Zn-doped Fe_2O_3 thin films. The reason for the destruction of inverse opal structure has been explained in Section 3.2.1.2. The voids between the grains appeared to be increased by the addition of PMMA though the inverse opal structure was not present.

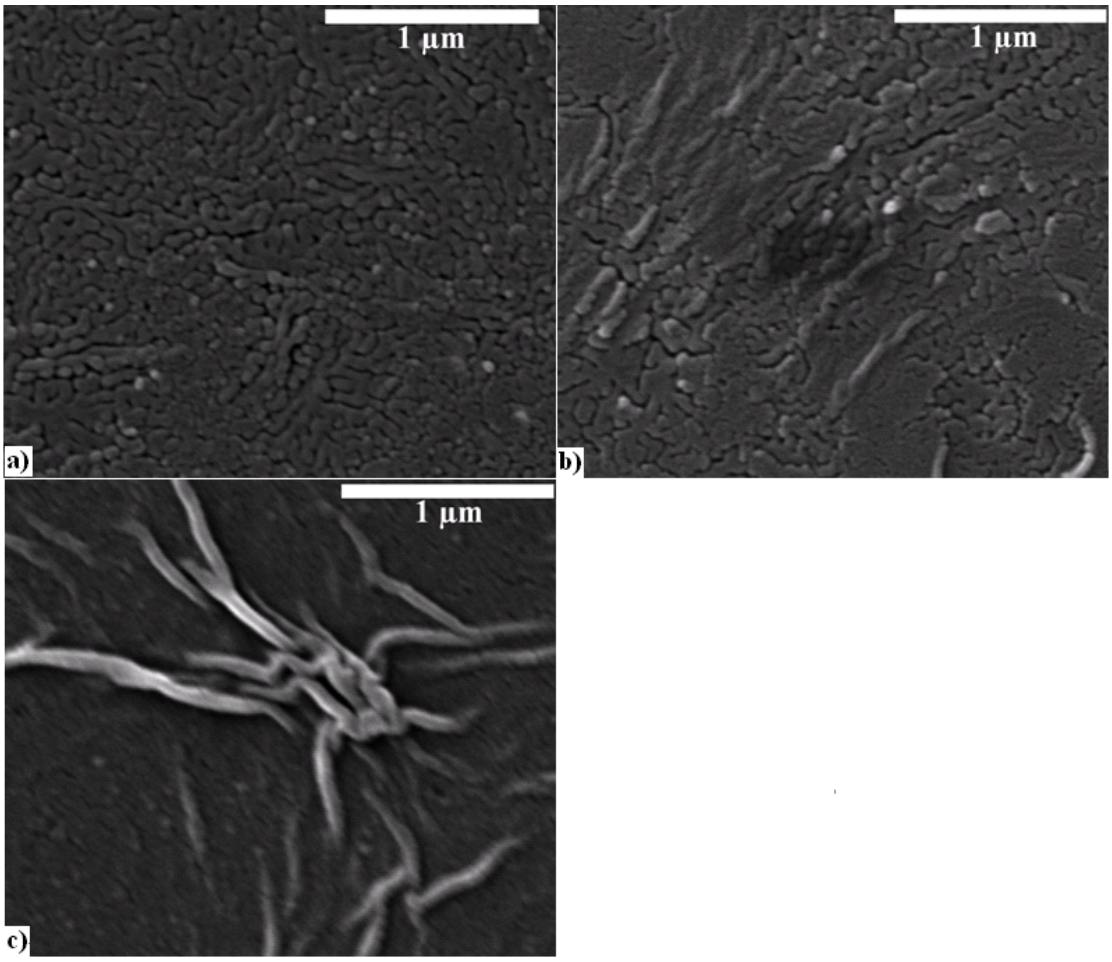

Figure 44. SEM images of a) 5 at.% (ZNHCDB-5), b) 10 at.% (ZNHCDB-10), and c) 20 at.% Zn-doped Fe_2O_3 thin films (ZNHCDB-20) on FTO glass substrates.

3.2.3.4. EDX analysis

EDX analyses of Zn-doped Fe_2O_3 thin films at a range of doping levels between 5 and 20 at.% were shown in Table 11, respectively. The Zn doping levels of these Zn-doped Fe_2O_3 thin films (i.e., Zn/(Zn+Fe)) were 5.03, 10.14 and 20.24 at.%, respectively, which is in agreement with the composition of the targets.

Elements / Sample Name	O (at.%)	Zn (at.%)	Fe (at.%)	Total (at.%)
ZNHCDB-5	58.04	2.11	39.85	100.00
ZNHCDB-10	58.97	4.16	36.87	100.00
ZNHCDB-20	66.89	6.70	26.41	100.00

Table 11. EDX analysis of Zn-doped Fe_2O_3 thin films at a doping content between 5 and 20 at.%.

3.2.3.5. Photoelectrochemical properties

Fig. 45 shows that Zn-doped Fe_2O_3 thin films with a range of doping levels from 5 to 20 at.% were almost photoelectrochemically inactive at a range of applied potentials between -1.2 and 0.2 V. Since Zn-doped Fe_2O_3 is a p-type semiconductor, cathodic bias voltages were applied to assist the water reduction at the photocathode. Therefore, introduction of Zn into hematite thin films did not enhance the electrode performance.

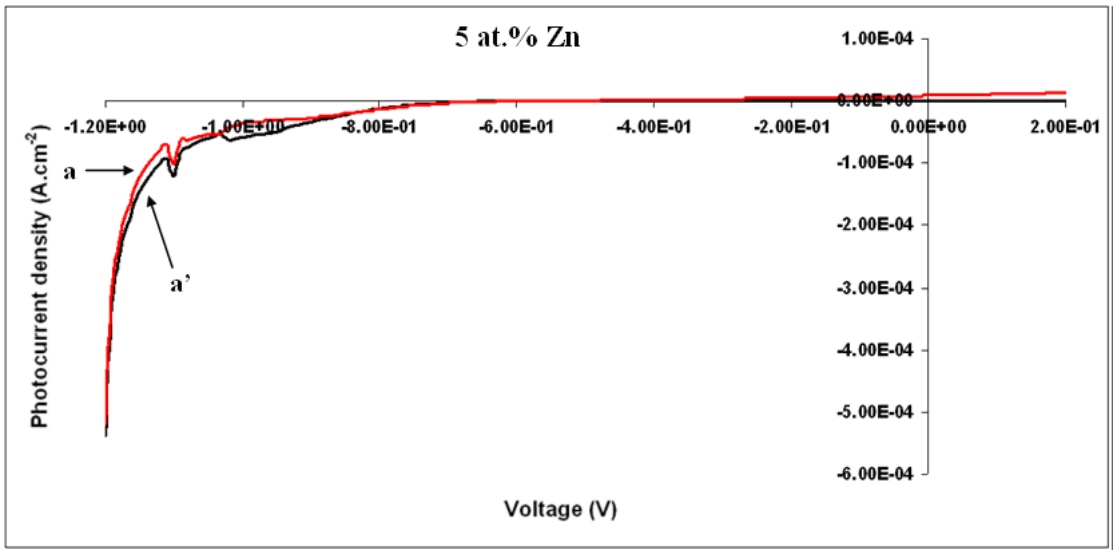

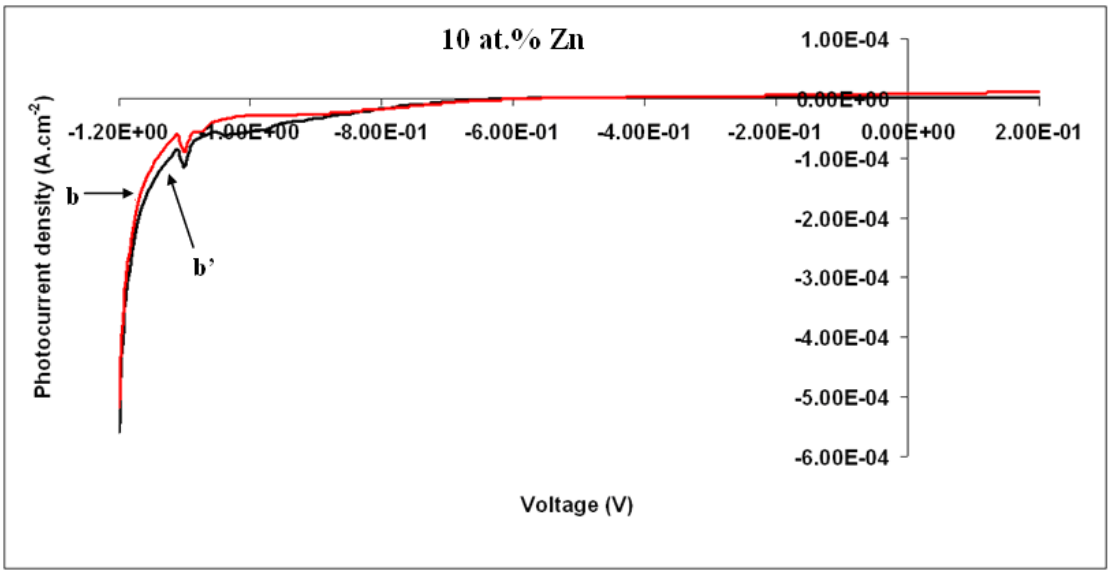

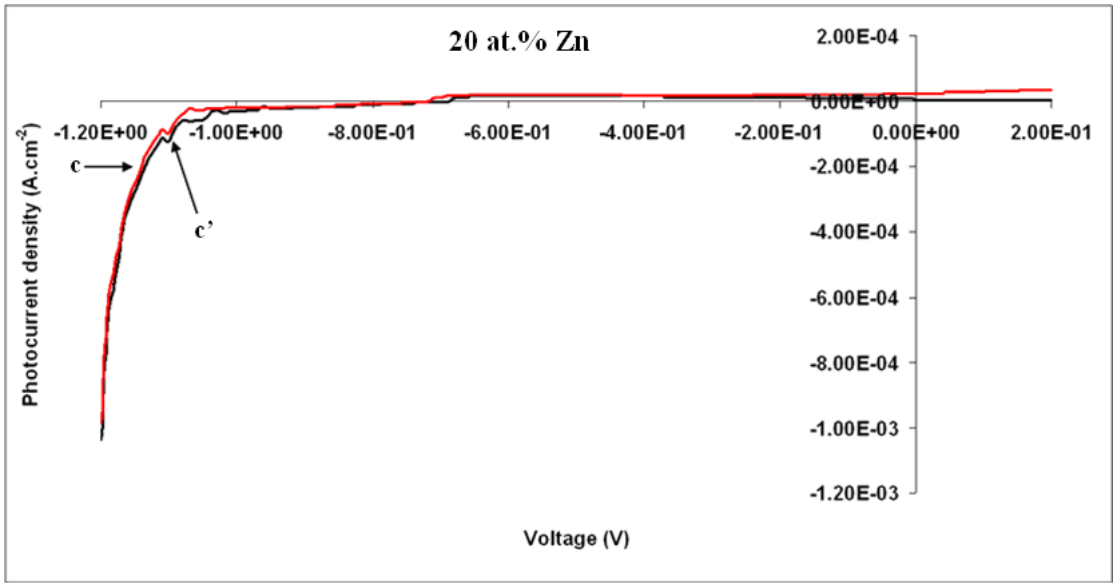

Figure 45. Photocurrent-voltage characteristics of 5-20 at.% Zn-doped Fe_2O_3 thin films prepared by doctor blading, which were measured in a 100 mL Perspex cell, a) 5 at.% Zn (ZNHCDB-5) under illumination, and a') in dark, b) 10 at.%Zn (ZNHCDB-10) under illumination, and b') in dark, and c) 20 at.% Zn (ZNHCDB-20) under illumination, and c') in dark.

The obtained poor performance of Zn-doped Fe_2O_3 thin films prepared by doctor blading contradicts the reasonable performance of Zn-doped Fe_2O_3 thin films prepared by spray pyrolysis by others [130, 131, 136]. A high photoresponse was observed by 4 at.% Zn-doped Fe_2O_3 thin films prepared by spray pyrolysis due to the existence of $ZnFe_2O_4$ in hematite, which exhibited enhanced conductive properties [131]. Enhancement of photocatalytic performace of spray pyrolytically synthesised 5 at.% Zn-doped Fe_2O_3 thin films was attributed to an increase in flatband potential and space charge region at the interface, which was induced by the Zn doping. The films were identified to be hematite and no $ZnFe_2O_4$ was present [130]. However, Zn-doping did not improve the photoresponse of α-Fe_2O_3 thin films prepared by doctor blading. Zn appeared to enter into the hematite structure at a doping concentration between 5 and 10 at.%. In this doping, Zn acts as an electron acceptor. The substitution of Fe^{3+} by Zn^{2+} forms a neighbouring Fe^{4+} ion which acts as a hole carrier to provide a hole to a neighbouring Fe^{3+} ion. Thus, the hole transport would be enhanced by Zn-doping. However, the conductivity of the *p*-type semiconductor

attributed to hole transfer by hopping through Fe^{III}/Fe^{IV} valence interchange between neighboring iron bilayers (see Fig. 8) is much lower than that caused by electron transfer by hopping through Fe^{II}/Fe^{III} valence interchange within the iron bilayers due to a larger activation barrier encountered by hole transport along [001] [6].Therefore, the enhancement of hole transfer did not overcome the slow hole mobility of hematite resulting in poor photoresponse. Also, at a doping level of 20 at.%, the presence of $ZnFe_2O_4$ and absence of most of hematite, caused by the incorporation of Zn resulted in poor performance.

3.3. Ti-doped Fe_2O_3 thin films by spray pyrolysis

3.3.1. X-ray diffraction

Fig. 46 shows that hematite was identified in the XRD pattern of 2.5 at.% Ti-doped Fe_2O_3 thin films prepared by spray pyrolysis (TIHCSP-6L). Cassiterite was also evident in the pattern, which was from the FTO layer on the glass. No anatase or rutile was detected. The crystallite size of these thin films was calculated using the diffraction peak corresponding to the crystal plane (110) and was found to be 58 nm, which is larger than that of 2.5 at.% Ti-doped Fe_2O_3 thin films prepared by doctor blading (Table 7).

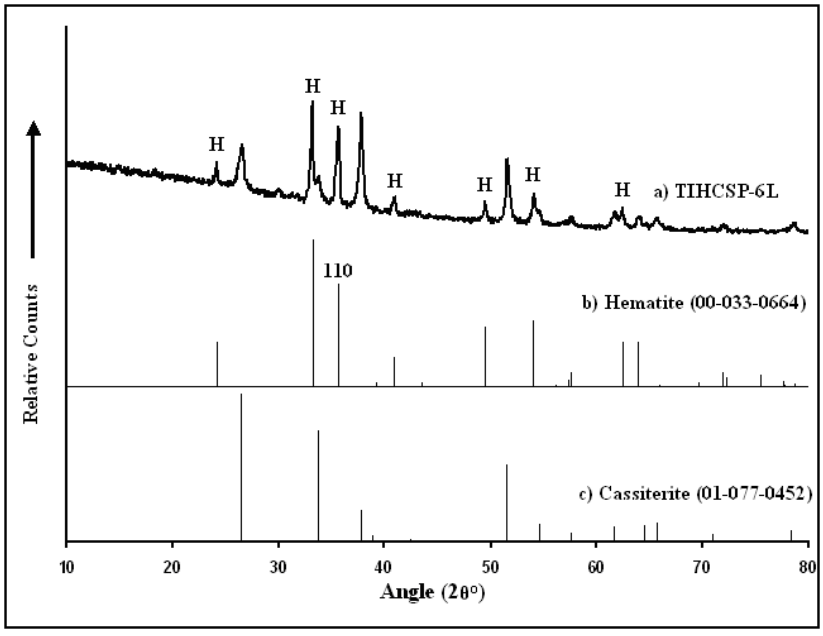

Figure 46. X-ray diffraction pattern of a) 2.5 at.% Ti-doped Fe_2O_3 thin films prepared by spray pyrolysis (TIHCSP-6L), and reference patterns of b) hematite and c) cassiterite.

3.3.2. Morphological characterisation

Fig. 47a shows the SEM image of the surface of 2.5 at.% Ti-doped Fe_2O_3 thin films prepared by spray pyrolysis. No voids were clearly found between the particles compared to the surface morphology of 2.5 at.% Ti-doped Fe_2O_3 thin films prepared by doctor blading using PMMA as template. Fig. 47b described the SEM image of the cross-section of this thin film. The thickness of the film was 1.5 µm.

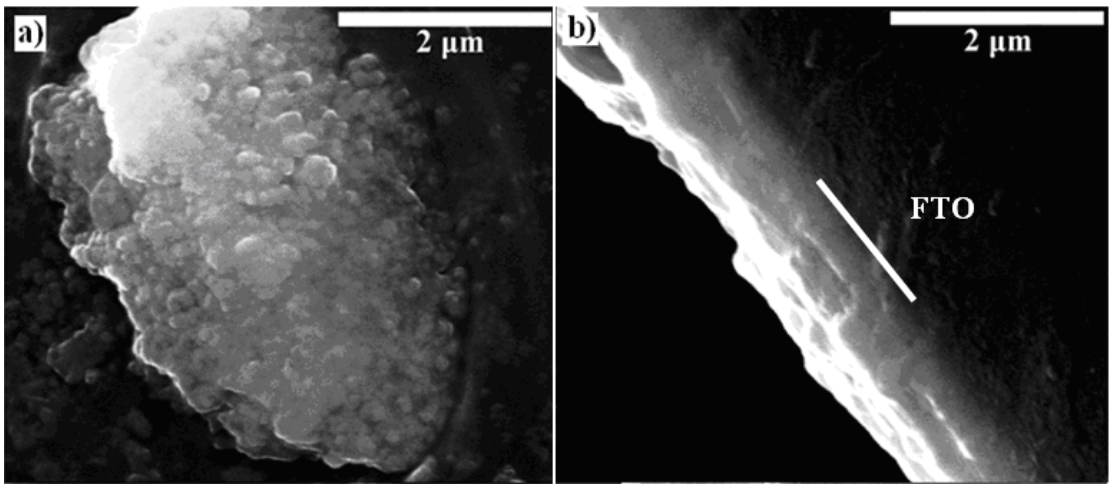

Figure 47. SEM images of 2.5 at.% Ti-doped Fe_2O_3 thin films prepared by spray pyrolysis, a) surface morphology, and b) cross-section.

3.3.3. EDX analysis

According to the results of EDX analysis (Table 12), impurity elements, Cu, Zn, Cl were introduced into the sample, which came from the metallic/brass components of the spray gun in an acidic solution (2 M HCl). Ti was also present in the sample, which was from the titanium dopant precursor, $TiOCl_2$. The Ti/(Ti+Fe) ratio is about 2 at.%.

Element	At.%
O	53.21
Fe	38.65
Cu	5.75
Cl	0.50
Ti	0.79
Zn	1.10

Table 12. EDX analysis of 2.5 at.% Ti-doped Fe_2O_3 thin films.

3.3.4. Photoelectrochemical properties

Fig. 48 shows the photocurrent density of 2.5 at.% Ti-doped Fe_2O_3 thin films (TIHCSP-6L) prepared by spray pyrolysis as a function of applied potentials bebtween -0.2 and 0.94 V. The maximum photocurrent density was 0.06 $mA.cm^{-2}$ at 0.94 V. The reason for the poor performance is probably the introduction of impurities from the metallic/brass components of the spray gun in an acidic medium such as Zn and Cu (see Table 12). The copper present in the thin films have three valences, 0, +1 and +2. As can be seen in Fig. 49, copper impurities react with the photogenerated electrons and holes through different valences, thus competing with water for the electrons. The reduction potential of Zn^{2+}/Zn is close to the water reduction potential (see Fig. 49). Hence, zinc might compete with water for the electrons.

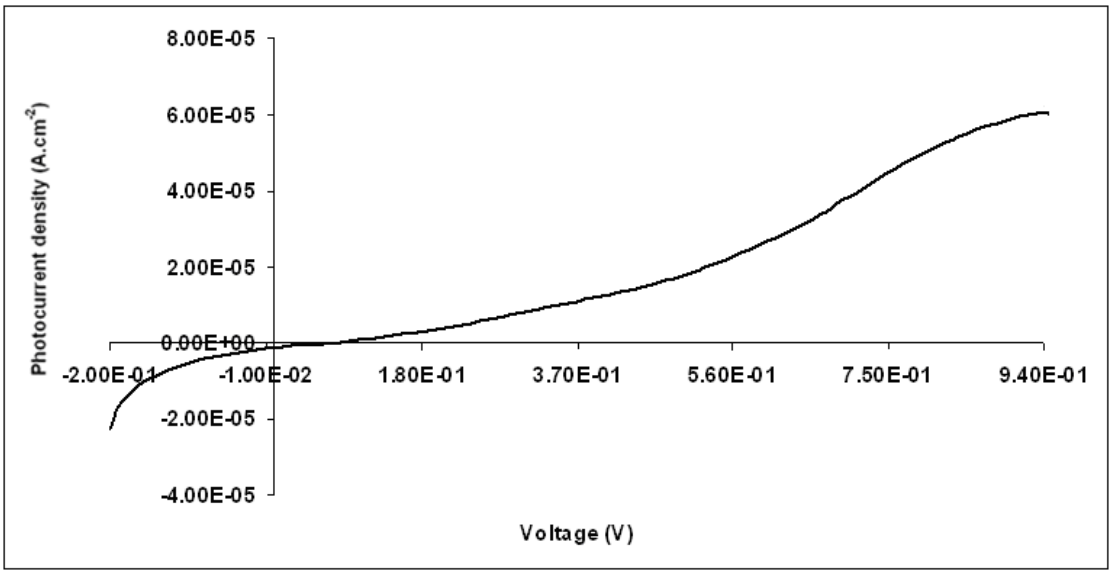

Figure 48. Photocurrent-voltage characteristics of 2.5 at.% Ti-doped Fe_2O_3 thin films (TIHCSP-6L) prepared by spray pyrolysis, which was measured in a 100 mL Perspex cell.

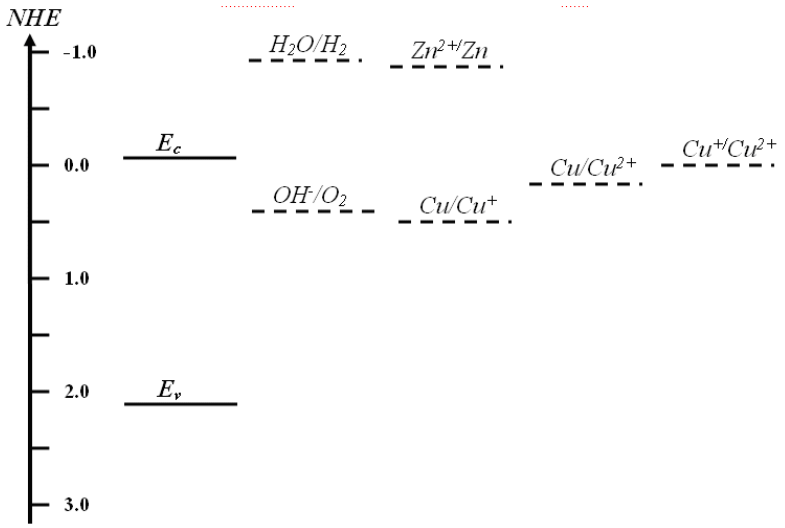

Figure 49. Band edge positions of hematite and reduction potentials of water, copper and zinc at pH 13 [3, 15].

A poor photoresponse was acquired by the 2.5 at.% Ti-doped Fe_2O_3 thin films prepared by spray pyrolysis due to the incorporation of impurities, e.g., Cu and Zn into the thin films. This does not agree with the high photoresponse of Ti-doped hematite thin films prepared by spray pyrolysis in the literature. It is reported by Sartoretti [138] that a photocurrent density of 4.05 $mA.cm^{-2}$ at 0.45 V vs NHE was observed for 5 at.% Ti-doped Fe_2O_3 thin films prepared by spray pyrolysis of 0.1 M

$FeCl_3.6H_2O$ and titanium ethoxide in absolute ethanol on FTO glass substrate at a temperature between 370 and 450 ^oC, compared to 0.78 $mA.cm^{-2}$ at the same applied potential in the undoped case. The enhanced performance is explained by the increased conductivity of the films and the stabilisation of oxygen vacancies by Ti doping. In contrast, the use of an acidic solution in this preparation instead of ethanol resulted in the introduction of impurities, decreasing markedly the photoactivity of the films.

4. Conclusions and future work

4.1. Conclusions

Undoped, Ti and Zn-doped Fe_2O_3 thin films were prepared by doctor blading and Ti-doped Fe_2O_3 thin films by spray pyrolysis. These thin films were characterised with the use of SEM, EDX, XRD, TGA, UV-Vis as well as PEC measurements.

Iron oxide thin films prepared by doctor blading of a mixture of iron nitrate and PMMA at a mass ratio of 0.636 in methanol, water and 2 M HCl aqueous solution on FTO glass substrate and calcination at 450 and 550 ^oC were identified to be hematite. Without the addition of PMMA, iron nitrate solution could not be evenly spread out on the FTO glass substrate by doctor blading since the solution was hydrophilic. Thus, PMMA has a great effect on the preparation of an even hematite film on the substrate. Moreover, inverse opals of hematite were formed with the aid of PMMA when methanol and water are used as solvent. The optimal range of mass ratios between iron nitrate and PMMA is between 0.477 and 0.636, which formed inverse opals of hematite with long range order. The formation of inverse opals of hematite can be explained that iron nitrate aqueous solution infiltrates into the voids of PMMA spheres which exhibit a 3-D, long-range ordering structure. Then hematite solid is formed by decomposition of iron nitrate, which is followed by the decomposition of PMMA. This order ensures the formation of inverse opals of hematite. However, hematite thin films prepared from iron nitrate in 2 M HCl

aqueous solution did not exhibit an inverse opal structure, which is probably due to the change of polarity of the iron nitrate aqueous solution.

Hematite thin films prepared by using water as solvent and calcination at 450 ^{o}C exhibited a better adhesion than the films with methanol as solvent, which is probably due to a much longer drying process resulting in the formation of a better contact between iron nitrate and the FTO glass surface. The adhesion of films on FTO glass substrate was enhanced by increasing the calcination temperature. Also, the adhesion was enhanced significantly when a 2 M HCl aqueous solution was used as solvent instead of water. The enhancement of adhesion may be related to the change of polarity and wetting properties of the iron nitrate aqueous solution in the presence of 2 M HCl.

Ti-doped iron oxide thin films at a range of doping levels between 2.5 and 20 at.% were prepared from doctor-blading of iron nitrate and PMMA in 2 M HCl with $TiOCl_2$ aqueous solution as dopant on FTO glass slides and calcined at 550 ^{o}C. All the films exhibited a very good adhesion. Hematite was evident in the films at all doping levels. Anatase seemed to be present in the 20 at.% Ti-doped Fe_2O_3 thin films. The electronic band gaps of undoped and Ti-doped hematite thin films were around 2.2 eV. Thus, Ti dopants did not appear to change the band-gap value of hematite thin films. Inverse opal structure was not present in all of the Ti-doped Fe_2O_3 thin films due to the existence of HCl in aqueous solution. The thickness of the 2.5 at.% Ti-doped Fe_2O_3 thin films is 4 μm. The EDX results of these thin films show that the Ti doping levels of the hematite thin films at a range of Ti concentrations from 2.5 to 20 at.% were 2.49, 5.18, 10.08, 19.71 at.%, respectively. Zn-doped iron oxide thin films at a range of Zn content between 5 and 20 at.% were prepared by doctor-blading of iron nitrate aqueous solution in 2 M HCl with $Zn(NO_3)_2.6H_2O$ as dopant on FTO glass slides. Hematite was present in the 5 and 10 at.% Zn-doped iron oxide thin films. As to 20 at.% Zn-doped iron oxide thin films, zinc iron oxide was identified and amorphous phase was probably present due to the absence of most of hematite. The electronic band gaps of 5 and 10 at.% Zn-doped Fe_2O_3 thin films were 2.22 eV. There were no definitive band gaps for 20 at.% Zn-doped Fe_2O_3 thin films,

which is probably due to the presence of amorphous or zinc iron oxide phase. Also, no inverse opals were formed according to the SEM images. The EDX results of these thin films show that the Zn doping levels of hematite thin films at a range of Zn concentrations between 5 and 20 at.% were 5.03, 10.14 and 20.24 at.%, respectively. Undoped hematite thin films were not photoactive due to poor electrical conductivity and rapid carrier recombination. However, incorporation of Ti improved the photoresponse of the hematite films probably due to the enhanced electrical conductivity of the films and the stabilisation of oxygen vacancies by the Ti^{4+} ions. It can be explained that Ti^{4+} ions substitute for Fe^{3+} ions in the hematite lattice with consequent formation of Fe^{2+} ions which act as electron carriers to provide electrons to neighbouring Fe^{3+} ions by hopping. Although Zn-doping seemed to enhance the hole transport by the formation of hole carriers, i.e, Fe^{4+} ions, it did not effectively enhance the photoresponse of hematite electrodes due to the slow hole mobility of hematite.

2.5 at.% Ti doping in α-Fe_2O_3 was the optimal concentration, which recorded a highest photocurrent density of 0.48 $mA.cm^{-2}$ at 0.94 V, a highest overall photoconversion efficiency of 0.22% at 0.69 V and a highest IPCE of 9.73% at 330 nm and 0.4 V. Compared to Ti-doped samples, Zn-doped ones at a doping level between 5 and 20 at.% did not show any photoresponse.

Some important factors that influence the photocatalytic performance of 2.5 at.% Ti-doped samples were investigated, including calcination temperature, thickness and adhesion of the films, and two different types of reactors. *i)* Although increasing calcination temperature enhanced adhesion of the films and sintering of the particles, resulting in a higher photocurrent, it increased the electrical resistivity of the FTO glass slides, which adversely influenced the photoresponse. An optimal calcination temperature of 550 ^{o}C was thought to balance these competing effects and yield the best PEC performance. *ii)* The thickness of the films was controlled by changing the concentrations of both iron nitrate and PMMA, or using a varying number of layers of adhesive tapes. It was found that the films with a thickness of 4 μm, which was prepared from 0.0775 $g.mL^{-1}$ iron nitrate and 0.125 $g.mL^{-1}$ PMMA with the use of

one layer of adhesive tape, obtained the highest photocurrent. With the use of one layer of adhesive tape, doubling and reducing the concentration by half decreased the photoresponse. The thicker films exhibited poor adhesion due to less solvent and thus the shorter drying time. The thinner films had less material on the substrate and therefore the less light absorption though the films were well adhered. Also, the thicker films were obtained by keeping the concentration unchanged and using two layers of adhesive tape, which decreased the performance of the films due to poor adhesion. *iii)* Two different types of photoelectrolysis cells were used for the examination of the photoresponse of 2.5 at.% Ti-doped Fe_2O_3 thin films. The maximum photocurrent density of the films obtained in the 100 mL Perspex cell was four times that of the films in the sandwich cell. There might be two reasons that cause the difference of the photoresponse. One is that the surface area of the counter electrode in the 100 mL Perspex cell is much larger than that in the sandwich cell. As water is reduced on the surface of counter electrode, a higher surface area contributes to a higher rate of water reduction. Thus, the photocurrent is controlled by the surface area of the counter electrode. The other is that the volume of the electrolyte in the 100 mL Perspex cell is much greater than that in the sandwich cell. A small volume of electrolyte in the sandwich cell cause the localisation of H^+ and OH^- at the photoelectrode and the counter electrode, respectively, which hinders the water splitting.

2.5 at.% Ti-doped Fe_2O_3 thin films were prepared by spray pyrolysis. Hematite was identified in the films and no other crystal phases were found in the films. No voids were clearly seen on the surface morphology of the films. A maximum photocurrent density of 0.06 $mA.cm^{-2}$ at 0.94 V was observed by the films. The poor photoresponse appeared to be a result of the introduction of impurities, Zn and Cu in the films from the metallic/brass components of the spray gun in an acidic solution.

4.2. Future work

Raman and X-ray photoelectron spectroscopy (XPS) [79] will be utilised to identify all the phases in the undoped and doped hematite thin films prepared by

doctor blading and spray pyrolysis. For the Ti-doped Fe_2O_3 thin films prepared by doctor blading, the results in combination with XRD observations can be employed to confirm whether Ti is introduced into the lattice of hematite and find out the reason for the decrease of photoresponse with an increase of Ti concentration above 2.5 at.%. For the Ti-doped Fe_2O_3 electrodes prepared by spray pyrolysis, the phases related to impurities, e.g., Zn and Cu can be used to figure out the reasons for the poor photocatalytic activity of the films. Also, the reasons for the poor performance of Zn-doped Fe_2O_3 thin films prepared by doctor blading will be found out with the aid of the spectra. Furthermore, as enhanced electrical conductivity due to Ti doping seemed to contribute to the improvement of photoelectrochemical activity of the hematite thin films prepared by doctor blading, the effect of dopants on the electrical properties of the films will be investigated through electrical conductivity measurements and electrochemical impedance spectroscopy [135].

Alternative dopants can be incorporated into hematite thin films, e.g., Si in attempt to improve the hematite electrode performance. Si has a tetravalence, which is the same as Ti. Si-doped hematite electrodes have been examined by many researchers in the field of water splitting. High photoelectrochemical performance has been observed by the Si-doped Fe_2O_3 thin films [13, 76, 124, 125, 135] which were synthesised by a couple of techniques, e.g., atmospheric pressure chemical vapour deposition (APCVD), spray pyrolysis, reactive DC magnetron sputtering, spin coating. However, there have been no reports on application of hematite thin films doped with Si prepared by doctor blading to water splitting. Therefore, Si-doped hematite thin films will be prepared by doctor blading. Also, the photocatalytic activity of the films will be investigated.

As the undoped and doped hematite thin films which exhibited well adhesion did not present an inverse opal structure, all the properties caused by the inverse opal structure, e.g., a high surface area, could not be investigated. As the dopant precursor for Ti doping, $TiOCl_2$ only exists in an acidic medium which destroys the inverse opal structure. In order to prepare Ti doped samples with well adhesion and an inverse opal structure, an alternative Ti precursor which exists in a neutral medium

and an alternative preparation technique which gives the films well adhesion need to be used to replace $TiOCl_2$ and doctor blading, respectively. Some Ti doping precursors, e.g., TPT (tetraisopropyl titanate) and titanium (IV) ethoxide can be incorporated into hematite photoelectrodes. Dip coating has been one of the preparation techniques to fabricate hematite thin-film electrodes [126, 153]. Ti-doped Fe_2O_3 thin films deposited on FTO glass substrate with and without an inverse opal structure will be prepared by dip coating. The photoelectrochemical activity of the photoelectrodes with an inverse opal structure will be examined through photosplitting of water. Also, the photoactivity of the samples without an inverse opal structure will be investigated for comparison.

5. References

1. Liu, S., S. Kokot, and G. Will, *Photochemistry and chemometrics - An overview.* J. Photochem. Photobiol. C: Photochem. Rev., 2009. **10**: p. 159-172.
2. Kittel, C., *Introduction to solid state physics*. Seventh ed. 1996, New York: John Wiley & Sons, Inc. 673.
3. Grimes, C.A., O.K. Varghese, and S. Ranjan, *Light, water, hydrogen - The solar generation of hydrogen by water photoelectrolysis*. 2008, New York: Springer Science + Business Media, LLC. 546.
4. Nozik, A.J. and R. Memming, *Physical chemistry of semiconductor-liquid interfaces.* J. Phys. Chem., 1996. **100**: p. 13061-13078.
5. Nozik, A.J., *Photoelectrochemistry: Applications to solar energy conversion.* Ann. Rev. Phys. Chern., 1978. **29**: p. 189-222.
6. Iordanova, N., M. Dupuis, and K.M. Rosso, *Charge transport in metal oxides: A theoretical studty ofhematite a-Fe2O3.* J. Chem. Phys., 2005. **122**(144305): p. 1-10.
7. Majumder, S.A. and S.U.M. Khan, *Photoelectrolysis of water at bare and electrocatalyst covered thin film iron oxide electrode.* Int. J. Hydrogen Energy, 1994. **19**(11): p. 881-887.
8. Glasscock, J.A., et al., *Photoelectrochemcial hydrogen production using nanostructured a-Fe2O3 electrodes.* Proc. of SPIE, 2006. **6340**(63400N): p. 1-12.
9. Qian, X.M., et al., *Photoelectrochemical characteristics of Fe2O3 nanocrystalline semiconductor thin film.* J. Nanopart. Res., 2000. **2**: p. 191-198.

10. Prakasam, H.E., et al., *Synthesis and photoelectrochemical properties of nanoporous iron (III) oxide by potentiostatic anodization.* Nanotechnology, 2006. **17**: p. 4285-4291.
11. Brezensinski, T., et al., *Crystal-to-crystal phase transition in self-assembled mesoporous iron oxide films.* Angew. Chem.-Int. Edit., 2006. **45**: p. 781-784.
12. Beermann, N., L. Vayssieres, and S.E. Lindquist, *Photoelectrochemical studies of oriented nanorod thin films of hematite.* J. Electrochem. Soc., 2000. **147**(7): p. 2456-2461.
13. Cesar, I., et al., *Translucent thin film Fe2O3 photoanodes for efficient water splitting by sunlight: Nanostructure-directing effect of Si-doping.* J. Am. Chem. Soc., 2006. **128**: p. 4582-4583.
14. William, D. and J. Callister, *Materials science and engineering : an introduction*. 6th ed. 2003, New York: John Wiley & Sons. 820.
15. Bagotsky, V.S., *Fundamentals of electrochemistry*. Second ed. 2006, Hoboken: John Wiley & Sons, Inc. 722.
16. Jain, I.P., *Hydrogen the fuel for 21st century.* Int. J. Hydrogen Energy, 2009. **34**: p. 7368-7378.
17. IEA, *Key world energy statistics*. 2008, Paris: Stedi Media. 78.
18. ElBaradei, M., *Tackling the global energy crisis.* IAEA Bull., 2008. **50-1**: p. 1-2.
19. Minculete, G. and M.M. Popescu, *End of the petroleum supply. Possible consequences.* Strategic Impact, 2008(4): p. 28-35.
20. Strahan, D., *Reserves of the black stuff were supposed to last for centuries. But rock bottom could come a lot sooner than that.* New Sci., 2008: p. 38-41.
21. Liu, P.I., *Energy, technology, and the environment*. 2005, New York: ASME press. 1-273.
22. MNRE Indian Metrological Department, S.E.C. *Solar Radiation Hand Book (2008)*. 2008 [cited 23/09/09]; Available from: http://mnes.nic.in/sec/srd-sec.pdf.
23. Metu, H., *Physical chemistry - Quantum mechanics*. 2006, New York: Taylor & Francis Group, LLC. 481.
24. Serpone, N. and E. Pelizzetti, *Photocatalysis: Fundamentals and Applications*. 1989, John Wiley & Sons, Inc.: New York.
25. Glasscock, J.A., *Nanostructured materials for photoelectrochemical hydrogen production using sunlight*, in *School of Chemical Sciences and Engineeing*. 2007, University of New South Wales. p. 220.
26. Oldham, K.B. and J.C. Myland, *Fundmentals of electrochemical science*. 1994, San Diego: Academic Press, INC. 474.
27. Divisek, J., ed. *Water electrolysis in a low and medium temperature regime*. Electrochemcial hydrogen technologies - Electrochemcial production and combustion of hydrogen, ed. H. Wendt. 1990, Elsevier: New York. 137-212.
28. Micic, O.I., ed. *Nanostructured and photoelectrochemical systems for solar photon conversion*. Photoconversion of solar energy, ed. M.D. Archer and A.J. Nozik. Vol. 3. 2006, Imperial College Press: Cambridge. 760.

29. Bak, T., et al., *Photo-electrochemical properties of the TiO2-Pt system in aqueous solutions.* Int. J. Hydrogen Energy, 2002. **27**: p. 19-26.
30. Memming, R., *Comprehensive treatise of electrochemistry*. Vol. 7. 1983, New York: Plenum Press.
31. Koval, C.A. and J.N. Howard, *Electron transfer at semiconductor electrode-liquid electrolyte interfaces.* Chem. Rev., 1992. **92**: p. 411-433.
32. Heller, A., *Hydrogen-evolving solar cells.* Science, 1984. **223**(4641): p. 1141-1148.
33. Lewis, N.S., *Mechanistic studies of light-induced charge separation at semiconductor/liquid interfaces.* Acc. Chem. Res., 1990. **23**: p. 176-183.
34. Harris, L.A. and R.H. Wilson, *Semiconductors for photoelectrolysis.* Ann. Rev. Mater. Sci., 1978. **8**: p. 99-134.
35. Wrighton, M.S., *Photoelectrochemical conversion of optical energy to electricity and fuels.* Acc. Chem. Res., 1979. **12**(9): p. 303-310.
36. Nozik, A.J., *p-n photoelectrolysis cell.* Appl. Phys. Lett., 1976. **29**: p. 150-153.
37. Gerischer, H., *On the stability of semiconductor electrodes against photodecomposition* J. Electroanal. Chem., 1977. **82**(1-2): p. 133-143
38. Gerischer, H., *The photoelectrochemical cell: principles, energetics and electrode stability* Electrochem. Soc., 1977. **77-3**(Semicond. Liq.-Junction Sol. Cells): p. 1-19.
39. Bard, A.J. and L.R. Faulkner, *Electrochemcial methods: Fundamental and applciations*. 1980, New York: John Wiley and Sons.
40. Parkinson, B., Acc. Chem. Res., 1984. **17**: p. 431.
41. Khan, S.U.M. and J. Akikusa, *Photoelectrochemical Splitting of Water at Nanocrystalline n-Fe2O3 Thin-Film Electrodes.* J. Phys. Chem. B, 1999. **103**: p. 7184-7189.
42. Khan, S.U.M., M. Al-Shahry, and W.B. Ingler, *Efficient photochemical water splitting by a chemically modified n-TiO2.* Science, 2002. **297**: p. 2243-2245.
43. Raja, K.S., V.K. Mahajan, and M. Misra, *Determination of photo conversion efficiency of nanotubular titanium oxide photo-electrochemical cell for solar hydrogen generation.* J. Power Sources, 2006. **159**: p. 1258-1265.
44. Butler, M.A. and D.S. Ginley, *Principles of photoelectrochemical, solar energy conversion.* J. Mater. Sci., 1980. **15**: p. 1-19.
45. Nozik, A.J., *Photoelectrolysis of water using semiconducting TiO2 crystals.* Nature, 1975. **257**: p. 383-386.
46. Wrighton, M.S., et al., *Photoassisted electrolysis of water by irradiation of a titanium dioxide electrode.* Proc. Nat. Acad. Sci., 1975. **72**: p. 1518-1522.
47. Dohrmann, J.K. and N.S. Schaaf, *Energy conversion by photoelectrolysis of water: determination of efficiency by in situ photocalorimetry.* J. Phys. Chem., 1992. **96**: p. 4558-4563.

48. Gerischer, H., ed. *Solar Photoelectrolysis with semiconductor electrodes*. Solar energy conversion: Solid-state physics aspects, ed. B.O. Seraphin. 1979, Springer-Verlag: New York. 115-172.
49. Akira, F. and H. Kenichi, *Electrochemical photolysis of water at a semiconductor electrode.* Nature, 1972. **238**(5358): p. 37-38.
50. Wrighton, M.S., et al., *Photoassisted electrolysis of water by ultraviolet irradiation of an antimony doped stannic oxide electrode.* J. Am. Chem. Soc., 1976. **98**: p. 44-48.
51. Yang, B. and V. Luca, *Enhanced long-wavelength transient photoresponsiveness of WO3 induced by tellurium doping.* Chem. Commun., 2008: p. 4454-4456.
52. Butler, M.A., R.D. Nasby, and Q. R.K., *Tungsten trioxide as an electrode for photoelectrolysis of water.* Solid State Commun. , 1976. **19**: p. 1011-1014.
53. Shaban, Y.A. and S.U.M. Khan, *Visible light active carbon modified (CM)-p-WO3 thin film electrodes for photosplitting of water.* ECS Trans., 2007. **6**(2): p. 93-100.
54. Gupta, M., et al., *Enhanced photoelectrochemical activity of 120 MeV Ag9+ irradiated nanostructured thin films of ZnO for solar-hydrogen generation via splitting of water.* Adv. Mater. Res., 2009. **67**(Nanomaterials and Devices): p. 95-102.
55. Gupta, M., et al., *Preparation and characterization of nanostructured ZnO thin films for photoelectrochemical splitting of water.* B. Mater. Sci., 2009. **32**(1): p. 23-30.
56. Yan, Y., et al., *Band gap reduction of ZnO for photoelectrochemical splitting of water.* Proc. of SPIE, 2007. **6650**(Solar Hydrogen and Nanotechnology II): p. 66500H/1-66500H/9.
57. Wolcott, A., et al., *Photoelectrochemical study of nanostructured ZnO thin films for hydrogen generation from water splitting.* Adv. Funct. Mater., 2009. **19**: p. 1849-1856.
58. Yang, X.Y., et al., *Nitrogen-doped ZnO nanowire arrays for photoelectrochemical water splitting.* Nano Lett., 2009. **9**(6): p. 2331-2336.
59. Ahn, K.S., et al., *Enhancement of photoelectrochemical response by aligned nanorods in ZnO thin films.* J. Power Sources, 2008. **176**: p. 387-392.
60. Ahn, K.S., et al., *Photoelectrochemical properties of N-incorporated ZnO films deposited by reactive RF magnetron sputtering.* J. Electrochem. Soc., 2007. **154**(9): p. B956-B959.
61. Barreca, D., et al., *The potential of supported Cu2O and CuO nanosystems in photocatalytic H2 production.* ChemSusChem, 2009. **2**(3): p. 230-233.
62. Kakuta, S. and T. Abe, *Structural characterization of Cu2O after the evolution of H2 under visible light irradiation.* Electrochem. Solid ST., 2009. **12**(3): p. 1-3.
63. Chauhan, D., et al., *Preparation and characterization of nanostructured CuO thin films for photoelectrochemical splitting of water.* Bull. Mat. Sci., 2006. **29**(7): p. 709-716.

64. Chaudhary, Y.S., et al., *Synthesis and characterization of nanostructured undoped/doped CuO films and their application in photoelectrochemical water splitting.* NSTI Nanotechnol., 2005. **2**: p. 601-603.
65. Ohnishi, T., Y. Nakato, and H. Tsubumura, *Quantum yield of photolysis of water on titanium oxide.* Ber Bunsenges Phys. Chem., 1975. **79**: p. 523-525.
66. Ghosh, A.K. and H.P. Muruska, *Photoelectrolysis of water in sunlight with sensitized semiconductor electrodes.* J. Electrochem. Soc., 1977. **128**: p. 1516-1522.
67. Giordano, N., et al., *Photoassisted decomposition of water over modified rutile electrodes* Int. J. Hydrogen Energy, 1982. **7**: p. 867-872.
68. Radecka, M., et al., *Photoresponse of undoped and W-doped TiO2.* Polish J. Chem., 2004. **78**: p. 1925-1934.
69. Wrighton, M.S., et al., *Strontium titanate photoelectrodes. Efficient photoassisted electrolysis of water at zero applied potential.* J. Am. Chem. Soc., 1976. **98**: p. 2774-2779.
70. Mavroides, J.G., J.A. Kafalas, and D.F. Kolesar, *Photoelectrolysis of water in cells with SrTiO3 anodes.* Appl. Phys. Lett., 1976. **28**: p. 241-243.
71. Xiao, Z.L., L.M. Lin, and Y.P. Weng, *Photoelectrocatalytic splitting of water into hydrogen by doping sandwich semiconductor photoelectrode* Hydrogen Syst., Pap. Int. Symp., 1986. **1**: p. 111-115.
72. Khan, S.U.M., R.C. Kainthla, and J.O.M. Bockris, *A model of a photon-induced self-driven electrochemical cell for water splitting to hydrogen* Adv. Hydrogen Energ., 1986. **5**(6): p. 560-567.
73. Yu, Z.G., et al., *Core-shell naorods for efficient photoelectrochemical hydrogen production.* J. Phys. Chem. B, 2005. **109**: p. 22913-22919.
74. Glasscock, J.A., et al., *Structural, optical and electrical properties of undoped polycrystalline hematite thin films produced using filtered arc deposition* Thin Solid Films, 2007. **516**: p. 1716-1724.
75. Sartoretti, C.J., et al., *Photoelectrochemical oxidation of water at transparent ferric oxide film electrodes.* Chem. Phys. Lett., 2003. **376**: p. 194-200.
76. Kay, A., I. Cesar, and M. Gratzel, *New benchmark for water photooxidation by nanostructured a-Fe2O3 films.* J. Am. Chem. Soc., 2006. **128**: p. 15714-15721.
77. Sanchez, C., K.D. Sieber, and G.A. Somorjai, *The photoelectrochemistry of niobium doped α-iron sesquioxide.* J. Electroanal. Chem., 1988. **252**(2): p. 269-290.
78. Komp, R.J., *Practical photovoltaics: electricity from solar cells*. 3rd ed. 1995, Ann Arbor, Michigan: Aatec Publications.
79. Hu, Y.S., et al., *Pt-doped a-Fe2O3 thin films active for photoelectrochemical water splitting.* Chem. Mater., 2008. **20**: p. 3803–3805.
80. Murphy, A.B., et al., *Efficiency of solar water splitting using semiconductor electrodes.* Int. J. Hydrogen Energy, 2006. **31**: p. 1999-2017.

81. Momirlan, M. and T.N. Veziroglu, *Current status of hydrogen energy.* Renew. Sust. Energ. Rev., 2002. **6**(1-2): p. 141-179.
82. Sivula, K., F.L. Formal, and M. Gratzel, *WO3-Fe2O3 photoanodes for water splitting: A host scaffold, guest absorber approach.* Chem. Mater., 2009. **21**: p. 2862-2867.
83. Dare-Edwards, M.P., et al., *Electrochemistry and photoelectrochemistry of p- and n-type oxides.* J. Chem. Soc., Farady Trans., 1983. **79**: p. 2027-2041.
84. Kennedy, J.H. and K.W. Frese, J. Electrochem. Soc., 1978. **125**: p. 709-714.
85. Sodergren, S., et al., J. Phys. Chem., 1994. **98**: p. 5552-5556.
86. Lindgren, T., et al., *Aqueous photoelectrochemistry of hematite nanorod array.* Sol. Energ. Mat. Sol. C., 2002. **71**: p. 231-243.
87. Gardner, R.F.G., F. Sweett, and D.W. Tanner, J. Phys. Chem. Solids, 1963. **24**: p. 1183.
88. Yazawa, K., H. Kamogawa, and H. Morisaki, *Semiconducting TiO2 films for photoelectrolysis of water.* Int. J. Hydrogen Energy, 1978. **4**: p. 205-209.
89. Dyer, C.K. and J.S.L. Leech, *Reversible optical changes within anodic oxide films on titanium and niobium.* J. Electrochem. Soc., 1978. **125**: p. 23-29.
90. Itoh, K. and J.O.M. Bockris, *Stacked thin-film photoelectrode using iron oxide.* J. Appl. Phys., 1984. **56**(3): p. 874-876.
91. Itoh, K. and J.O.M. Bockris, *Thin Film Photoelectrochemistry: Iron Oxide.* J. Electrochem. Soc.: Electrochemcial science and technology, 1984. **131**(6): p. 1266-1271.
92. Satsangi, V.R., *Metal oxide semiconductors in PEC splitting of water.* Proc. of SPIE, 2007. **6650**: p. 66500D-1-66500D-13.
93. Konenkamp, R., et al., *Thin film semiconductor deposition on free-standing ZnO columns.* Appl. Phys. Lett., 2000. **77**(16): p. 2575-2577.
94. Katoh, R., et al., *The kinetics and mechanism in electron injection and charge recombination in dye-sensitized nanocrystalline semiconductor.* Coord. Chem. Rev., 2004. **248**: p. 1195-1213.
95. Frank, A.J., N. Kopidakis, and J. Lagemaat, *Electron in nanostructured TiO2 solar cell: transport, recombination and photovoltaic properties.* Coord. Chem. Rev., 2004. **248**: p. 1195-1213.
96. Solbrand, A., et al., J. Phys. Chem. B., 1997. **101**: p. 2514.
97. Kamat, P.V., et al., J. Phys. Chem., 1996. **100**: p. 4900-.
98. Hodes, G. and I.D.J. Howell, J. Electrochem. Soc., 1992. **139**: p. 3136.
99. Duret, A. and M. Gratzel, *Visible light-induced water oxidation on mesoscopic Fe2O3 films made by ultrasonic spray pyrolysis.* J. Phys. Chem. B, 2005. **109**: p. 17184-17191.
100. Gondal, M.A., et al., Appl. Catal. A: Gen., 2004. **268**: p. 159.
101. Gondal, M.A., et al., Chem. Phys. Lett., 2004. **385**: p. 111.
102. Yu, J.G., et al., J. Phys. Chem. C, 2007. **111**: p. 10582.
103. Wei, Q., et al., *Enhanced photocatalytic activity of porous Fe2O3 films prepared by rapid thermal oxidation.* J. Phys.D: Appl. Phys., 2008. **41**: p. 1-4.

104. Jiao, F., et al., *Synthesis of ordered mesoporous Fe3O4 and r-Fe2O3 with crystalline walls using post-template reduction/oxidation.* J. Am. Chem. Soc., 2006. **128**: p. 12905-12909.
105. Poizot, P., et al., Nature, 2000. **407**: p. 496.
106. Rolison, D.R., Science, 2003. **299**: p. 1698.
107. Wang, L.Y., et al., Abstr. Pap. Am. Chem. Soc., 2004. **228**: p. U473-U473.
108. Srivastava, D.N., et al., J. Phys. Chem. B., 2002. **106**: p. 1878.
109. Malik, A.S., M.J. Duncan, and P.G. Bruce, J. Mater. Chem., 2003. **13**: p. 2123.
110. Long, J.W., et al., J. Am. Chem. Soc., 2004. **126**: p. 16879.
111. Jiao, F. and P.G. Bruce, Angew Chem. Int. Ed., 2004. **43**: p. 5958.
112. Lezau, A., et al., J. Phys. Chem. B, 2004. **108**: p. 5211.
113. Jiao, F., et al., *Ordered mesoporous Fe2O3 with crystalline walls.* J. Am. Chem. Soc., 2006. **128**: p. 5468-5474.
114. Bjorksten, U., J. Moser, and M. Gratzel, Chem. Mater., 1994. **6**(6): p. 858.
115. Frites, M. and S.U.M. Khan, *Photoelectrochemical splitting of water to H2 and O2 at n-Fe2O3 nanowire films and nanocrystalline carbon-modified (CM)-n-Fe2O3 thin films* ECS Trans., 2009. **19**(3): p. 137-145.
116. Mor, G.K., et al., *Enhanced photocleavage of water using titania nanotube arrays.* Nano. Lett., 2005. **5**: p. 191-195.
117. de Taconi, N.R., et al., *Nanoporous TiO2 and WO3 films by anodization of titanium and tungsten substrates: Influence of process variables on morphology and photoelectrochemical response.* J. Phys. Chem. B, 2006. **110**: p. 25347-25355.
118. Varghese, O.K., et al., *Water-photolysis properties of micron-length highly-ordered titania nanotube-arrays.* J. Nanosci. Nanotechnol, 2005. **5**: p. 1158-1165.
119. Chen, J., et al., *a-Fe2O3 nanotubes in gas sensor and lithium ion battery applications.* Adv. Mater., 2005. **17**: p. 582-586.
120. Sun, Z., et al., *A highly efficient chemical sensor material for H2S: a-Fe2O3 nanotubes fabricated using carbon nanotube templates.* Adv. Mater., 2005. **17**: p. 2993-2997.
121. Liu, L., et al., *Surfactant assisted synthesis of a-Fe2O3 nanotubes and nanorods with shape dependent magnetic properties.* J. Phys. Chem. B, 2006. **110**: p. 15218-15223.
122. Leygraf, C., M. Hendewerk, and G.A. Somorjai, *Photocatalytic production of hydrogen from water by a p- and n-type polycrystalline iron oxide assembly.* J. Am. Chem. Soc., 1982. **86**: p. 4484-4485.
123. Turner, J.E., et al., *The characterization of doped iron oxide electrodes for the photodissociation of water.* J. Electrochem. Soc.: Electrochemcial science and technology, 1984. **131**(8): p. 1777-1783.
124. Souza, F.L., et al., *Nanostructured hematite thin films produced by spin-coating deposition solution: Applicationinwatersplitting.* Sol. Energ. Mat. Sol. C., 2009. **93**: p. 362-368.

125. Saremi-Yarahmadi, S., et al., *Nanostructured a-Fe2O3 electrodes for solar driven water splitting: Effect of doping agents on preparation and performance.* J. Phys. Chem. C, 2009. **113**: p. 4768-4778.
126. Watanabe, A. and H. Kozuka, *Photoanodic properties of sol-gel-derived Fe2O3 thin films containing dispersed gold and silver particles.* J. Phys. Chem. B, 2003. **107**: p. 12713-12720.
127. Merchant, P., et al., *The electrical, optical and photoconducting properties of iron chromium oxide (Fe2-xCrxO3) (0 ≤ x ≤ 0.47).* J. Solid State Chem., 1979. **27**(3): p. 307-315.
128. Leygraf, C., M. Hendewerk, and G.A. Somorjai, *Photodissociation of water by p- and n-type polycrystalline iron oxides by using visible light (<=2.7 eV) in the absence of external potential* Proc. Natl. Acad. Sci. USA, 1982. **79**: p. 5739-5741.
129. Ingler, W.B. and S.U.M. Khan, *A self-driven p/n-Fe2O3 tandem photoelectrochemical cell for water splitting.* Electrochemical. Solid St. , 2006. **9**(4): p. G144-G146.
130. Kumari, S., et al., *Characterization of Zn-doped hematite thin films for photoelectrochemcial splitting water.* Curr. Sci. India, 2006. **91**(8): p. 1062-1064.
131. Ingler, W.B., J.P. Baltrus, and S.U.M. Khan, *Photoresponse of p-type zinc-doped iron(III) oxide thin films.* J. Am. Chem. Soc., 2004. **126**: p. 10238-10239.
132. Aroutiounian, V.M., et al., *Photoelectrochemistry of semiconductor electrodes made of solid solutions in the system Fe2O3-Nb2O5.* Sol. Energy, 2006. **80**: p. 1098-1111.
133. Gurunathan, K. and P. Maruthamuthu, *Photogeneration of hydrogen using visible light with undoped/doped a-FesO3 in the presence of methyl viologen.* Int. J. Hydrogen Energy, 1995. **20**(4): p. 287-295.
134. Sanchez, H.L., H. Steinfink, and H.S. White, *Solid solubility of germanium, silicon, and magnesium in iron oxide (Fe2O3) and photoelectric behavior* J. Solid State Chem., 1982. **41**(1): p. 90-96.
135. Glasscock, J.A., et al., *Enhancement of photoelectrochemical hydrogen production from hematite thin films by the introduction of Ti and Si.* J. Phys. Chem. C, 2007. **111**: p. 16477-16488.
136. Ingler, W.B. and S.U.M. Khan, *Photoresponse of spray pyrolysis synthesized copper-doped p-Fe2O3 thin film electrodes in water splitting.* Int. J. Hydrogen Energy, 2005. **30**: p. 821-827.
137. Liang, Y., C.S. Enache, and R. van de Krol, *Photoelecrochemical characterisation of sprayed a-Fe2O3 thin films: Influence of Si doping and SnO2 interfacial layer.* International Journal Photoenergy, 2008. **2008**: p. 1-7.

138. Sartoretti, C.J., et al., *Photoelectrochemical oxidation of water at transparent ferric oxide film electrodes.* J. Phys. Chem. B, 2005. **109**: p. 13685-13692.
139. Luo, W., et al., *Enhanced photocurrent–voltage characteristics of WO3/Fe2O3 nano-electrodes.* J. Phys. D: Appl. Phys., 2007. **40**: p. 1091–1096.
140. Kumari, S., et al., *Ehanced photoelectrochemical response of zn-dotted hematite.* International Journal of Photoenergy, 2007. **2007**: p. 1-6.
141. Hu, Y.S., et al., *Improved photoelectrochemical performance of Ti-doped a-Fe2O3 thin films by surface modification with fluoride.* Chem. Commun., 2009: p. 2652–2654.
142. Hu, Y.S., et al., *Improved photoelectrochemical performance of Ti-doped a-Fe2O3 thin films by surface modification with fluoridew.* Chem. Commun., 2009. **2009**: p. 2652–2654.
143. Stein, A., F. Li, and N.R. Denny, *Morphological control in colloidal crystal templating of inverse opals, hierarchical structures, and shaped particles.* Chem. Mater., 2008. **20**: p. 649-666.
144. Ren, M., R. Ravikrishna, and K.T. Valsaraj, *Photocatalytic degradation of gaseous organic species on photonic band-gap titania.* Environ. Sci. Technol., 2006. **40**: p. 7029-7033.
145. Velev, O.D. and A.M. Lenhoff, Curr. Opin Colloid Interface Sci., 2000. **5**: p. 56.
146. Asua, J.M., Prog. Polym. Sci., 2002. **27**: p. 1283-1346.
147. Bjorksten, U., J. Moser, and M. Gratzel, *Photoelectrochemical studies on nanocrystalline hematite films* Chem. Mater., 1994. **6**: p. 858-863.
148. Petkewich, R., *Adhesive Tape.* Chem. Eng. News 2007. **85**(42): p. 39.
149. Cullity, B.D. and S.R. Stock, *Elements of X-ray diffraction*. Third ed. 2001, Upper Saddle River: Prentice Hall. 664.
150. Kettle, S.F.A., *Physical inorganic chemistry : a coordination chemistry approach* 1996, Sausalito: University Science Books. 490.
151. Kawashima, T., et al., *FTO/ITO double-layered transparent conductive oxide for dye-sensitized solar cells.* 2004. **164**: p. 199-202.
152. Uekawa, N., M. Watanabe, and K. Kaneko, *Mixed-valence formation in highly oriented Ti-doped iron oxide film.* J. Chem, Soc. Faraday Trans., 1995. **91**(14): p. 2161-2166.
153. Hida, Y. and H. Kozuka, *Photoanodic properties of sol - gel-derived iron oxide thin films with embedded gold nanoparticles: effects of polyvinylpyrrolidone in coating solutions.* Thin Solid Films, 2005. **476**: p. 264-271.